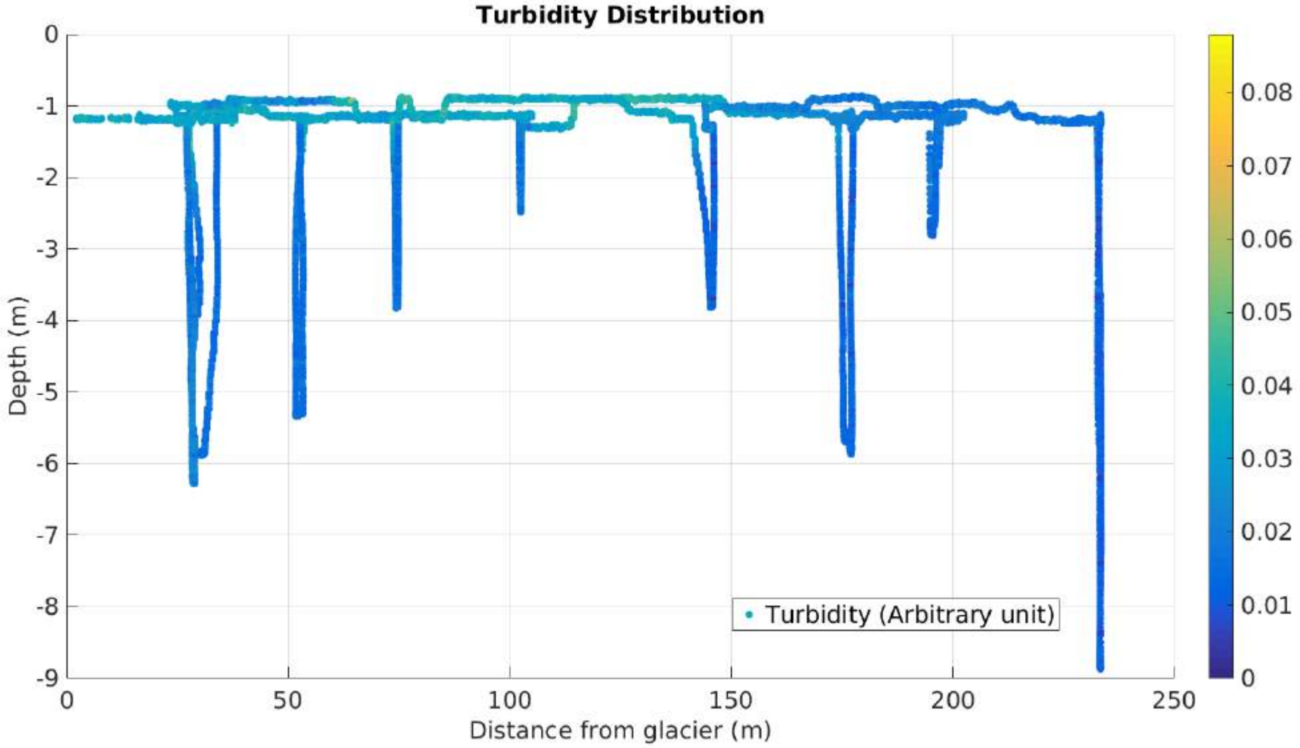

Figure 4.39 - Variation in Turbidity (arbitrary unit; yellow = high turbidity; blue = low turbidity) as a function of depth (m, y-axis) and distance from the front of the glacier (m, x-axis). The values of the turbidity are expressed in arbitrary units since they are raw data, read directly from the serial port of the sensors, not yet converted to values with a SI measurement unit.

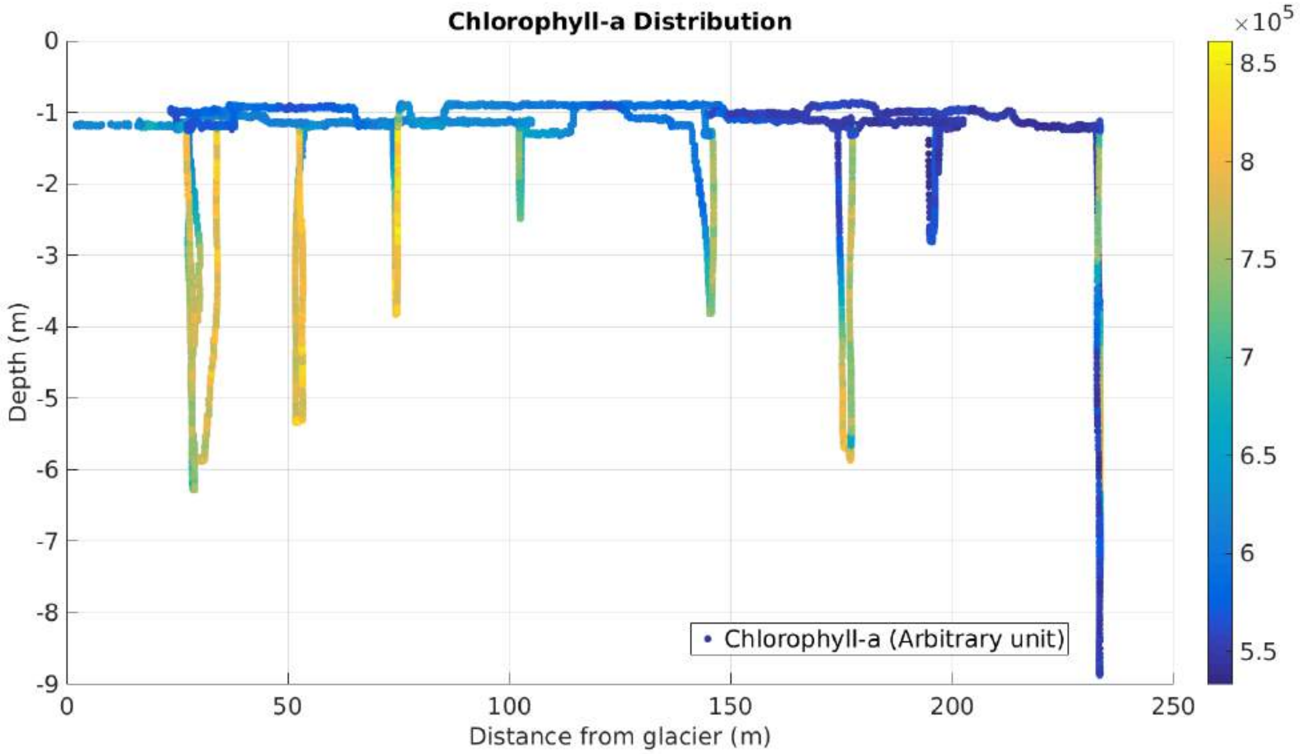

Figure 4.40 - Variation in Chlorophyll-a (arbitrary unit; yellow = high Chl-a; blue = low Chl-a) as a function of depth (m, y-axis) and distance from the front of the glacier (m, x-axis). The values of the Chl-a are expressed in arbitrary units since they are raw data, read directly from the serial port of the sensors, not yet converted to values with a SI measurement unit.

Also chlorophyll-a concentration is considerably higher in areas near glacier front where the increased subglacial melt enhances the supply of suspended matter and nutrients into the marine environment and intensifies stratification of water masses, stabilizing the phytoplankton near the surface. The presence and the complexity in the distribution of the chlorophyll-a parameter near the glacier front is particularly evident in Figure 4.41 which represents the trend (x-axis) as a function of the depth (m, y-axis), indicating with red color the data corresponding to the surface water masses and with the color scale (blue = near; yellow = far) the distance from the front of the glacier.

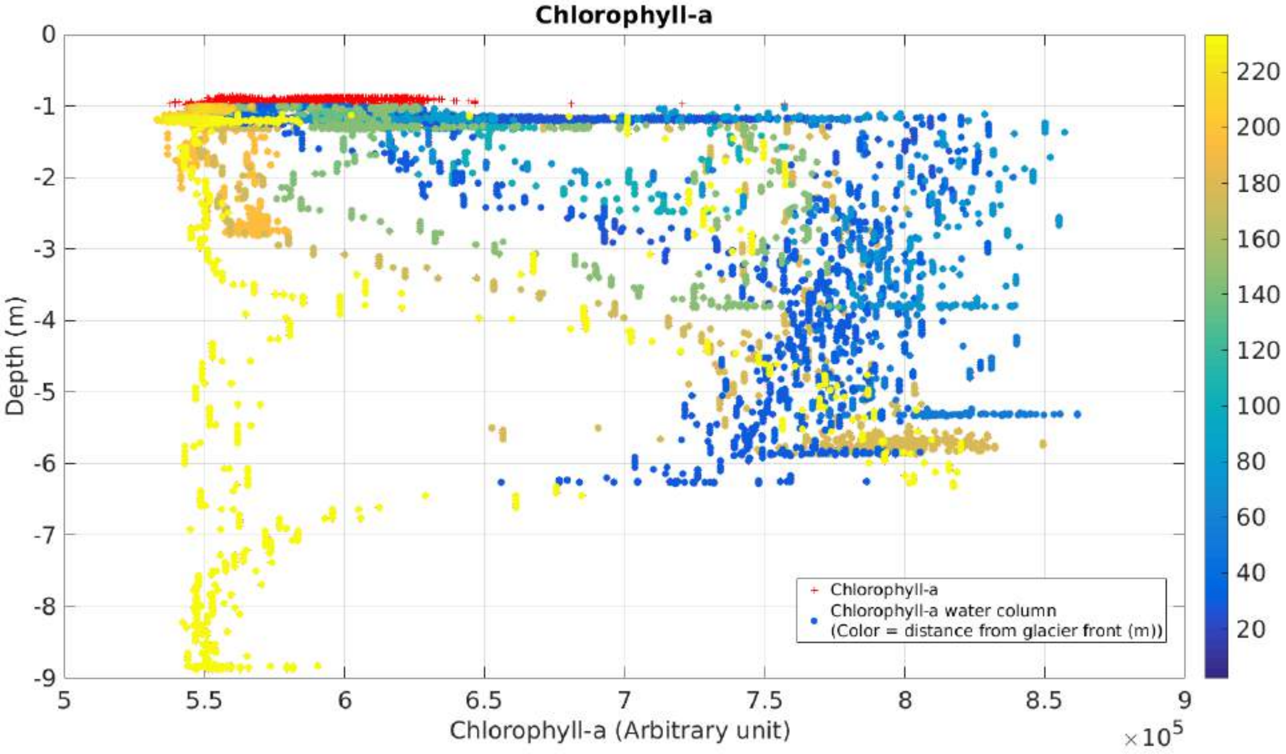

Figure 4.41 - Chlorophyll-a trend (arbitrary unit, x-axis) as a function of the depth (m, y-axis); red cross represent data corresponding to the surface water masses; the scale of the colors (blue = near; yellow = far) indicates the distance from the front of the glacier. The values of the Chl-a are expressed in arbitrary units since they are raw data, read directly from the serial port of the sensors, not yet converted to values with a SI measurement unit.

This figure confirms that near the front of the glacier there are higher chlorophyll-a values, probably due to ice melting phenomenon.

In general, from the analysis of these data it can be seen that the coastal glaciers of the Kongsfjorden are a very important feeding area for many organisms. Thanks to phytoplankton blooms, which are due to continental intake of nutrients, this area attracts fish and top predators such as seals, seabirds and polar bears, resulting fundamental for the entire ecosystem of the Arctic area. The study of the dynamics of ice and water masses by means of autonomous robotic platforms, which allow the collection of data not otherwise obtainable, is therefore fundamental in a perspective of continuous monitoring of the area and of the possible hazards present, which can disturb the fragile balance within the fjord.

4.4 Air data analysis

The goal of the campaigns was to carry out an integrated characterisation of the water column – water surface – air column. In order to reach this ambitious scope, two release systems based on automatic winches were installed on the robotic platform PROTEUS. The astern winch was used for releasing and recovering a set of instruments for the bio-chemical-physical characterization of the water column, as described in the first part of this chapter.

The fore winch was used for launching and recovering a helium-filled aerostat carrying the AirQino system, in order to record the variation of meteorological parameters (temperature and relative humidity) and various atmospheric components such as CO_2, O_3, CO, NO_2 and particulate matter (PM2.5, PM10).

Data from the air column were acquired near the front of Kongsbreen and Blomstrandbreen glacier: different vertical profiles were performed using the helium filled balloon attached to the winch, at increasing distance from the glacier front. The purpose of these test was to study the variation of the air parameters near the front of the tidewater glaciers and to possible highlight some particular trend with respect to the distance of the glacier.

Furthermore, these data allow to characterize the instantaneous meteorological situation close to the glacier front, which has a direct influence on the creation of transient phenomena (the main subject of this thesis) in the water, generated by the melting of the ice.

In the following graphs the different parameters are shown, both for Kongsbreen and Blomstrandbreen.

4.4.1 Kongsbreen

The AirQino system, in addition to the sensors for air quality, is also equipped with a GPS in order to geolocalize the parameters acquired. In the following graph the path followed by the AirQino system is shown. The front of the glacier is located in the bottom right part of the graph.

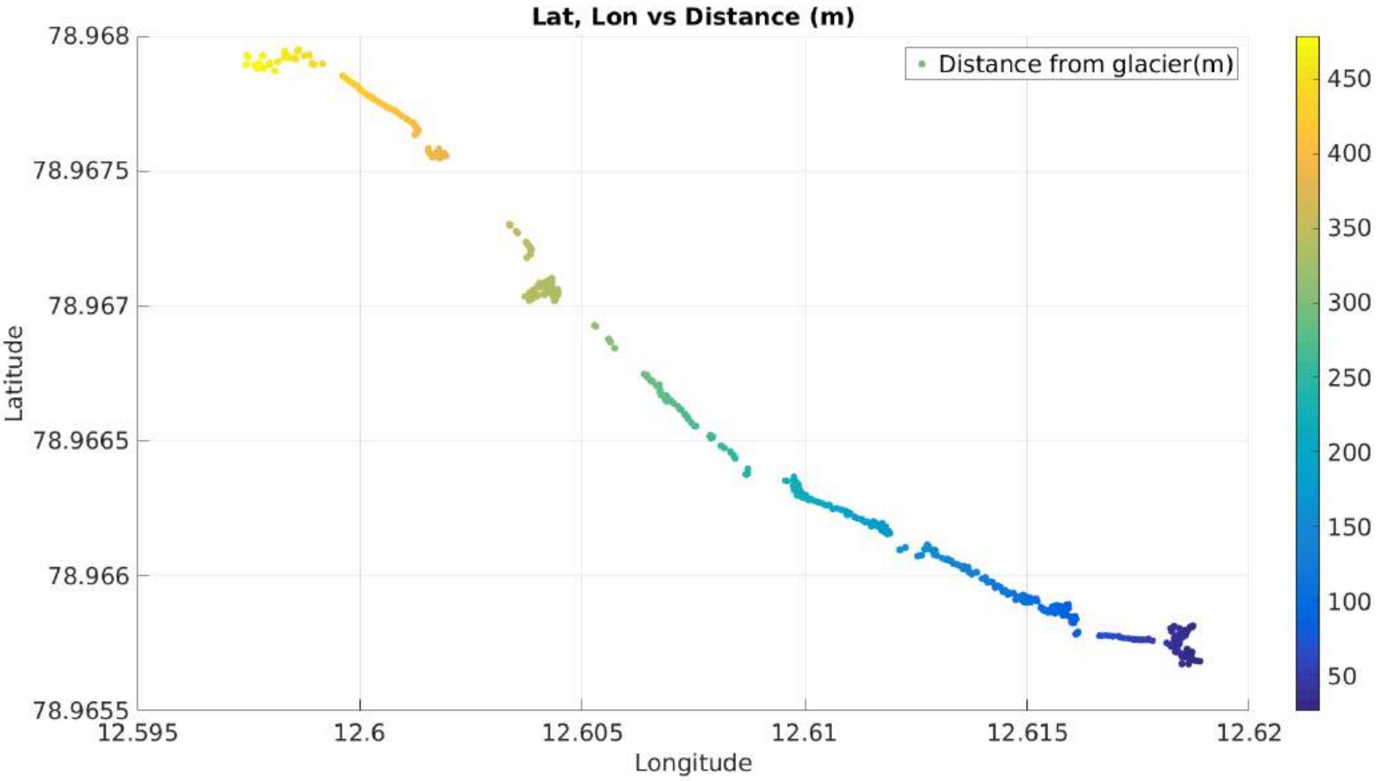

Figure 4.42 - Latitude and longitude (WGS84, EPSG 4326 reference system) positions of AirQino. The color is proportional to the distance from the glacier front (m): blue = near; yellow = far. The front of Kongsbreen glacier is in the bottom-right part of the graph.

During the sampling the system performed vertical profiles along the air column. This is visible in the following graph, showing the pressure (hPa) values with different colors: lower pressure values (blue dots) indicate higher height of the sampling system with respect to the water surface; on the contrary, higher pressure values (yellow dots) indicate lower height of the system with respect to water surface.

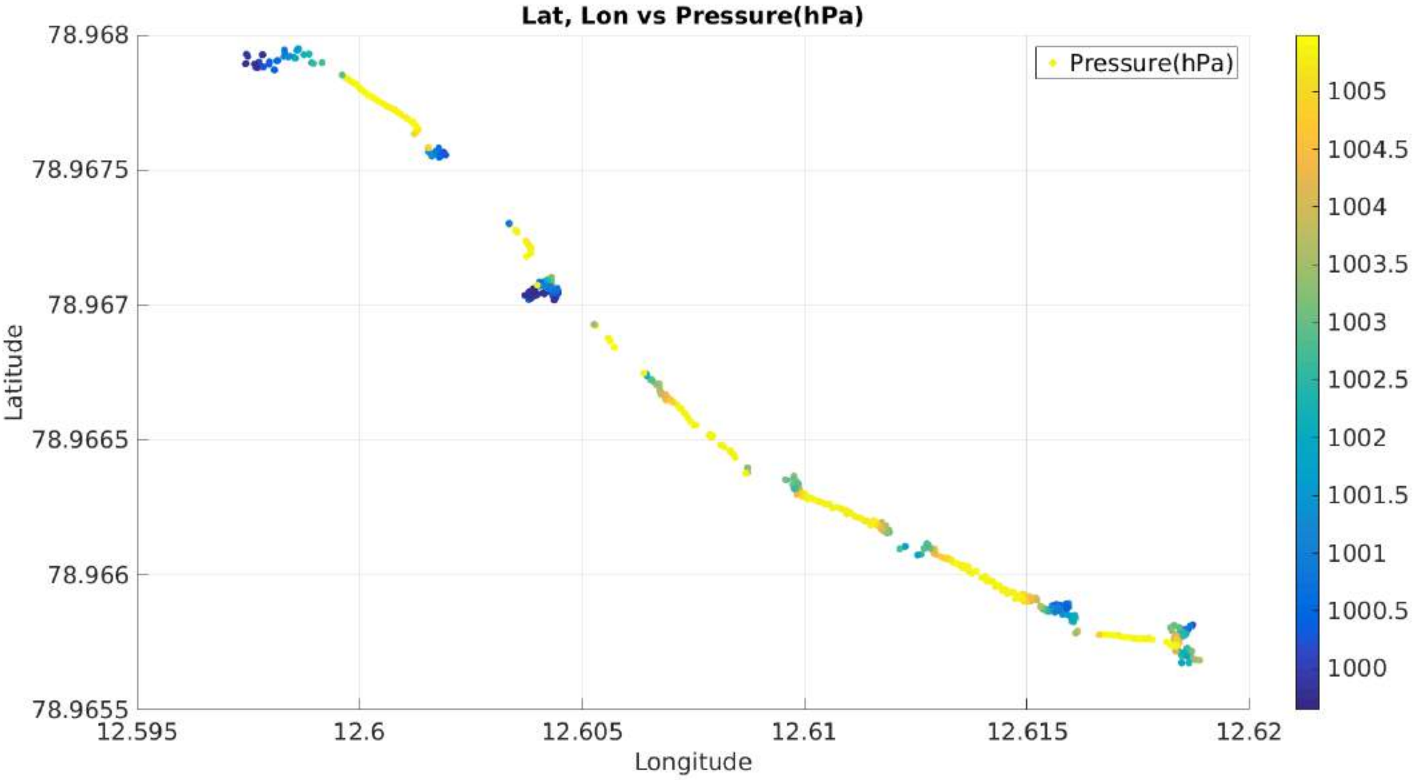

Figure 4.43 - Latitude and longitude (WGS84, EPSG 4326 reference system) positions of AirQino. The color is proportional to the pressure (hPa): lower pressure values (blue dots) indicate higher height of the sampling system with respect to the water surface; higher pressure values (yellow dots) indicate lower height of the system with respect to water surface. The front of Kongsbreen glacier is in the bottom-right part of the graph.

The following graph shows the trends of CO_2 (ppm, left y-axis) and Temperature (°C, right y-axis) as a function of the distance from the front of the glacier (m, x-axis).

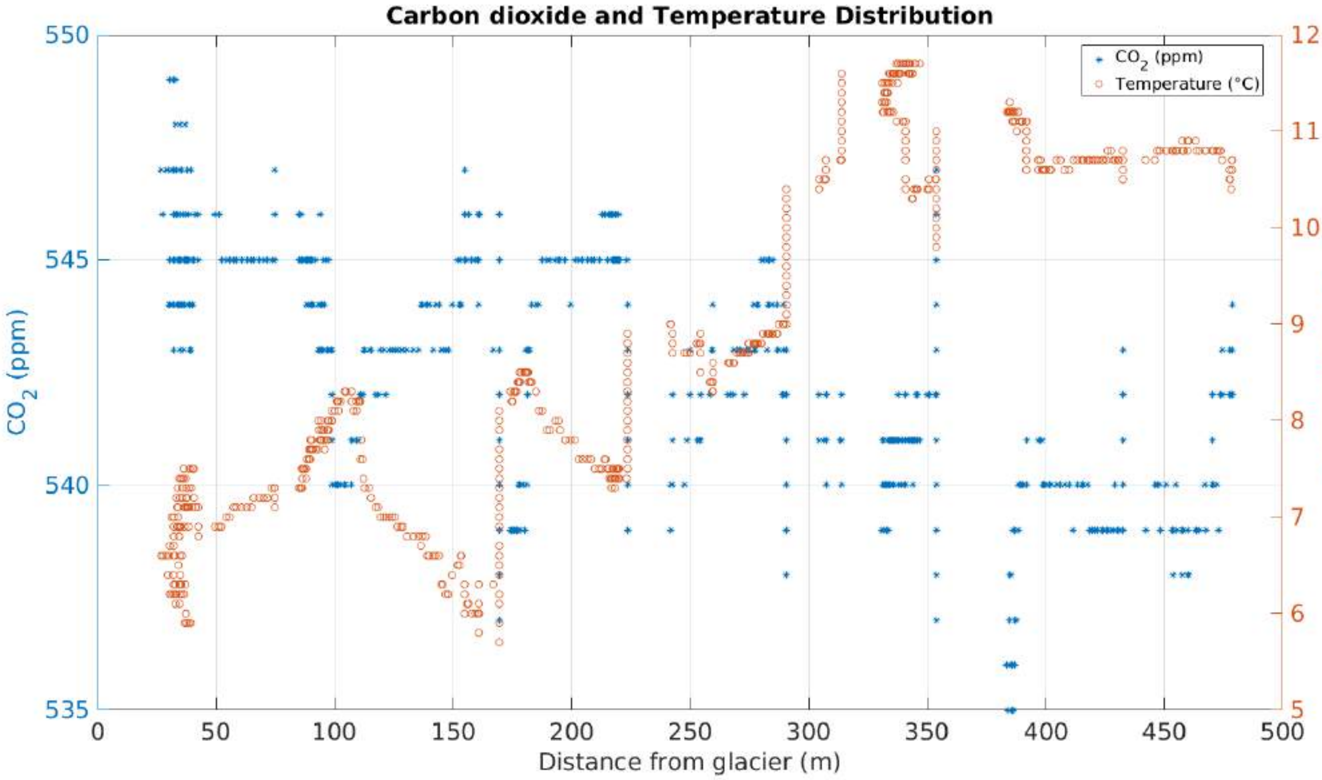

Figure 4.44 - Trends of CO_2 (ppm, left y-axis, blue dots) and Temperature (°C, right y-axis, orange dots) as a function of the distance from the front of the Kongsbreen glacier (m, x-axis).

Carbon dioxide (CO_2) is the most important greenhouse gas. CO_2 is the end product in the atmosphere of the oxidation of all main organic compounds, and it has shown an increase of as much as 40 % since the pre-industrial time, mainly due to emissions from combustion of fossil fuels and land use change (Myhre et al., 2013). In Svalbard there are different observatories for the long term monitoring of CO_2 and other greenhouse gases like, for example, the Climate Change Tower in Ny Alesund.

With the AirQino system it is possible to acquire a snapshot of the atmospheric situation in a precise and very short time interval. What can be seen is a trend of increasing temperature and decreasing CO_2 with respect to the distance from the glacier. These trends are also visible in the following two graphs that show the values of the two variables, also as a function of pressure (and therefore of height compared to sea level).

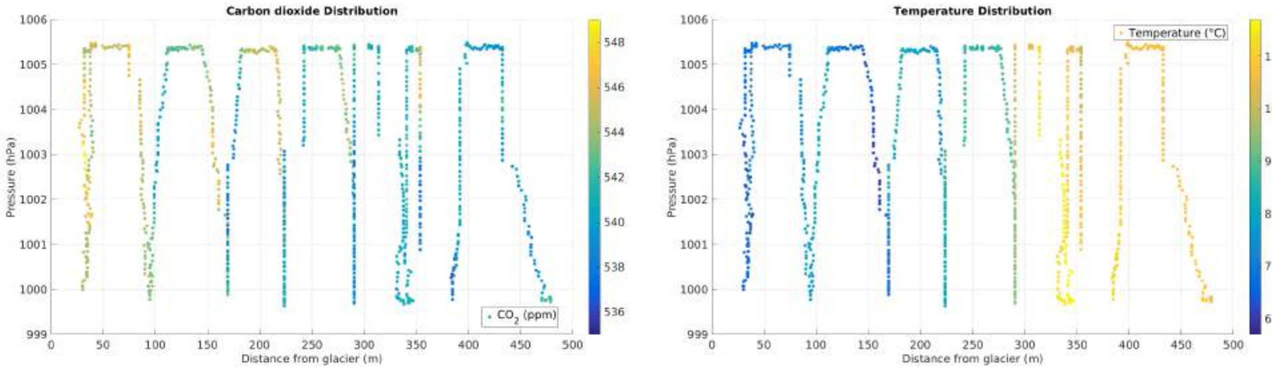

Figure 4.45 – Left: variation in CO_2 (ppm; yellow = high CO_2; blue = low CO_2) as a function of pressure (hPa, y-axis) and distance from the front of the glacier (m, x-axis). Right: variation in Temperature (°C; yellow = high Temperature; blue = low Temperature) as a function of pressure (hPa, y-axis) and distance from the front of the Kongsbreen glacier (m, x-axis).

As regards CO_2, there is also a slight dependence on the sampling height, in particular there is a small decrease in CO_2 increasing the height (and therefore at low pressure values). The temperature instead does not show this type of dependence by these small height variations. An increase in temperature also corresponds to a decrease in Relative Humidity (RH) as shown in the following graphs. Furthermore, relative humidity shows a slight decreasing trend with height respect to sea level (and therefore a decrease in pressure, figure 4.46 right) especially in an area between 320-350 m from the front of the glacier.

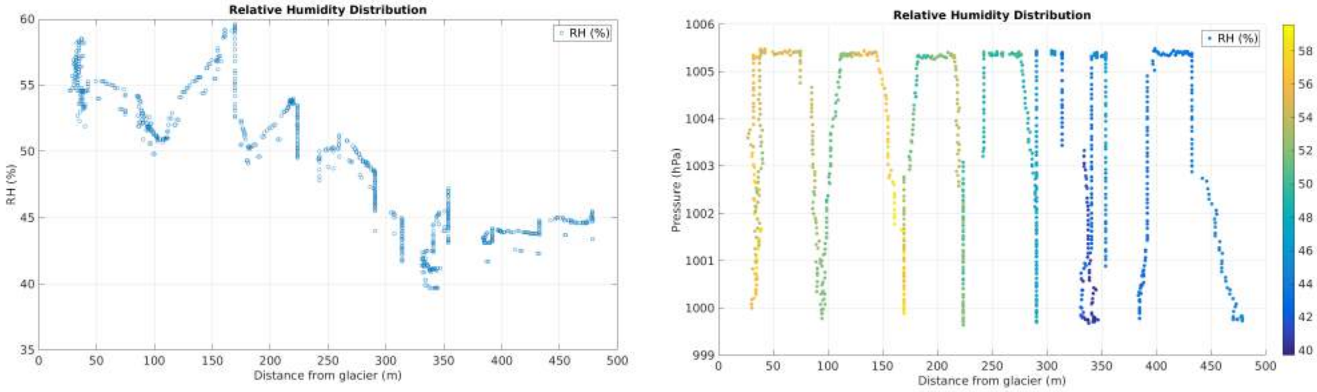

Figure 4.46 – Left: Trend of Relative Humidity (%) as a function of the distance from the glacier front (m). Right: variation in Relative Humidity (%; yellow = high RH; blue = low RH) as a function of pressure (hPa, y-axis) and distance from the front of the Kongsbreen glacier (m, x-axis).

Regarding the variables Nitrogen Dioxide and Ozone (NO_2 e O_3), from the following graphs it can be seen that NO_2 does not show a particular trend, with values that oscillate fairly homogeneously even with increasing distance from the glacier. A small peak of NO_2 values can be observed at distances between 320-350 m from the glacier, which had already been highlighted in the previous temperature and relative humidity graphs. This fact is clearly visible in the Figure 4.48 left, with yellow dots at about 350 m.

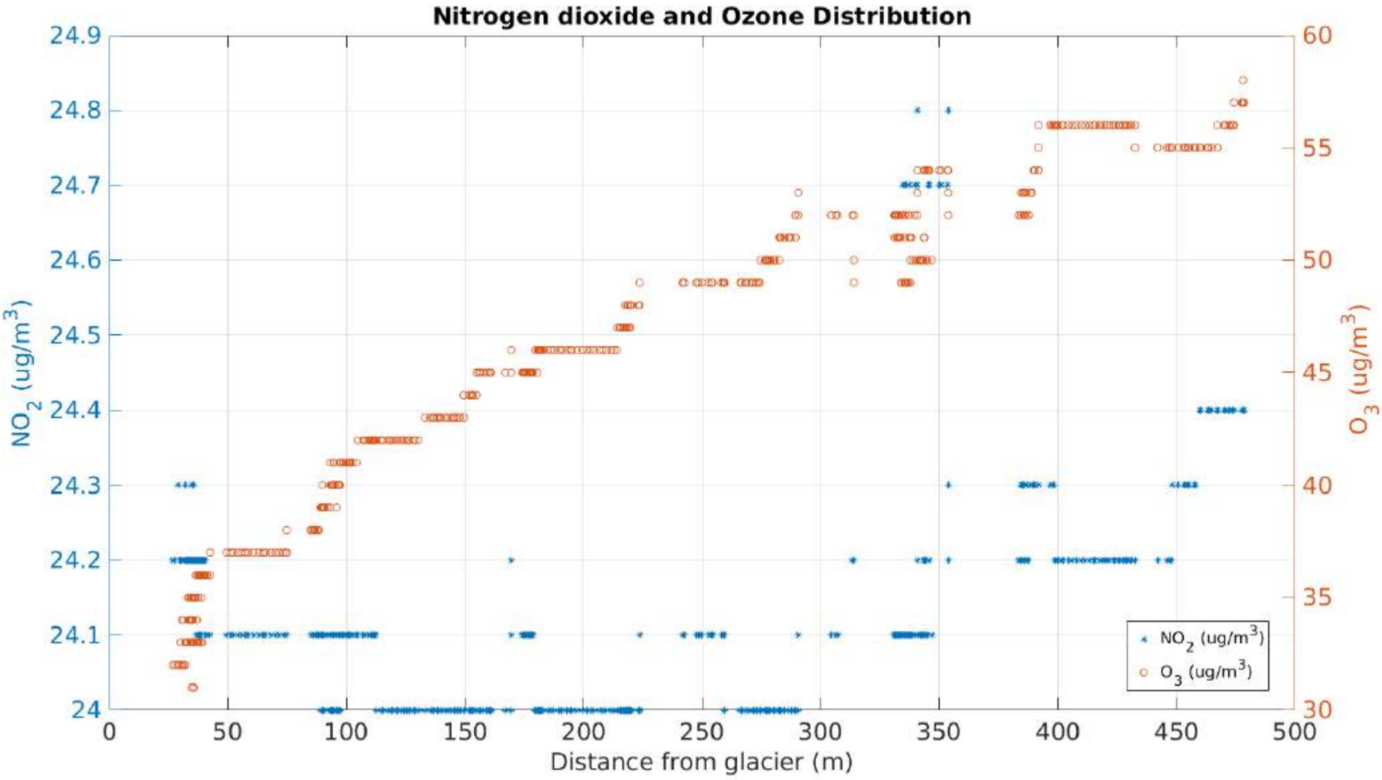

Figure 4.47 - Trends of NO_2 (ug/m^3, left y-axis, blue dots) and O_3 (ug/m^3, right y-axis, orange dots) as a function of the distance from the front of the Kongsbreen glacier (m, x-axis).

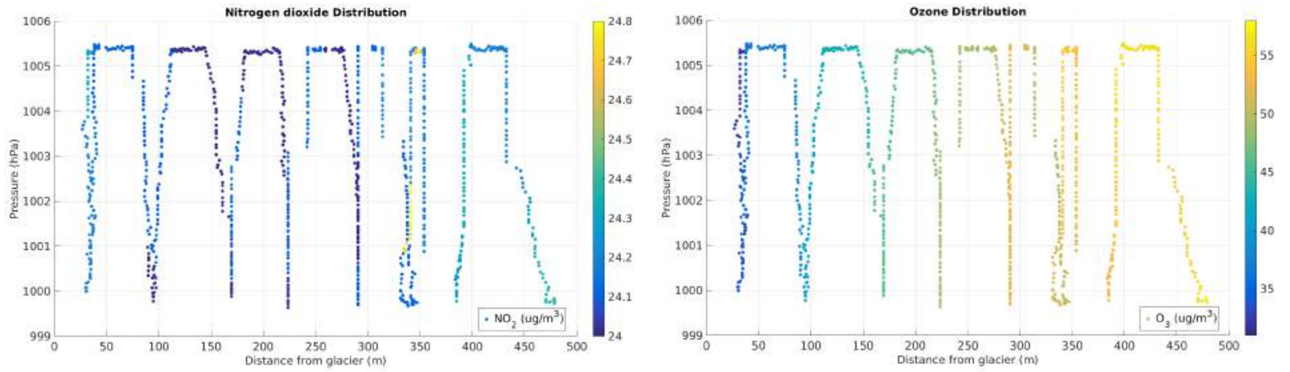

Figure 4.48 - Left: variation in NO_2 (ug/m^3; yellow = high NO_2; blue = low NO_2) as a function of pressure (hPa, y-axis) and distance from the front of the glacier (m, x-axis). Right: variation in O_3 (ug/m^3; yellow = high O_3; blue = low O_3) as a function of pressure (hPa, y-axis) and distance from the front of the Kongsbreen glacier (m, x-axis).

As for Ozone, it shows an increasing trend as a function of the distance from the front of the glacier while there are no effects related to the height of the sampling.

Generally speaking, Ozone (O_3) and Nitrogen dioxide (NO_2) are included among the air pollutants by virtue of their adverse impact on human health and the natural environment. In the troposphere, near the Earth's surface, Ozone is formed through a complex series of reactions involving the action of sunlight on nitrogen dioxide (NO_2) and hydrocarbons. As the formation of ground level ozone depends on the intensity of solar radiation, many observations have shown that on clear days the concentration of ozone rises with increasing intensity of solar radiation and temperature. The tropospheric background is derived from both natural and man-made sources; a range of annual average values of 40–70 µg/m^3 is a reasonable estimate of the level.

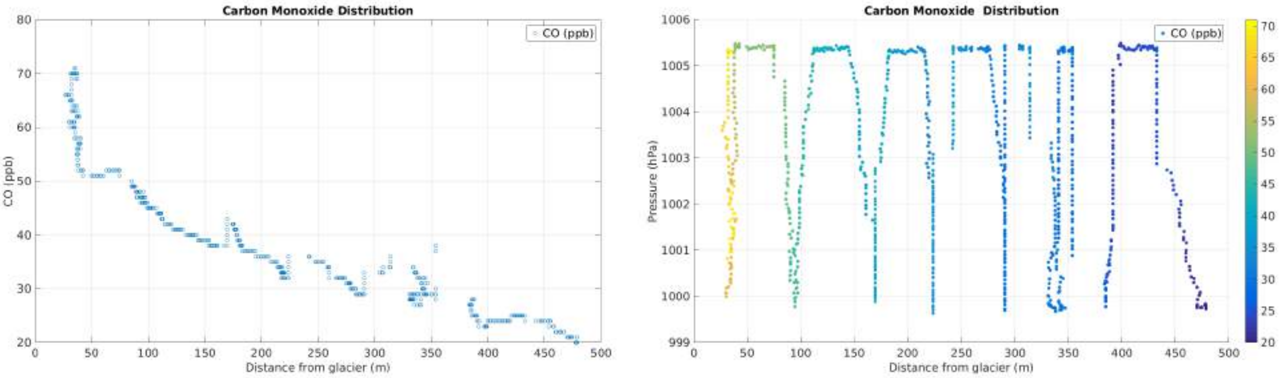

Figure 4.49 - Left: Trend of CO (ppb) as a function of the distance from the glacier front (m). Right: variation in CO (ppb; yellow = high CO; blue = low CO) as a function of pressure (hPa, y-axis) and distance from the front of the Kongsbreen glacier (m, x-axis).

Concerning Carbon monoxide (CO) is not considered as a direct greenhouse gas, mostly because it does not absorb terrestrial thermal IR energy strongly enough. However, CO is able to modulate the level of methane and production of tropospheric Ozone, which are both very important climate components (Myhre et al., 2013).

The natural concentration of carbon monoxide in air for the Svalbard region is around 115 parts per billion (ppb), and that amount is not harmful to humans. Natural sources of carbon monoxide include volcanoes and bush-fires.

The graphs in Figure 4.49 show a decreasing value of CO with increasing distance from the glacier and no dependence from the vertical movement of the system. In this case, the values are well below the mean values registered for the Svalbard area.

In this case graphs of the variables PM2.5 and PM10 are not shown because the values are so low that they are illegible from the sensors used. This fact means that no particulate matter worthy of relevance is present near the Kongsbreen glacier.

4.4.2 Blomstrandbreen

In the following graph the path followed by the AirQino system to sample the air column in the area facing the Blomstrandbreen glacier is shown. The front of the glacier is located in the up right part of the graph.

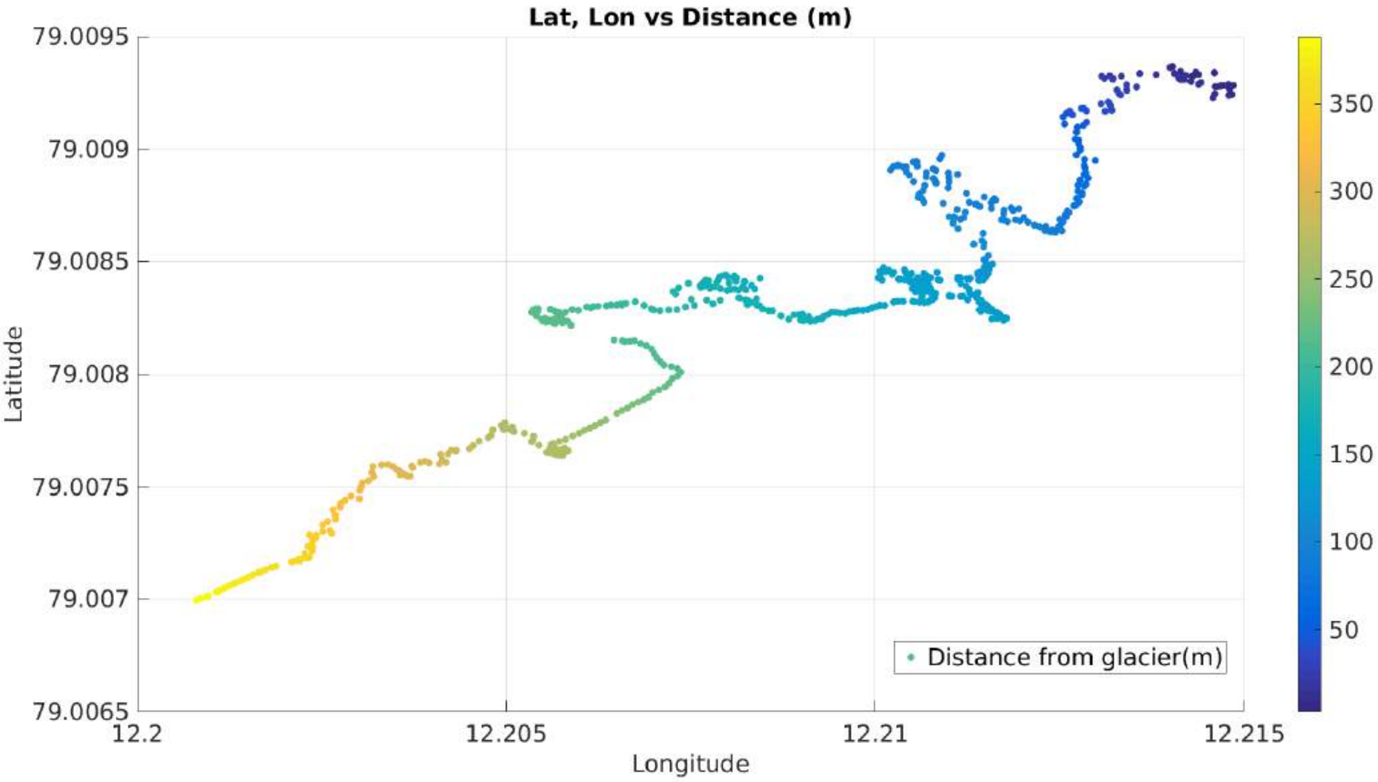

Figure 4.50 - Latitude and longitude (WGS84, EPSG 4326 reference system) positions of AirQino. The color is proportional to the distance from the glacier front (m): blue = near; yellow = far. The front of Blomstrandbreen glacier is in the up-right part of the graph.

Also in this case, during the sampling the system performed vertical profiles along the air column. This is visible in the following graph, showing the pressure (hPa) values with different colors: lower pressure values (blue dots) indicate higher height of the sampling system with respect to the water surface; on the contrary, higher pressure values (yellow dots) indicate lower height of the system with respect to water surface.

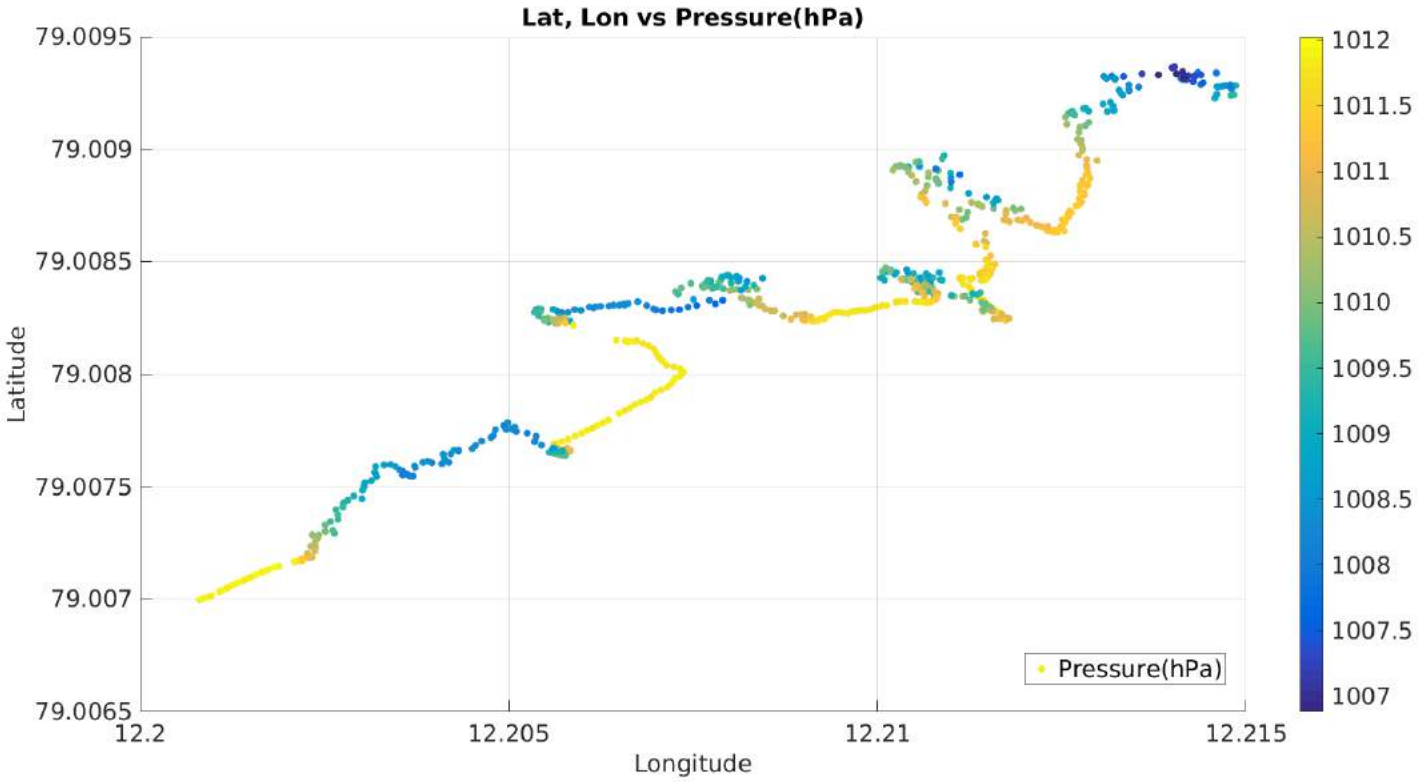

Figure 4.51 - Latitude and longitude (WGS84, EPSG 4326 reference system) positions of AirQino. The color is proportional to the pressure (hPa): lower pressure values (blue dots) indicate higher height of the sampling system with respect to the water surface; higher pressure values (yellow dots) indicate lower height of the system with respect to water surface. The front of Blomstrandbreen glacier is in the up-right part of the graph.

The following graph shows the trends of CO_2 (ppm, left y-axis) and Temperature (°C, right y-axis) as a function of the distance from the front of the glacier (m, x-axis).

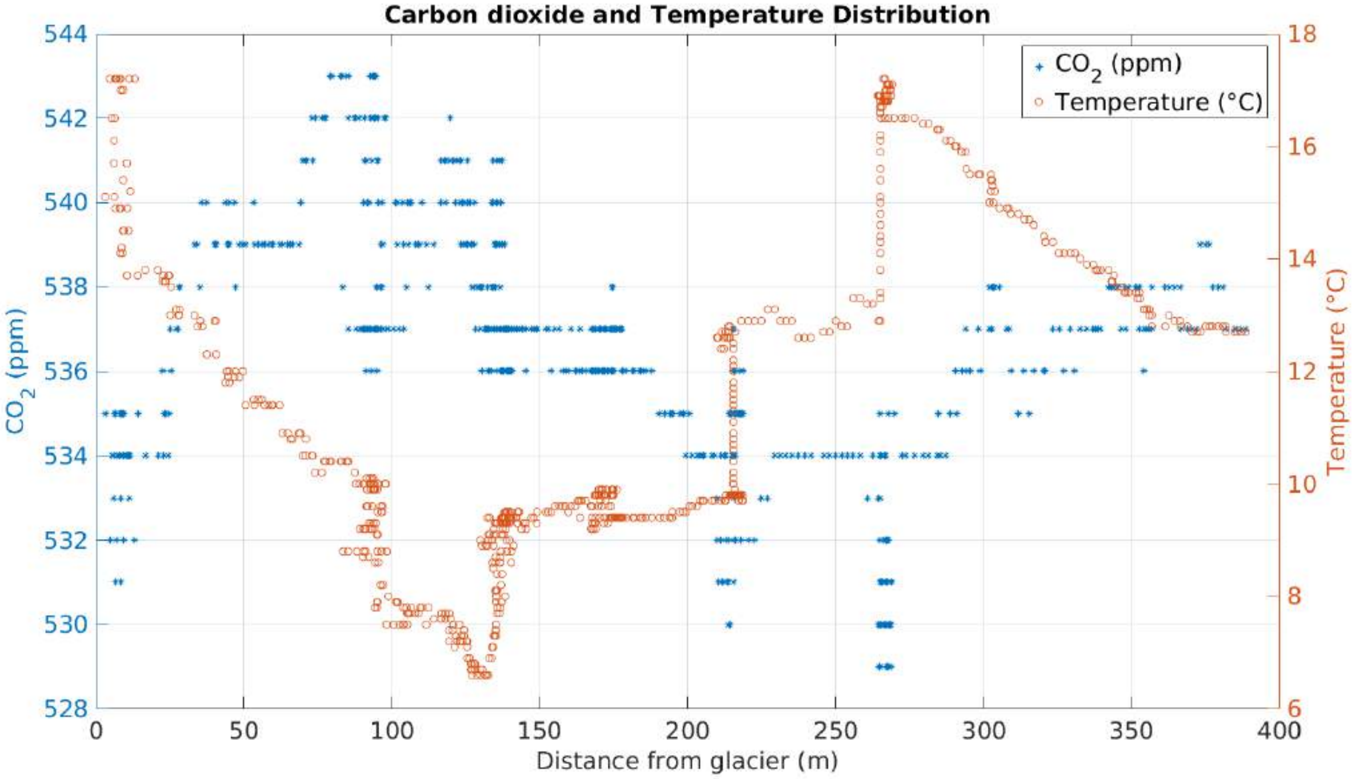

Figure 4.52 - Trends of CO_2 (ppm, left y-axis, blue dots) and Temperature (°C, right y-axis, orange dots) as a function of the distance from the front of the Blomstrandbreen glacier (m, x-axis).

In this graph it is observed that, moving away from the front of the glacier, a decrease in temperature corresponds to an increase in CO_2 and vice versa. This opposite behavior between the two variables (CO_2 increase/Temperature decrease and vice versa) is also observed and confirmed in general by the annual time series data, as reported in (Carotenuto et al., 2020).

The following graphs, on the other hand, show the trends of the CO_2 and temperature variables (color scale) as a function of the distance from the front of the glacier (m, x-axis) and pressure (hPa, y-axis). There is a small decrease in CO_2 values and a small increase in temperature when the pressure decreases (and therefore height increases).

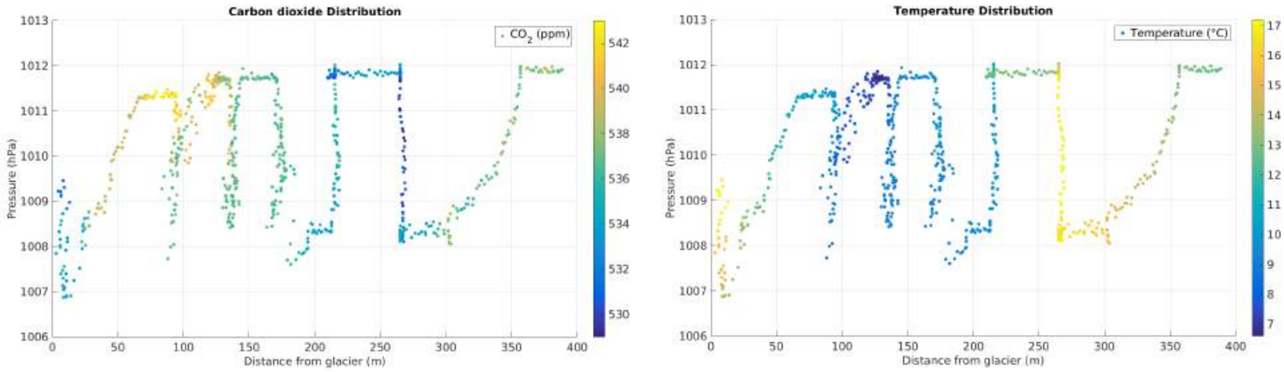

Figure 4.53 - Left: variation in CO_2 (ppm; yellow = high CO_2; blue = low CO_2) as a function of pressure (hPa, y-axis) and distance from the front of the glacier (m, x-axis). Right: variation in Temperature (°C; yellow = high Temperature; blue = low Temperature) as a function of pressure (hPa, y-axis) and distance from the front of the Blomstrandbreen glacier (m, x-axis).

By comparing the graphs of temperature and those of relative humidity (RH), a specular trend of the two variables is observed also in this case: an increase in temperature corresponds to a decrease in Relative Humidity (RH) and vice versa. Furthermore, relative humidity shows a slight decrease trend with increasing height with respect to sea level (lower pressure).

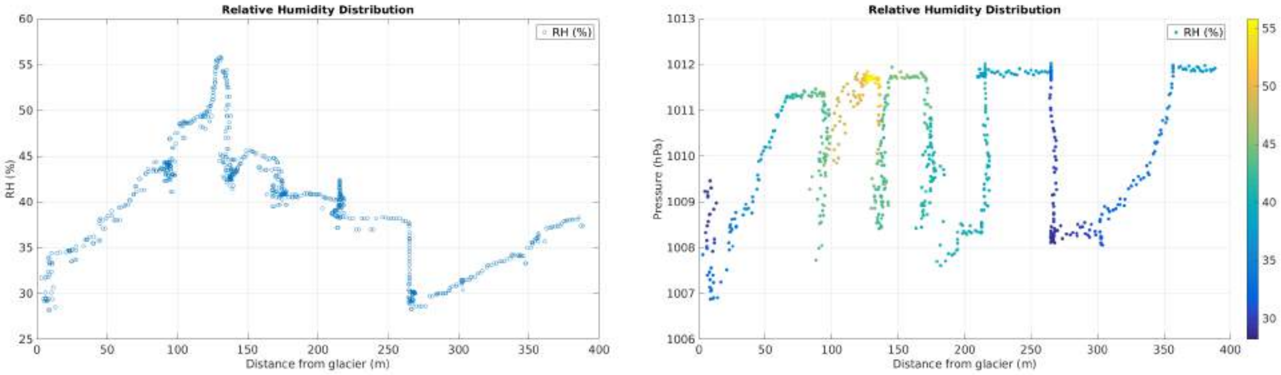

Figure 4.54 - Left: Trend of Relative Humidity (%) as a function of the distance from the glacier front (m). Right: variation in Relative Humidity (%; yellow = high RH; blue = low RH) as a function of pressure (hPa, y-axis) and distance from the front of the Blomstrandbreen glacier (m, x-axis).

About the variables Nitrogen Dioxide and Ozone (NO_2 e O_3), from the following graphs it can be seen that NO_2 does not show a particular trend, with values that oscillate fairly homogeneously even with increasing distance from the glacier. A small peak of NO_2 values can be observed at distances between 320-350 m from the glacier, which had already been highlighted in the previous temperature and relative humidity graphs. This fact is clearly visible in the Figure 4.56 left, with yellow dots at about 350 m.

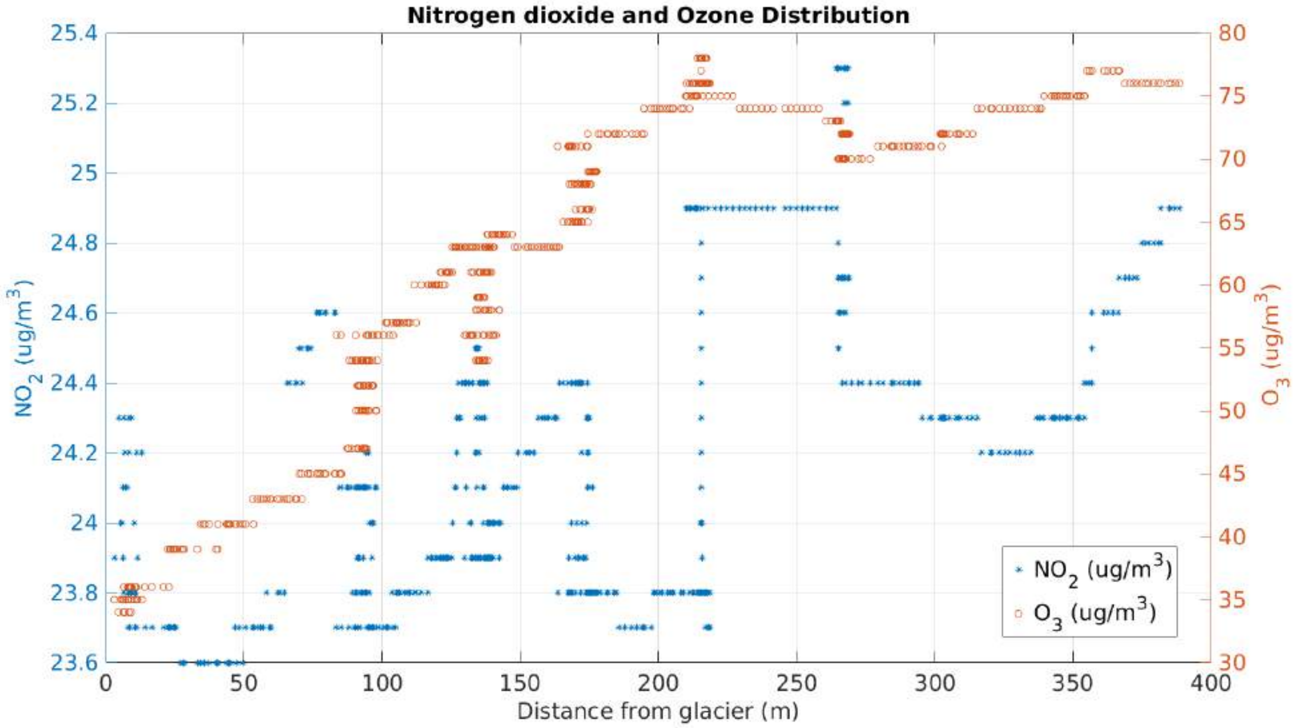

Figure 4.55 - Trends of NO$_2$ (ug/m^3, left y-axis, blue dots) and O$_3$ (ug/m^3, right y-axis, orange dots) as a function of the distance from the front of the Blomstrandbreen glacier (m, x-axis).

As for Ozone, it shows an increasing trend as a function of the distance from the front of the glacier while there are no effects related to the height of the sampling, as also confirmed by the graph in Figure 4.56, right.

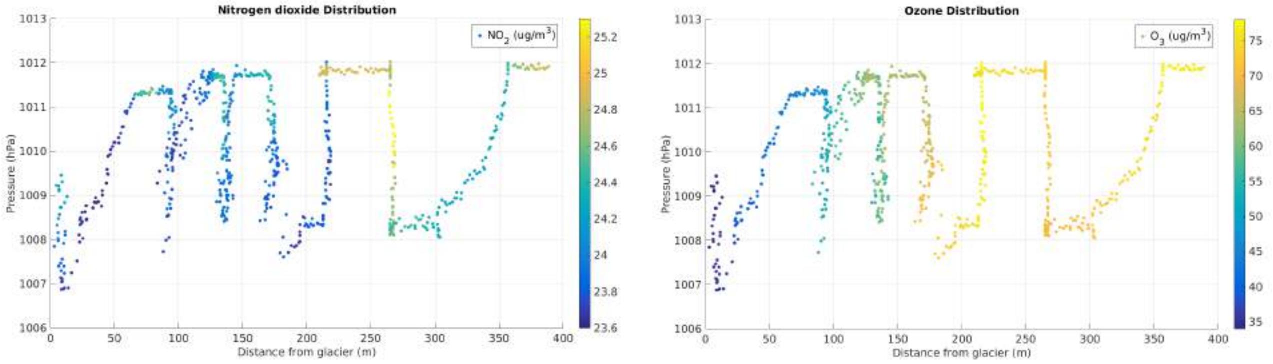

Figure 4.56 - Left: variation in NO$_2$ (ug/m^3; yellow = high NO$_2$; blue = low NO$_2$) as a function of pressure (hPa, y-axis) and distance from the front of the glacier (m, x-axis). Right: variation in O$_3$ (ug/m^3; yellow = high O$_3$; blue = low O$_3$) as a function of pressure (hPa, y-axis) and distance from the front of the Blomstrandbreen glacier (m, x-axis).

The behavior of the NO$_2$ is different: there is a general tendency to increase with the increase in the distance from the front of the glacier but in the same time there are variations along the vertical profiles, with a slight decrease in correspondence with the increase in the height of the acquisition system with respect to sea level (Figure 4.56, left).

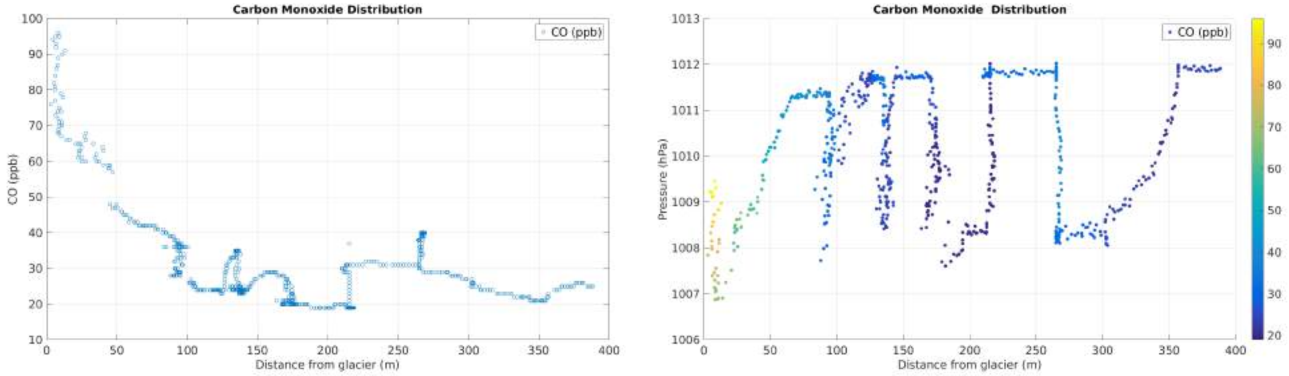

Figure 4.57 - Left: Trend of CO (ppb) as a function of the distance from the glacier front (m). Right: variation in CO (ppb; yellow = high CO; blue = low CO) as a function of pressure (hPa, y-axis) and distance from the front of the Blomstrandbreen glacier (m, x-axis).

Concerning Carbon monoxide (CO), the graphs in Figure 4.57 show a decreasing value of CO with increasing distance from the glacier and no dependence from the vertical movement of the system. In this case, the values are well below the mean values registered for the Svalbard area (about 115 ppb).

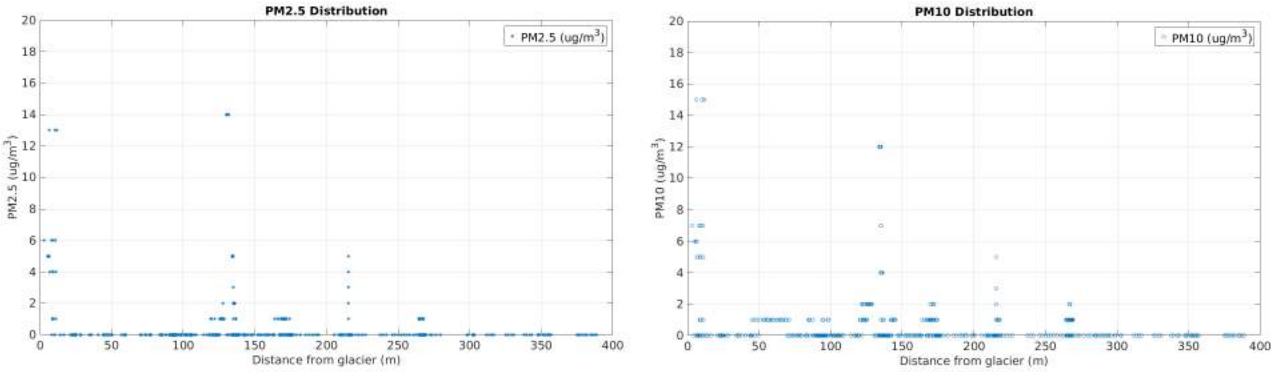

Figure 4.58 -Left: Trend of PM2.5 (ug/m^3) as a function of the distance from the glacier front (m). Right: Trend of PM10 (ug/m^3) as a function of the distance from the Blomstrandbreen glacier front (m).

Near the Blomstrandbreen glacier, some small values in the PM2.5 and PM10 sensors were detected. However, these variables do not present any type of trend as a function of the distance from the glacier, showing that no significant source of particulate matter is present in the area.

All the values obtained during these tests were compared with the values obtained from an AirQino system deployed on the roof of the Gruvebadet laboratory, an instrumented shack roughly 1 km away from the research village of Ny-Ålesund. The shack is 67 m above sea level and is located so as to avoid any contamination from the Ny-Ålesund settlement. This AirQino system was left in place for one year (30 March 2017 – 29 March 2018) to register a consistent data series, capable of capturing the main seasonal trends and characteristics of the lower troposphere. For more details on the datasets and on the graphs obtained refer to (Carotenuto et al., 2020). The comparison shows a good agreement of the short term dataset with the long data series.

Before concluding, one more thing should be observed: some of the graphs of the variables examined above (temperature, RH, NO_2, O_3) show a trend that differs from the average trend in the area which is about 260 m away from the front of the Blomstrandbreen glacier. This anomaly in the trends of the variables can be observed along the vertical profile. It is possible only to make assumptions about the cause of these peaks (negative or positive depending on the variable) that emerge from the trend: they can probably be related to a malfunction of the acquisition system or to the presence of modified air due to wind currents transporting the exhaust of the MS Teisten used to support the operations. Although it is not possible to trace the cause of the anomaly, it is nevertheless important to underline how the system (AirQino mounted on the robotic platform PROTEUS) is able to highlight even minimal variations in the distribution of the atmospheric parameters and possibly be able to trigger an alert signal. This fact is very important also in a perspective of using autonomous robotic platforms for hazard detection and for implementation of risk mitigation procedures, even in situations where the anomaly is of short duration over time, such as in the case of air where the mixing effect is much faster than in water.

Chapter 5

Scoglio d'Affrica (Northern Tyrrhenian Sea): seabed gas emission observations

Seepage represents an important route of transport for methane (CH_4) and other hydrocarbon gases from Earth's subsurface to the oceans and the atmosphere. When CH_4 comes in contact with seawater, it provides energy to drive chemosynthetic microbial activity. Escaping CH_4 can then contribute to the atmospheric CH_4-pool where it acts as a strong greenhouse gas. Finding the locations of CH_4-seepage, tracing the origin of the CH_4 and identifying abiotic vs. biotic processes occurring at CH_4 seeps is therefore of fundamental importance for understanding the global carbon cycle and its interaction with the biosphere (Meister et al., 2018).

Surveys to observe gas emissions in the area of the Scoglio d'Affrica were carried out by the Geological Service since the 1960s and 1970s and were described in (Barletta et al., 1969). These identify the presence of morphological terraces, structures affected by fault dislocations and structural lineations potentially capable of conveying deep fluids. Direct observations indicate a widespread and continuous degassing activity, and the gas was found to be mainly methane (Chiocci et al., 2017). These emissions phenomena affect, more generally, the Tyrrhenian area, presenting different characteristics based on the geomorphological context in which they originate.

5.1 Geological and morphostructural setting of the area

The Scoglio d'Affrica, also known as Formica di Montecristo, is a small islet of the Tuscan Archipelago located offshore in the waters between the Tyrrhenian Sea and the Corsica Channel and from an administrative point of view it belongs to the Municipality of Portoferraio (LI). It is located at N42°23.740' - E10°05.567', about 23.5 km (14.6 nautical miles) south of the island of Pianosa and about 18.5 km (11.5 nautical miles) west of the island of Montecristo (Motteran and Ventura, 2005).

Figure 5.1 – Map showing the location of the Scoglio d'Affrica (Tuscan archipelago) in the waters between the Tyrrhenian Sea and the Corsica Channel.

The Scoglio d'Affrica represents the southernmost part of the ridge of Elba, a tectonic structure consisting of sedimentary deposits of the predominantly Cenozoic age. The ridge of Elba develops from Capraia (volcanic origin) to Monte Capanne all'Elba (plutonic origin) to Pianosa (sedimentary origin, myopliocene age) to the Scoglio d'Affrica (sedimentary origin). Montecristo Island, not far away, is also of plutonic origin, like Monte Capanne. (Figure 5.2) (Chiocci et al., 2017).

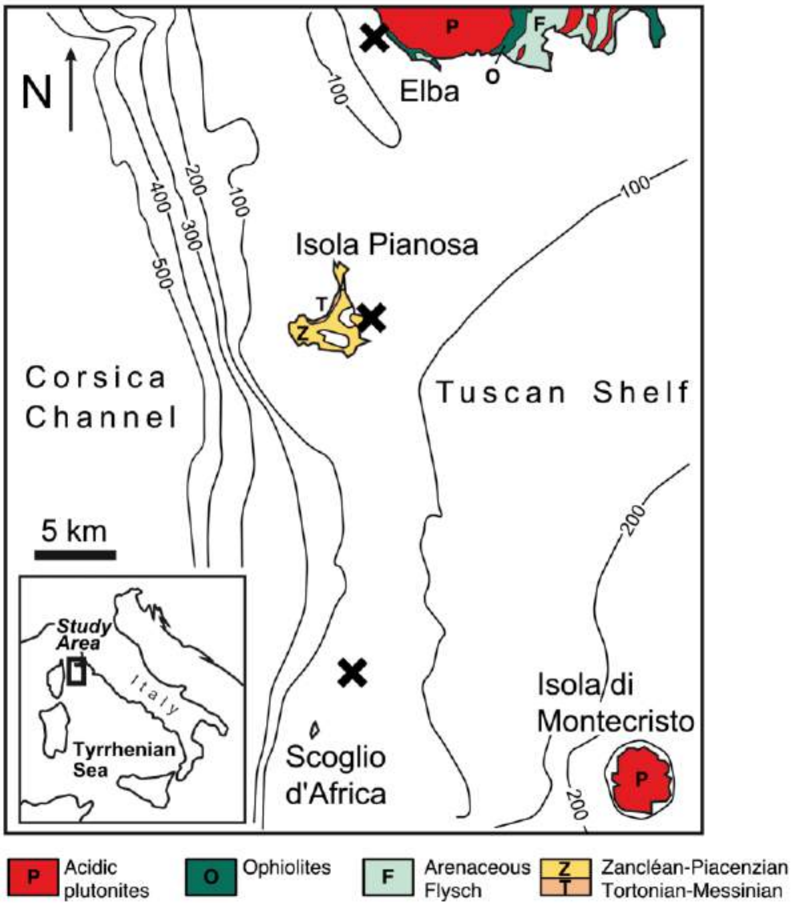

Figure 5.2 - Map of the Tyrrhenian Sea showing the geological characteristics (with different colors) and the locations of some hydrocarbon gas seeps (crosses) near Pomonte (Island of Elba), the island of Pianosa and the Scoglio d'Affrica (Meister et al., 2018).

This ridge, stretching towards N-S, is located at an average depth of about 70-80 m which, in proximity of the islands, drops sharply to about 20 meters, reaching 7-8 m in some points. It divides the northern Tyrrhenian basin into two parts: the one in the West, between the same ridge and the island of Corsica where high depths of around 800 meters are quickly reached (already less than 5-6 km from the western coast of the islands) and the one to the E-NE where the ridge slopes towards the continental shelf with average maximum depths around 150 meters. In the area between the Scoglio d'Affrica and the Island of Montecristo the depths reach maximum depths of about 200 m, while between the latter and the Island of Giglio a deep pit begins which reaches about 540 m in depth (Figure 5.3) (Motteran and Ventura, 2005).

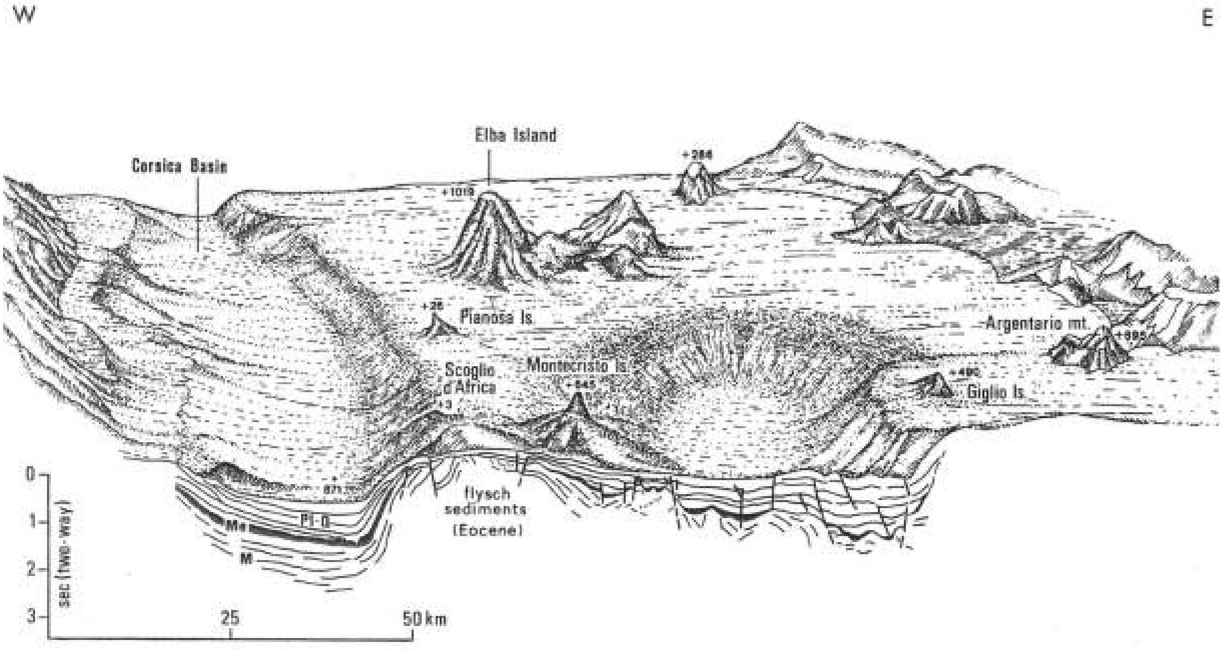

Figure 5.3 - Diagram of the main morphologies of the central Tyrrhenian basin (Wezel, 1982)

The portion of the ridge where the Scoglio d'Affrica is present consists of a core of calcareous sediments coeval with the Tuscan aquifer on which the most recent organogenic limestones, referring to the Pleistocene-Holocene interval, rest in transgression, as confirmed by reflection seismic studies (Motteran and Ventura, 2005).

More details on the seabed are provided by a series of geomorphological studies conducted in the years 1964-69 by the Geological Service of Italy. The studies (Barletta et al., 1969), carried out within the isobath -30 m, highlight the presence of morphological terraces, structures affected by fault locations and widespread methane production (Motteran and Ventura, 2005).

The sedimentological analyzes carried out show that the minerals present on the seabed between the Pianosa Island and the Scoglio d'Affrica are mainly manganese and calcite and to a lesser extent aragonite; from the granulometric point of view, there is a clear prevalence of sands (90%), alongside detrital material of bioclastic origin (gravel 6.5%) while the presence of clay sediments is rather reduced (silt 1%, clay 2.5%).

More recent seismic surveys (Cornamusini et al., 2002; Pascucci et al., 1999) show that the Scoglio d'Affrica presents chaotic or almost transparent seismic facies similar to that described for the structural high of the Formiche di Grosseto (to the east of the high structural of Montecristo) and referring to the Liassic limestones of the Falda Toscana. These studies also highlight the presence, around the island, of a series of high-angle normal faults active during the post-Burdigalian period (Figure 5.4)(Cornamusini et al., 2002; Motteran and Ventura, 2005).

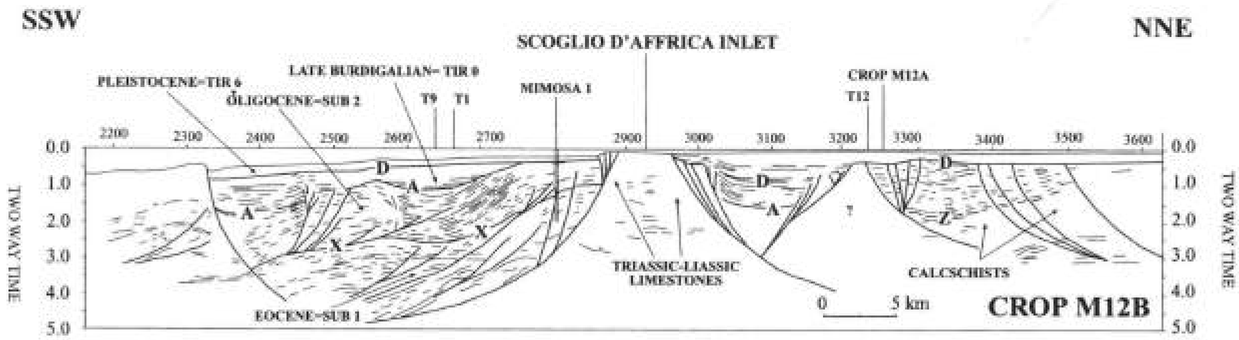

Figure 5.4 - Drawing lines of the seismic profile CROP M12B. Z, base of the Eocene deposits; X, base of oligocene deposits; A, base of the deposits of the upper Burdigaliano - ? Serravalliano; B, base of the deposits of the upper Miocene (Cornamusini et al., 2002).

These observations should be considered in the more general context of the Tyrrhenian Sea, which, during the Late Miocene (8.5–6.85 Ma ago), opened as a back-arc basin between the Apennine and Corsica/Sardinia. This post-collisional extension of the Apennine has caused lithospheric thinning and related melting of the asthenosphere. These mantle melts interacted with the rifted crust to produce varied intermediate to felsic intrusive bodies. Today, the northern Tyrrhenian Sea is characterised by relatively thin crust on the order of 22 km and a shallow asthenosphere at 50 km depth. In areas of the Tyrrhenian Sea and Western Apennines region, where the magmatic intrusions are most recent, heat flow is high, especially in Tuscany. Scoglio d'Affrica sits on top of a fault-bounded horst structure consisting of Triassic-Liassic limestone, as observed by seismic inspections (Cornamusini et al., 2002; Meister et al., 2018).

5.2 Magnetic anomalies setting

The Northern Tyrrhenian Sea contains an intense positive N-S-trending magnetic anomaly and the island of Elba is located at the eastern margin of this high-intensity magnetic lineation (see Figure 5.5). From the analysis of and gravimetric data, it is possible to infer that the intense N-S magnetic alignment in the Northern Tyrrhenian sea is the expression of a segment of oceanic upper mantle and crust of the Jurassic Tethys. The oceanic rocks have been emplaced in the Alpine Apenninic orogen (ophiolitic suture zone) that, subsequently, through rifting processes, evolved into the opening Tyrrhenian with subsequent basin formation (Eriksson and Savelli, 1989).

Measurements of magnetic susceptibility of the different lithologies that characterise the ridge indicate that only the peridotites (serpentinites), which are associated with other ophiolitic rocks such as gabbro, diabase and siliceous sediments, possess such a high magnetic susceptibility (4000-10,000×10^5 SI units)(Caratori et al., 2004; Cassano et al., 2001; Eriksson and Savelli, 1989).

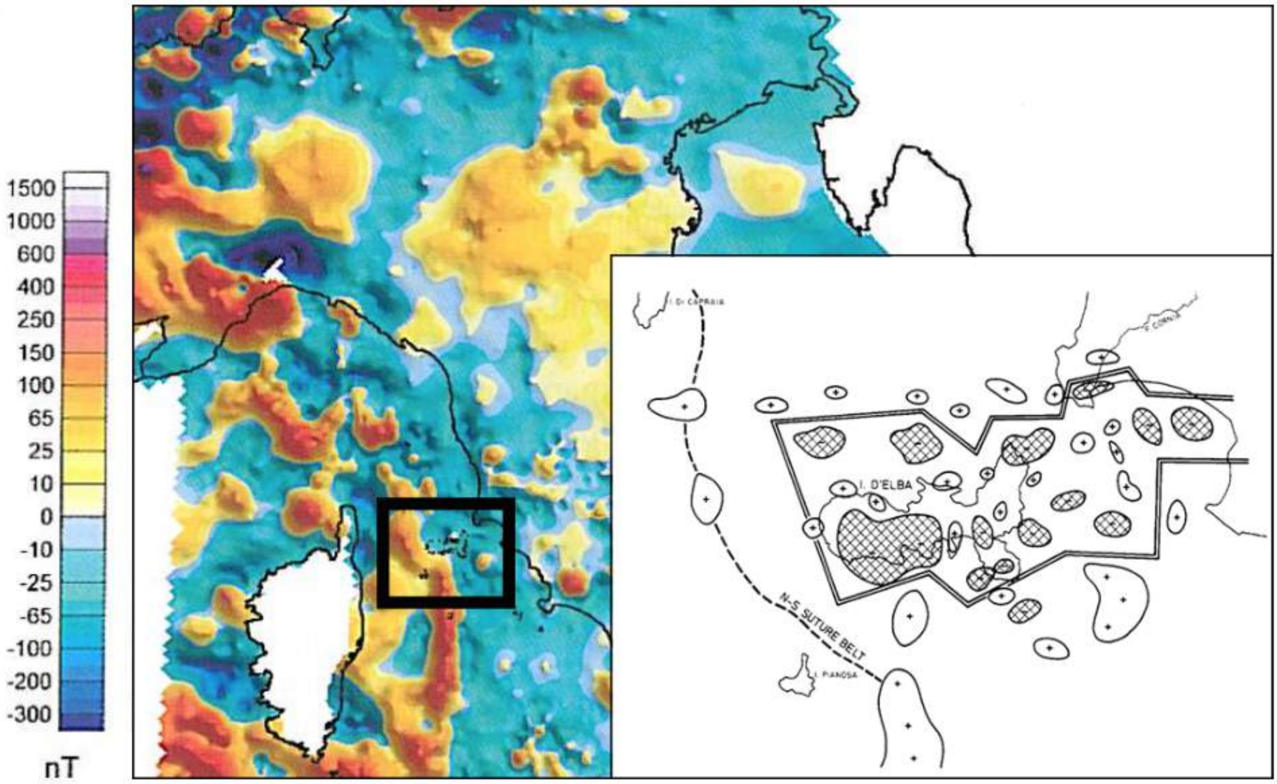

Figure 5.5 - Map of the magnetic anomalies of Italy in Chiappini et al. (2000), modified, and non-magnetic intrusive bodies surrounded by the positive anomalies of the ophiolytic bodies in Eriksson and Savelli (1989).

Two major W-E magnetic alignments delimit the Northern Tyrrhenian. These are the Elba lineation to the north and the lineation of the 41 ° parallel to the south (lines n. 2 and n. 5 in Figure 5.6).

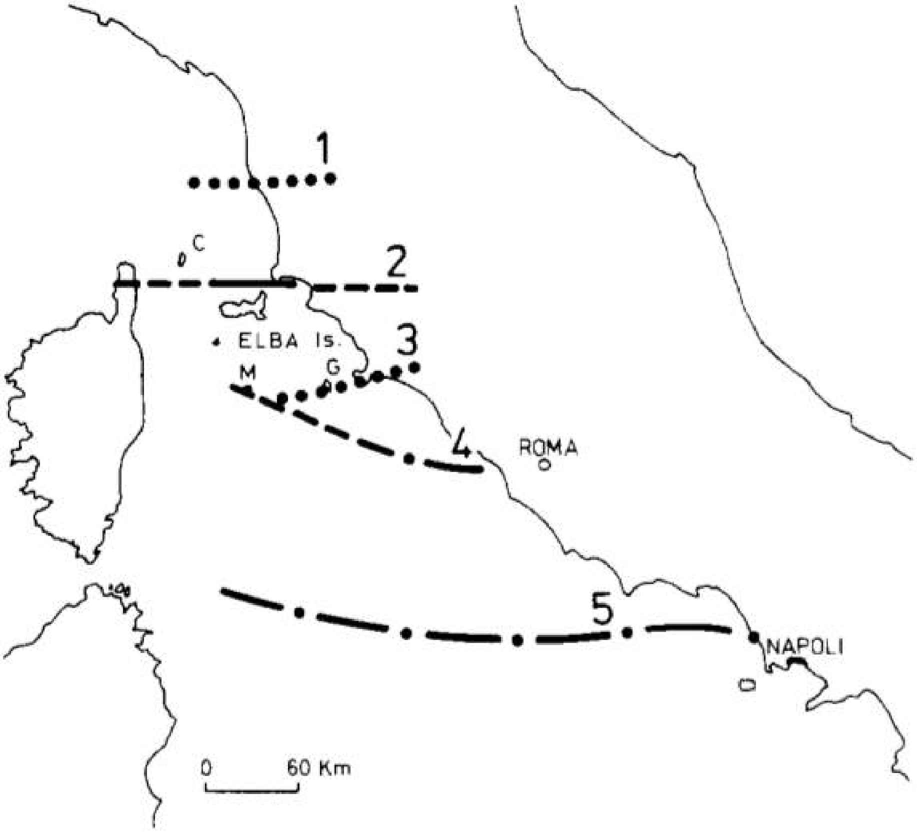

Figure 5.6 - Main W-E tectonic lineaments interpreted from magnetic data. 1=the Livorno lineament; 2=the Sisco (North-West Corsica) Elba Amiata volcanic lineament; 3=the Montecristo islet Vulsini volcanic lineament; 4=the Montecristo islet Tiber mouth lineament; 5=the lineament of the 41 ° parallel. C, M and G -- islands of Capraia, Montecristo and Giglio (Eriksson and Savelli, 1989).

Both these lineations are of magmatotectonic nature and are characterised by an overall migration of magmatic events to the east and so they could be interpreted as the expression of deep sinistral transcurrent faults, resulting in high heat flow, extensive melting and underplating in the lower crust (Eriksson and Savelli, 1989). Moreover, moving towards south in Tuscan domain, along N-S fault, there is clear evidence of off-shore gas seepage (mainly CH_4), which can be related to the recent extensional activity (Sciarra et al., 2019).

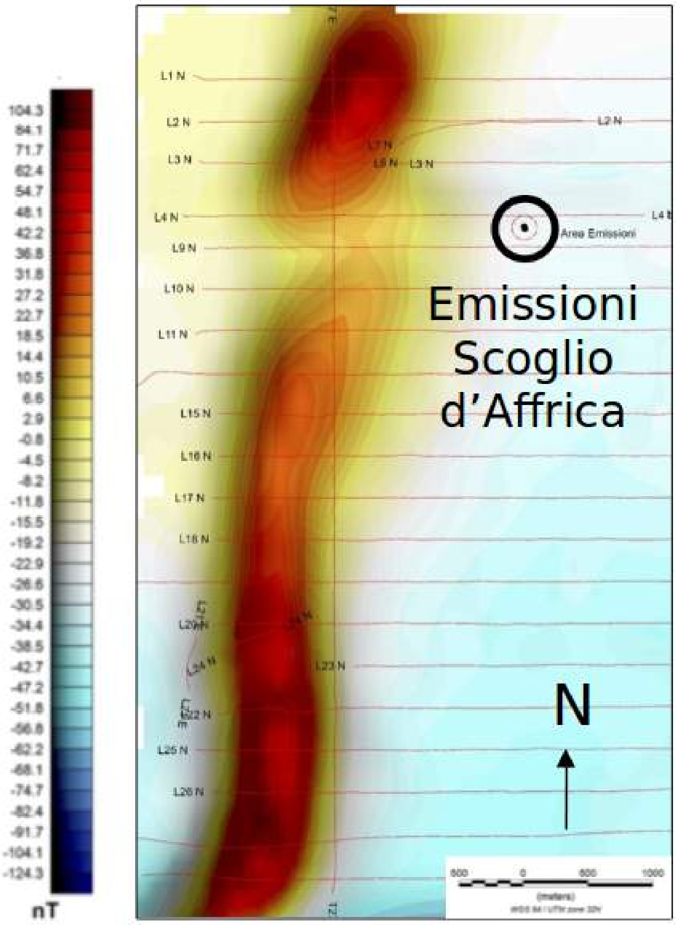

Figure 5.7 - Magnetic anomaly map near the emissions of the Scoglio d'Affrica, in INGV – Rapporto Tecnico, 2017.

5.3 Introduction on methane emissions

A cold vent (also called a cold seep) is an area of the ocean floor where hydrogen sulfide, methane, and other hydrocarbon-rich fluid seepage occurs, often in the form of a brine pool. Cold seeps occur over fissures on the seafloor caused by tectonic activity. Oil and methane "seep" out of those fissures, get diffused by sediment, and emerge over an area several hundred meters wide. Cold seeps constitute a biome (very large ecological areas, with fauna and flora (animals and plants) adapting to their environment) supporting several endemic species. Cold seeps develop unique topography over time, where reactions between methane and seawater create carbonate rock formations and reefs. This kind of seepage activities have no depth boundaries, having been found in both shallow water as well as in deeper depths (Joseph, 2017).
It is important to find and understand such seeps because they have global significance for the transfer of methane carbon from long-term storage in ocean-floor sediments into the ocean and atmosphere. Methane released into the water column is often oxidized to carbon dioxide, leading to changes in ocean chemistry, such as ocean acidification. Locating seeps will expand opportunities for researchers to study how seeps in the ocean environment affect ocean chemistry (Joseph, 2017).

Despite the importance of these seepage of methane (CH_4) that affect affect Earth's biogeochemical cycles, processes of CH_4 generation and consumption, both abiotic and microbial, are not always clear (Meister et al., 2018). This fact is particularly true for Geological CH_4 (geo-CH_4) seepage, i.e. the natural component of fossil fuel (^{14}C-free) emission. Geological CH_4 sources are from the natural degassing of hydrocarbons from the Earth's crust. Geo-CH_4 originates in deep rocks by biotic processes (decomposition of organic matter): methane is produced either by microbial methanogenesis or by thermal breakdown of larger organic molecules at higher temperatures (i.e. microbial and thermogenic). Relatively minor amounts of CH_4 can also be produced by abiotic processes in crystalline basement, which do not involve organic matter in rocks. The abiogenic formation of CH_4 is fuelled by dihydrogen (H_2), which forms as a result of subsurface water-rock interactions, such as serpentinization of ultramafic rocks. Abiogenic CH_4 is predominantly released from hydrothermal vent systems along oceanic spreading centres, such as the Lost City Hydrothermal Field in the central Atlantic. Abiogenic CH_4 seeps related to serpentinization also occur in shallow water or even on land (Meister et al., 2018).

Surface emissions of geological CH_4 occur through the process known as "gas seepage", which includes point sources (gas–oil seeps, mud volcanoes (MVs), springs, geothermal manifestations (Gms)) and area sources (diffuse "microseepage", MS). Once considered a minor natural CH_4 source globally, geological degassing is today recognized as a major contributor to atmospheric CH_4.

Summarising, four traditional categories of natural geo-CH_4 emissions and a fifth, recently discovered, are documented in the literature and shown in Figure 5.8 (Etiope et al., 2019):

- onshore hydrocarbon macro-seeps, including mud volcanoes,
- submarine (offshore) seeps,
- diffuse microseepage,
- geothermal manifestations,
- seepage from serpentinised peridotites.

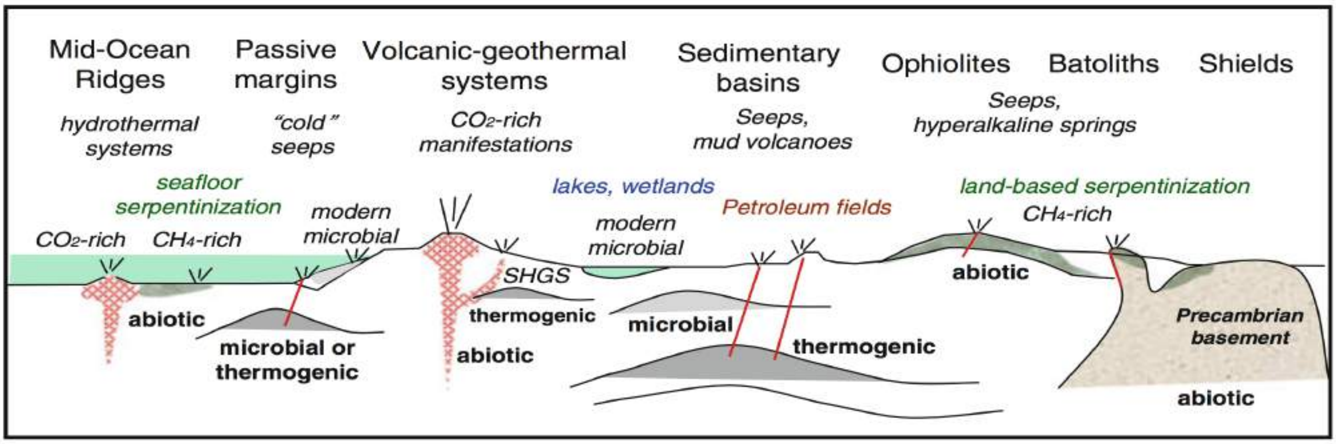

Figure 5.8 - Geological environments of methane production (Etiope, 2015).

Typically, the geochemical analysis of collected gas samples is used to trace the origin of the seepage. Stable carbon and hydrogen isotope compositions of CH_4 released is analysed. In particular, $^{13}C/^{12}C$ ratios are reported as $\delta^{13}C$ values ($1\ \sigma = 0.1‰$) against VPDB (Vienna Pee Dee Belemnite) standard and $^{2}H/^{1}H$ ratios are reported as $\delta^{2}H$ values ($1\sigma = 1‰$) against VSMOW (Vienna Standard Mean Ocean Water) standard. Helium isotope composition (expressed as R/ R_a, which is $^{3}He/^{4}He$ of the sample versus the same $^{3}He/^{4}He$ ratio in atmosphere, $R_a = 1.386 \times 10\ {-6}$) is also calculated to understand the origin of the seepage (Sciarra et al., 2019).

By graphically representing these values, we can see that methane of different origin has isotopic signature positioned in different areas of the graph, as shown in the Figure 5.9.

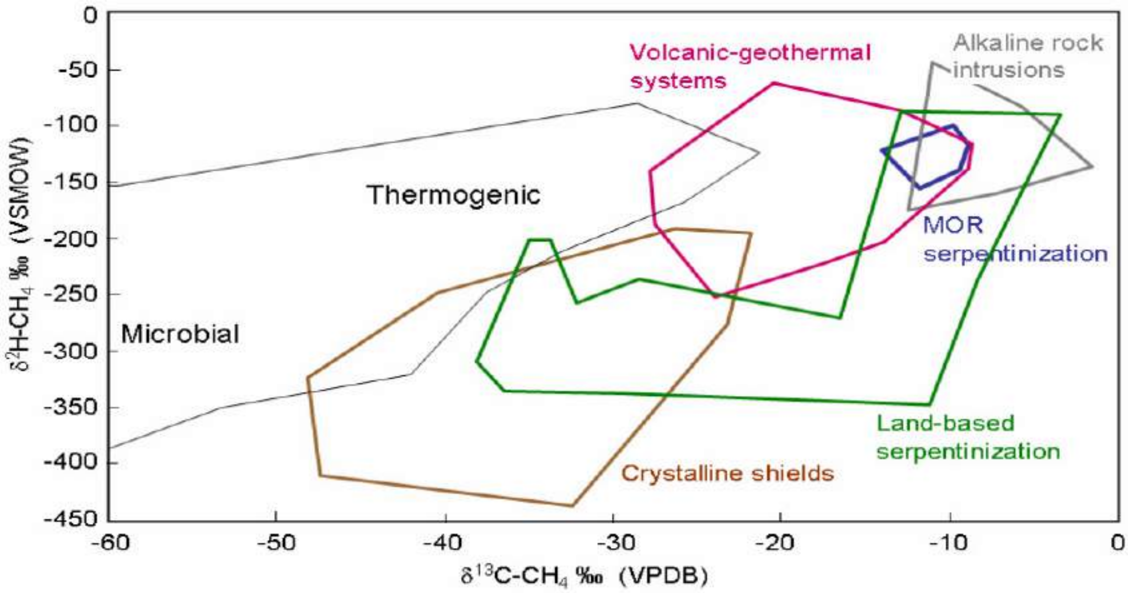

Figure 5.9 - Graph of $\delta^{13}C$ *values versus* $\delta^{2}H$ *values for methane, showing different isotopic signature depending from biotic or abiotic origin of the gas (Etiope et al., 2017).*

For example, thermogenic CH_4 is generally less depleted in ^{13}C compared to microbial CH_4, as during the thermogenic breakdown of hydrocarbons, CH_4 largely inherit the isotopic composition of the organic matter, modified only by minor kinetic fractionation. In contrast, microbial CH_4 can be very strongly depleted in ^{13}C, due to kinetic isotope fractionation by microbial enzymatic path-ways of methanogenesis (Meister et al., 2018).

Another issue connected to this kind of events is the temporal variability of geological methane emissions. The fluxes of natural gas seepage from the Earth's crust are not constant, either on short (hours, days, months, seasons) or long (years, centuries, millennia) timescales. Seepage variations can be induced by endogenous (geological) and exogenous (atmospheric) factors, including subsurface gas pressure variations (controlled mainly by gas migration and accumulation processes), changes of fracture permeability (tectonic stress, seismicity), hydrostatic aquifer variations and meteorological and climatic changes (atmospheric pressure, temperature, humidity and microbiological activity in the soil) (Etiope, 2015). Mud volcano episodic eruptions (Mazzini and Etiope, 2017), seismicity-related degassing (Manga et al., 2009) and seasonal variability of microseepage (higher in winter due to lower methanotrophic consumption in the soil;

Anthropogenic activity, through modification of aquifer pressures (water pumping) and petroleum exploitation (with consequent decrease of reservoir pressures) can also induce seepage variability over time (Etiope, 2015). Specific empirical studies are however missing, and with the present state of knowledge it is impossible to provide a temporal variability factor. On longer, geological timescales, a series of proxies suggested that geo-CH_4 emissions could have been quite variable over the Quaternary period (Etiope et al., 2008; Etiope and Schwietzke, 2019).

5.3.1 Gas seeps in the Tyrrhenian Sea: occurrence and distribution

Many seeps and hydrothermal systems producing various amounts of CH_4 from the areas of the Tyrrhenian Sea and along the Italian peninsula are known. Probably all types of CH_4 seeps occur, depending on the tectonomagmatic and sedimentary setting (Meister et al., 2018).

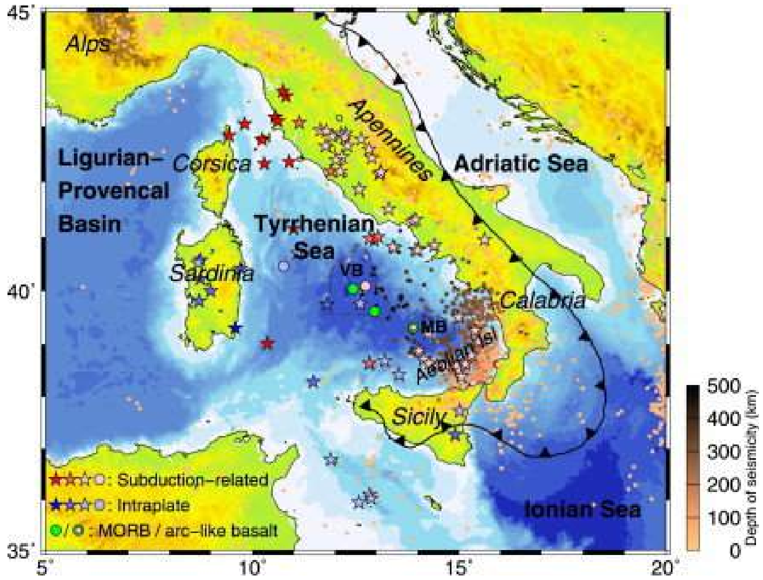

Figure 5.10 - Tectonic map of the Tyrrhenian Sea area. The plate boundary along the Adriatic and Ionian arc is shown as thick black line with triangles indicating the sense of subduction. The Vavilov Basin (VB) and Marsili Basin (MB) are outlined by dashed lines. Volcanic centers are indicated by stars and samples from deep drill holes by outlined circles. Different rock types are represented by different color, as in the legend (Greve et al., 2014) .

They can be subdivided into four regional domains based on the geological setting and geochemical properties of the emanating fluids:

- the Latio-Umbria region and Tuscan Magmatic Province (e.g. Larderello and Mt. Amiata hydrothermal springs) are grouped as “Tyrrhenian” domain that is largely associated with the back-arc extensional regime;
- admixture of CH_4 with volcanic gas at Vesuvio, Campi Flegrei, Panarea and Pantelleria result from interaction with calc-alkaline rock;
- mud volcanoes occurring frequently along the Appennine and Adriatic coast are releasing microbial or thermogenic CH_4 from a thick pile of sedimentary nappes along the Adriatic thrust front;
- abiogenic CH_4 is released from hyperalkaline springs related to serpentinization of Ligurian ophiolites near Genova (Meister et al., 2018; Rovere et al., 2014).

5.3.2 Scoglio d'Affrica emission site

The seabed gas emissions in the area of the Scoglio d'Affrica are studied since the sixties and recently they return to great interest due to an episode that occurred in March 2017, when fishermen reported that an outburst of gas rose about 10 m near their boat. The phenomenon persisted for about 15 minutes and then decreased, transforming into emissions of "clear water" bubbles.

After this episode, numerous data acquisition campaigns were carried out by various subjects (public and private research centers) interested in the study of the phenomena that occur in the area. The most recent data acquisition campaign is the one carried out in June 2019 by Italian Navy Hydrographic Office (IIM), the National Institute of Geophysics and Volcanology (INGV), the INstitute of Marine engineering (INM) Genoa of the CNR, University of Ferrara (UniFe) and University La Sapienza (Roma1) and it will be described in detail in the following chapters.

The knowledge acquired during these campaigns has highlighted the presence of dozens of emission points located on seabed of various nature: sandy bottom with ripple, sandy bottom with sub-metric and metric blocks, detrital bottom with sub-angular fragments of heterometric dimensions. The emissions observed are punctual, gaseous, sometimes intermittent, as visible in Figure 5.11. Bubbles emissions appeared to be concentrated in the shallower parts of the seabed, between the depths of 8 and 10 m, decreasing going towards deeper bottoms. Sometimes the emissions emerge from the contact between the blocks/rocky outcrops and the sandy sediment, sometimes in correspondence of the emissions there are evident erosive forms (minipockmark) of decimetric dimensions. Blocks covered with probable bacterial matte were also observed (INGV - Rapporto tecnico, 2017).

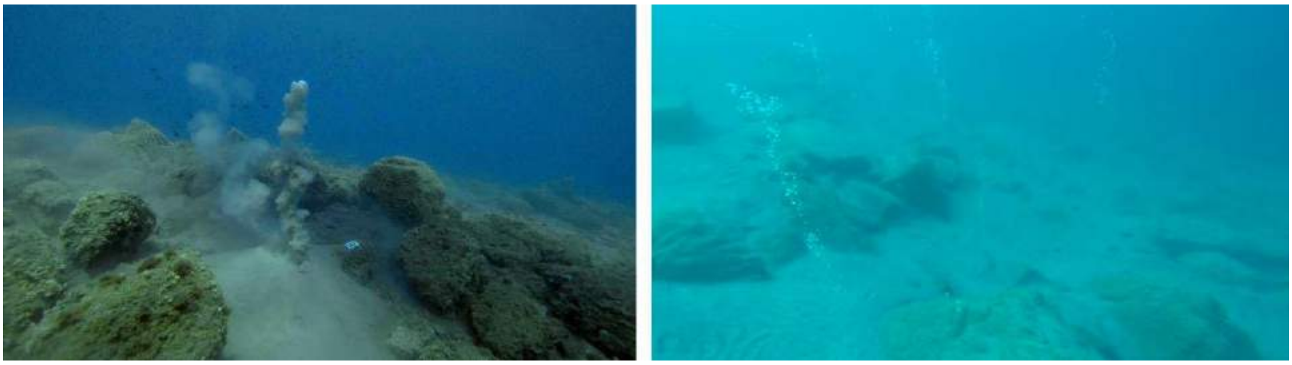

Figure 5.11 – Examples of methane emissions observed in the Scoglio d'Affrica area (INGV - Rapporto tecnico, 2017)

Violent expulsion of fluids from the seabed, such as that described in March 2017, generally involve the formation of craters (pockmarks) of sizes varying between a few meters and tens or hundreds of meters and/or the accumulation around the point of emission of debris or sediment expelled from the seabed. In the latter case, we speak of mud volcanoes. Pockmark-like structures have been observed on the Elba ridge, to the north of the island (INGV - Rapporto tecnico, 2017).

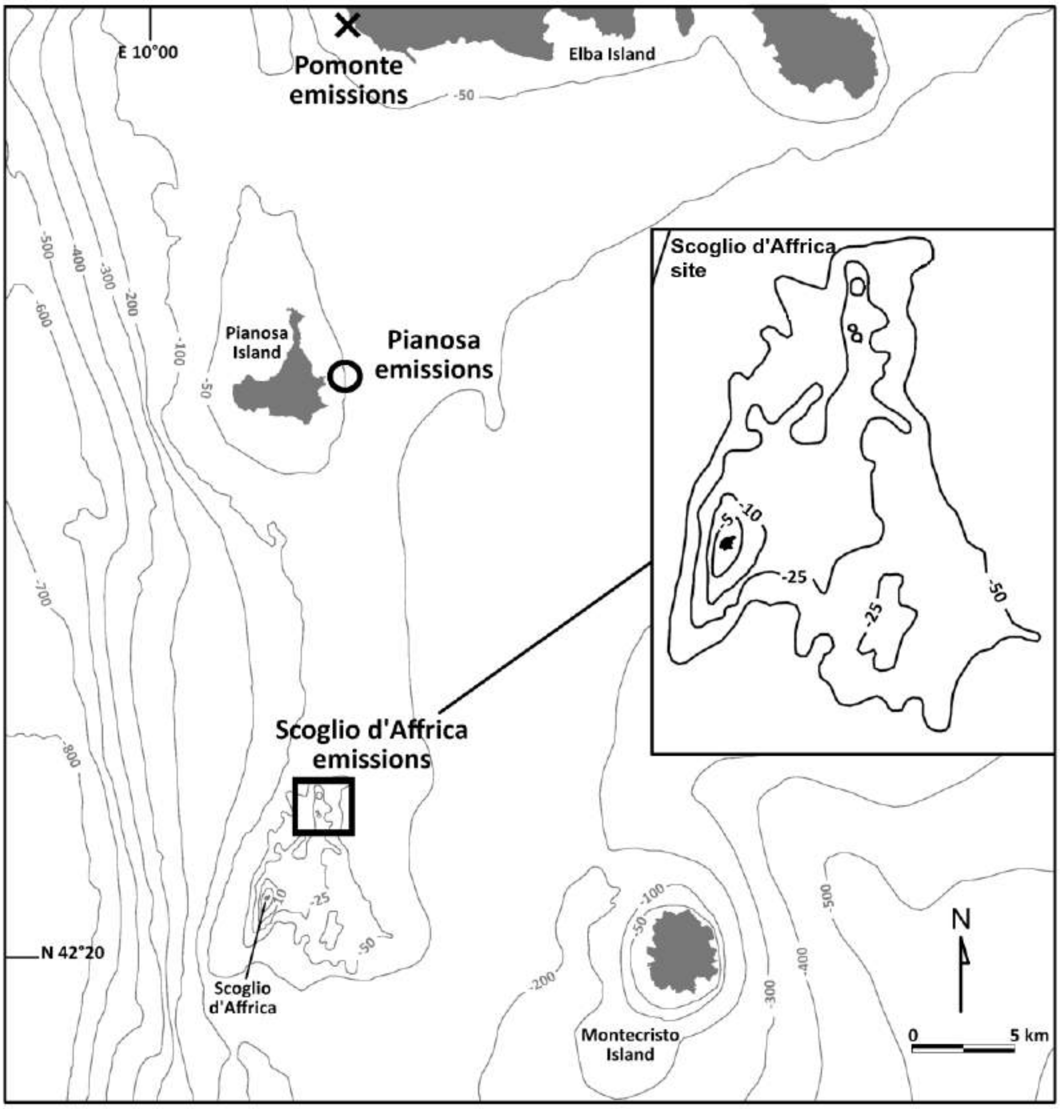

Figure 5.12 - Bathymetric map of the area between the island of Elba and Montecristo showing the location of Scoglio d'Affrica emission site (about 40 km south of Elba), Pomonte seeps and Pianosa emission site. All three sites of hydrocarbon seepage follow a North-South transect (Meister et al., 2018).

5.3.3 The discovered Mud Volcano: geochemistry and origin of methane at Scoglio d'Affrica.

In this context, cold methane seeps discovered in the sedimentary basin near the Scoglio d'Affrica show the conical shapes and the typical acoustic backscatter signature (obtained by a high resolution multibeam) of other mud volcanoes. Generally, mud volcanoes are the shallow expression of subsurface processes characterised by movements of large masses of sediments and fluids. A marine mud volcano is a window into different depth levels of the submerged geosphere where hydrogen sulfide, methane and other hydrocarbon-rich fluid seepage occurs caused by tectonic activity. Indeed, vertical migration of geogas, especially CH_4 from the reservoir strata to the seafloor occurs along focused, permeable migration pathways, often created by faults and fractures (Sciarra et al., 2019).

The sampled gas chemistry is typical of mud volcanoes, with methane as the prevalent gas component (>95 vol%) and minor gases that include carbon dioxide, nitrogen and trace amounts of helium. The combined stable C and H isotope composition of CH_4 ($\delta^{13}C$ and δ^2H) highlights a thermogenic origin of methane discharged from mud volcano in the Scoglio d'Affrica site (magenta dots in Figure 5.13), contrary to likely abiotic origin gas found in the Pomonte seep and linked to serpentinized ultramafic rock systems (green triangles in Figure 5.13).

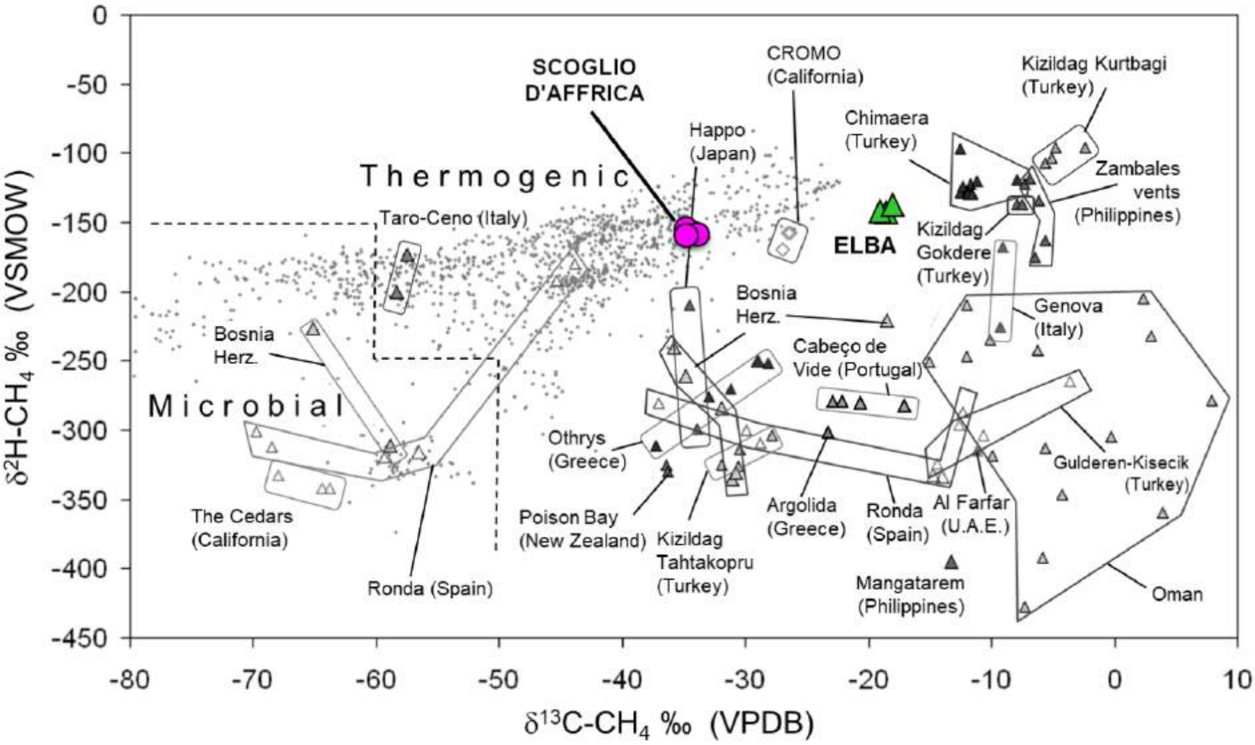

Figure 5.13 - $\delta^{13}C$ vs δ^2H diagram of methane: gas from mud volcano in the Scoglio d'Affrica site is of thermogenic origin and shown in magenta dots;gas emissions in the Elba site is of abiotic origin and shown with green triangles. Emission from other sites in the world are reported for comparison (Sciarra et al., 2019).

The isotopic diagram, however, is only the first step for determining the abiotic origin of gas and it cannot reveal if CH_4 is completely abiotic or mixed with some biotic components. Additional interpretative tools are necessary and may include the use of noble gases (helium isotopes), Schulz-Flory distribution tests, the molecular and isotopic composition of associated gases, and methane vs. ethane mixing plots (Etiope and Sherwood Lollar, 2013). For example, the samples collected on the Scoglio d'Affrica mud volcano are extremely depleted in ^3He and their $^3He/^4He$ ratios are typical for a geological setting in which radiogenic crustal helium is strongly predominant. On the contrary, the Pomonte ophiolitic gas seeps show a mantle-derived ^3He-rich component estimated in the range between 10 and 15% (Sciarra et al., 2019).

Moreover, knowledge of the geological context is an essential precondition for final interpretations. Actually, in many cases emissions can be not totally abiotic and they may have variable components of thermogenic or microbial gas (Etiope and Schoell, 2014).

Although a different origin of methane has been observed in the emissions of the area between the Elba and the Montecristo island, there is a characteristic that unites them: the low temperature of the geological system. Measurements suggest that the gas is produced at temperatures typically <100°C (in contrast with hydrothermal mid-ocean ridge systems that can overcome 200°C) (Etiope, 2017).

In conclusion we can say that, based on morphological, sedimentary and geochemical characteristics of the solid materials and the fluids expelled from the Scoglio d'Affrica site, these seeps can be classified as a mud volcano.

In the next chapters, the data acquisition campaign carried out in 2019 will be described in detail and the data collected will then be shown and analysed.

Chapter 6

Methods and technologies for seabed gas emissions observation and monitoring in Northern Tyrrhenian Sea

Marine environmental monitoring focuses on current status and possible changes detection in the behavior and characteristics of key parameters and objects of interest related to the environment. The selection of parameters to monitor is based on the best available understanding of the resources, processes and other relevant qualities present in the area of interest. Efficient monitoring depends on the ability to acquire relevant data at relevant temporal and spatial resolution to optimize information for knowledge-based decisions. Dependent on the environment, there will be a minimum set of parameters that always should be measured, either as an essential or supporting parameter for interpretation of other data gathered. In addition to measurements of essential parameters, the quality of the data interpretation is dependent on the spatial and temporal resolution and coverage of the data. Moreover, the data are characterised by specific “data request”, a set of data attributes or qualities such as resolution, sampling rate and quality, required to answer the mission objective. Based on the data request, selections of sensors, platforms and parameters are made within appropriate temporal and spatial ranges, coverage and resolutions (Nilssen et al., 2015).

The planning of a monitoring mission and the operational procedures for its execution must therefore take into account on the one hand the objectives of the mission and on the other the operational constraints such as the availability of appropriate technology and methods, environmental limits and possible dangers, in the case of operations in situations of risk. While surveys have traditionally been performed as ship campaigns with temporal and spatial resolution limited to the capabilities of the ship with its installed sensors, a variety of fixed and mobile sensor platforms now enable gathering of vast amounts of, more or less, continuous or online real-time multisensory data. The need to optimize data sampling has increased the focus also on the ability to modify a real-time mission plan depending on what is being sampled. Reduced mission time, and thereby reduced risk related to the operation, is an additional important advantage of such an adaptive sampling approach. Such an approach would provide more valuable scientific data, in addition to higher temporal resolution and lower power consumption (Nilssen et al., 2015).

An example of phenomena, the observation, study and understanding of which require the integrated use of numerous sensors at different time and space scales, are the gaseous emissions from the seabed. In these cases, the use of robotic vehicles, integrated with traditional monitoring tools, can be the solution necessary to satisfy the numerous requests in terms of spatial/temporal resolution and data quality.

In general, hydrothermal vents and cold seeps are detected and mapped by measuring the intensity and distribution of heat, particles, or other chemical tracers that are introduced to the marine environment by emissions. Because hydrothermal vents and cold seeps cause changes to the chemistry and physical characteristics of surrounding seawater, these geologic features are often surrounded by masses of water that are distinctly different from normal seawater. These water masses (called plumes) provide clues about the location of these seeps. To search for these clues, different kind of sensors are employed to measure chemical and physical water characteristics and detect the presence of hydrothermal vents and cold seeps. Once the plumes have been detected in the water, the depth and size of the plumes are investigated in more detail using instruments that measure conductivity, temperature, depth, optical backscatter, and redox potential so that the source of the plume can be located (Joseph, 2017).

Underwater cameras and biogeochemical sampling devices operated from surface vessels or mounted on submersibles vehicles (ROV, AUV, etc…) are often used in scientific expeditions intended to study the biogeochemical properties of water samples in the vicinity of the seepage area. Moreover, to study long-term changes in a specific seepage site, the monitoring instrument package should be left in place for a long period (weeks or even months) to make repeated measurements of the chemistry, temperature, flow rates, and electrical conductivity of the stream of the seepage (Joseph, 2017).

The following paragraphs describe an experimental campaign carried out in the Northern Tyrrhenian Sea to observe emissions of gas (typically methane) from the seabed. Particular attention will be paid to the operating procedures and the integration of different methods of observation of the environment, necessary to characterise the study area and possibly intervene in the event of an emergency.

6.1 The need for an integrated observing system to study seabed gas emissions in the Tyrrhenian Sea

As described in the previous chapter, the Tyrrhenian Sea, due to its geological structure, is subject in various areas to gas emissions from the seabed. Numerous studies have been done, especially in the southern part of the Tyrrhenian Sea, characterised by very numerous and also very conspicuous degassing events. For example, the Marsili Seamount (Southern Tyrrhenian Sea, Italy), the largest volcano of the Mediterranean area and Europe, is located in the Marsili back-arc basin, to the north of the Aeolian volcanic Arc, and is associated to the subduction of the Ionian slab below the Calabrian Arc (Iezzi et al., 2014). Examples of cold seeps related to this system are mud volcanoes located in the Paola Ridge, along the NW Calabrian margin (SE Tyrrhenian Sea), at a water depth of 500–1000 m, that form plumes in the water column that can reach more that 600 m in height (Rovere et al., 2014). Another active volcanic zone is the area of Ischia Island and Campi Flegrei caldera (Campania) that have been the site of many geothermal investigations, since the early 20th century (Carlino et al., 2015). These are just some examples of sites in the South Tyrrhenian area where numerous experimental investigations have been made over the past few years.

The northern part of the Tyrrhenian Sea is instead characterised by more contained and temporally discontinuous but no less interesting emissions. To this end, a program coordinated by the

Hydrographic Institute of the Italian Navy, together with various research institutes and universities, has been in place for years to monitor and study degassing events in this area.

In this work, the focus will be on the 2019 campaign, carried out by Italian Navy Hydrographic Office (IIM), the National Institute of Geophysics and Volcanology (INGV), the INstitute of Marine engineering (INM) Genoa of the CNR, University of Ferrara (UniFe) and University La Sapienza (Roma1) in the period 4-15 June 2019. The main purpose of this campaign was the mapping of the morphology of the seabed in the area surrounding the Scoglio d'Affrica (west of the Montecristo Island) subject to the emission in 2017 of a mixture of gas, mainly methane, and mud well above the sea surface.

Due to the complexity of these types of events, an integrated study is necessary: acquiring data from different points of view (geological, morphological and chemical-physical) and video images is necessary in order to characterise the site being tested in an interdisciplinary way.

The coordinated action between the different entities took place with the goal of 3D mapping the area with the identification of targets of interest and of classifying the nature of the seabed, developing a rapid environmental characterisation procedure in case of exceptional events, environmental monitoring and risk management, also in support of Civil Protection.

The work was carried out by integrating the backscatter data with the analysis of the Water Column data obtained from a high resolution multibeam echosounder (MBES) mounted on the ITS Magnaghi (Italian Navy Ship) and with video inspections using the e-URoPe ROV, to identify and map any presence of gas leakage, and by sampling water and performing multi parametric vertical CTD profiles. The inclusion in the data acquisition procedures of inspections of the seabed by the ROV allows to obtain data characterised by reproducibility, accuracy and precise georeferencing, higher than those obtainable by human operators.

The Institute of Marine Engineering of the National Research Council took part in the data acquisition campaign using the autonomous vehicle e-URoPe (e-Underwater Robotic Pet).

6.2 Integrated seabed gas emissions observing system: the contribution of marine robotics

As previously discussed, robotics can provide effective solutions to collect high quality data in hazardous environment, mitigating risks and allowing the overcome of some limitations typical of traditional surveys. At the same time, however, it must be considered that autonomous operations in hazardous areas require ad-hoc projects and solutions: the specific application, characterised by certain environmental constraints and specific outputs to be obtained, is the driving factor towards the definition of the observation and monitoring procedures, and towards the development of innovative technological tools. The robotic platform e-URoPe of CNR-INM is an example of this process of technological innovation driven by environmental constraints.

e-URoPe is a hybrid ROV/AUV system (Figure 6.1), characterised by an open and reconfigurable structure: following the needs coming from the different types of mission and the actual indications arising from the environment, it is possible to easily change in e-URoPe the position of sensors and cameras, to add more payload, modify the frame and even change the propulsion layout. During this campaign, e-URoPe was used in the ROV configuration, with an umbilical cable, that can be deployed and retrieved through a portable and electrically actuated winch, for the power supply and the transmission of data and commands to and from the remote control station (Odetti et al., 2017).

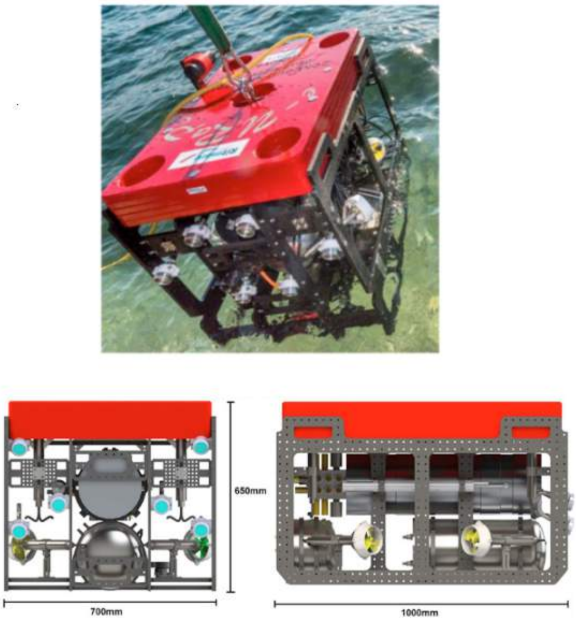

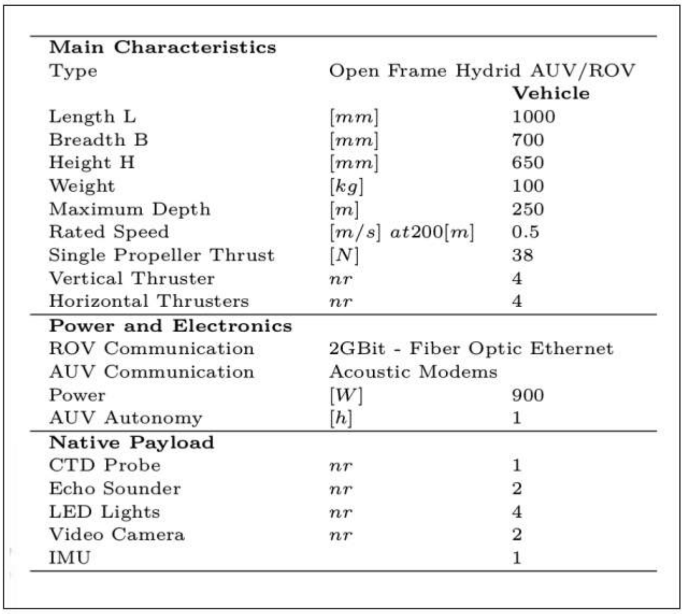

Main Characteristics		
Type	Open Frame Hydrid AUV/ROV	
		Vehicle
Length L	$[mm]$	1000
Breadth B	$[mm]$	700
Height H	$[mm]$	650
Weight	$[kg]$	100
Maximum Depth	$[m]$	250
Rated Speed	$[m/s]$ $at 200[m]$	0.5
Single Propeller Thrust	$[N]$	38
Vertical Thruster	nr	4
Horizontal Thrusters	nr	4
Power and Electronics		
ROV Communication	2GBit - Fiber Optic Ethernet	
AUV Communication	Acoustic Modems	
Power	$[W]$	900
AUV Autonomy	$[h]$	1
Native Payload		
CTD Probe	nr	1
Echo Sounder	nr	2
LED Lights	nr	4
Video Camera	nr	2
IMU		1

Figure 6.1 – e-URoPe (e-Underwater Robotic Pet) the hybrid ROV/AUV system of CNR-INM. On the left a picture and two rendering of the robotic platform are shown. On the right there is a table with the main characteristics of the robotic vehicle.

The basic instrumentation for the autonomous navigation of e-URoPe includes a system of attitude and orientation measurement (AHRS), a positioning system (GPS), a CTD probe (Electrical conductivity, Temperature and Depth), a Doppler effect velocimeter (DVL), a fiber optic gyroscope (FOG), a USBL transponder (Ultra Short BaseLine) for underwater acoustic positioning and two altimeters. Moreover, three analog cameras installed at the stern and bow offer the pilot a subjective panoramic view of the operating environment. In addition to the navigation instruments, instruments for the characterization of the seabed have been installed, in particular a single-beam sonar operating at 200 kHz and a vertically mounted Ethernet camera that allows you to acquire high resolution images of the area under the vehicle.

6.2.1 e-URoPe operations and acquisition procedures during the 2019 “Scoglio d’Affrica” campaign

The Hydrographic Institute, on the basis of bathy-morphological data and results of the analysis of the waters acquired in the campaigns of the previous years, proposed a survey area (Figure 6.2, left) divided into three sub-areas based on different priorities. As regards the activity with the ROV, this was concentrated in the area called “1a” in the Figure 6.2 (right), considered of particular interest for the degassing phenomena and in which the high resolution survey with the multibeam was also performed.

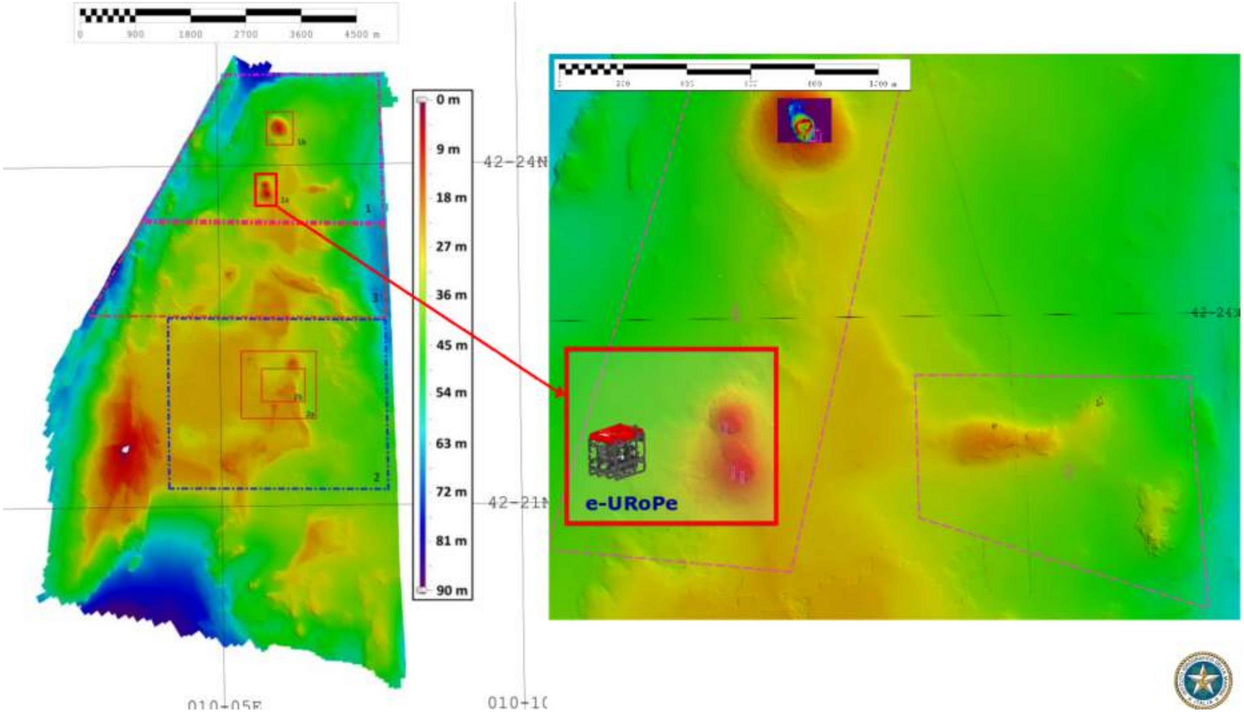

Figure 6.2 – Left: bathymetric chart (courtesy of Hydrographic Institute) of the survey area divided into sub-areas based on different priorities. Right: detail of the area investigated with the ROV, considered of particular interest for the degassing phenomena.

e-URoPe was embarked on the ITS Magnaghi (Italian Navy Ship) (Figure 6.3, left side) which is also equipped with two support boats (Figure 6.3, right side) that can be put in sea to carry out operations in areas with shallow water, where the ship would not be able to operate. This is the case of the area under investigation, characterised by very shallow waters, which reaches just 7 m in depth in some areas.

Figure 6.3 – Picture of the ITS Magnaghi (left); picture of one of the two support boats (right) available on the ITS Magnaghi.

During the data acquisition campaign, two different procedures to acquire data with the ROV were tested. The first involved the use of the ROV with its surface remote control station installed on the support boat. In order to operate in this mode and to have the precise position of the ROV during the underwater phases, an acoustic positioning system has been installed, consisting of a USBL transponder on the boat and an acoustic modem on the ROV (Figure 6.4).

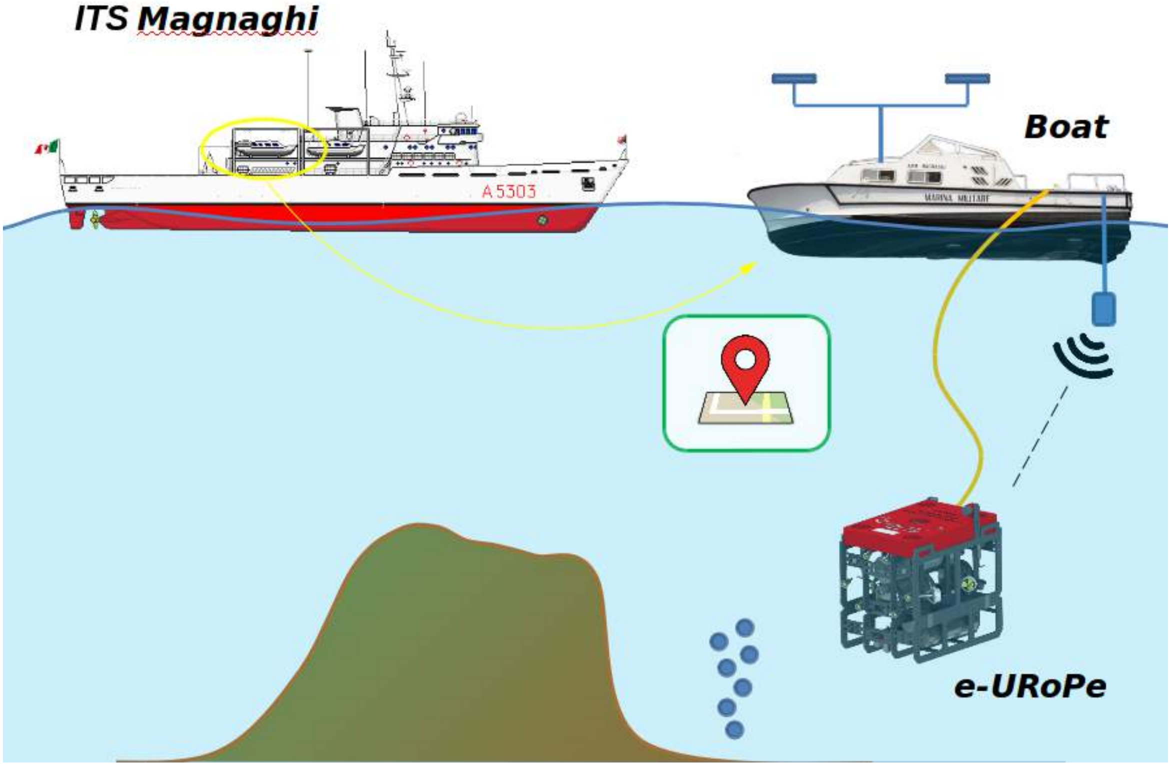

Figure 6.4 – Sketch of the first operating procedure: the ROV has the surface remote control station installed on the support boat. In order to have the precise position of the ROV during the underwater phases, an acoustic positioning system has been installed: the USBL transponder on the boat and the acoustic modem on the ROV.

The operations of putting to sea the boat, the ROV and the descent of the personnel on board the boat were successfully carried out. Since the boat was put in sea far from the operating site, a long transfer with the ROV towed was necessary. Once reached the operating site, the boat's power supply system stopped working and it was discovered that the boat is not able to support the power required for the operation of the ROV and of its instruments. Recovery operations were then carried out which included disconnecting the ROV cable from the surface remote control station, recovering the ROV, passing the ROV tether from the boat to the ship, getting the personnel on board the ship and recovering the ROV and the boat. From this first experience with ROV no scientific data were acquired but it was possible to learn some useful general indications on the operating procedures for the monitoring:

- the boat does not involve risks related to the possibility that the ROV cable ends up between the propellers (it has no propellers for movement);
- the cable can twist around the USBL pole, but the problem is manageable;

- the sea-holding capacity of the boat does not seem to allow operations that require continuous attention to a monitor, due to the roll.

With this lesson learned in mind, a second operating procedure was implemented which involved the use of the ROV with the surface remote control station installed on the ITS Magnaghi (Italian Navy Ship) (Figure 6.5).
Putting to sea the ROV directly from the ITS Magnaghi (Italian Navy Ship) presents "structural" problems related on the one hand to the characteristics of the ship itself, equipped with a single stern propeller and a bow thruster, and on the other to the specificity of the site of interest, a shoal that has a depth of 7-10 m in some points and which forces the ship to remain at a certain distance from the operating site.

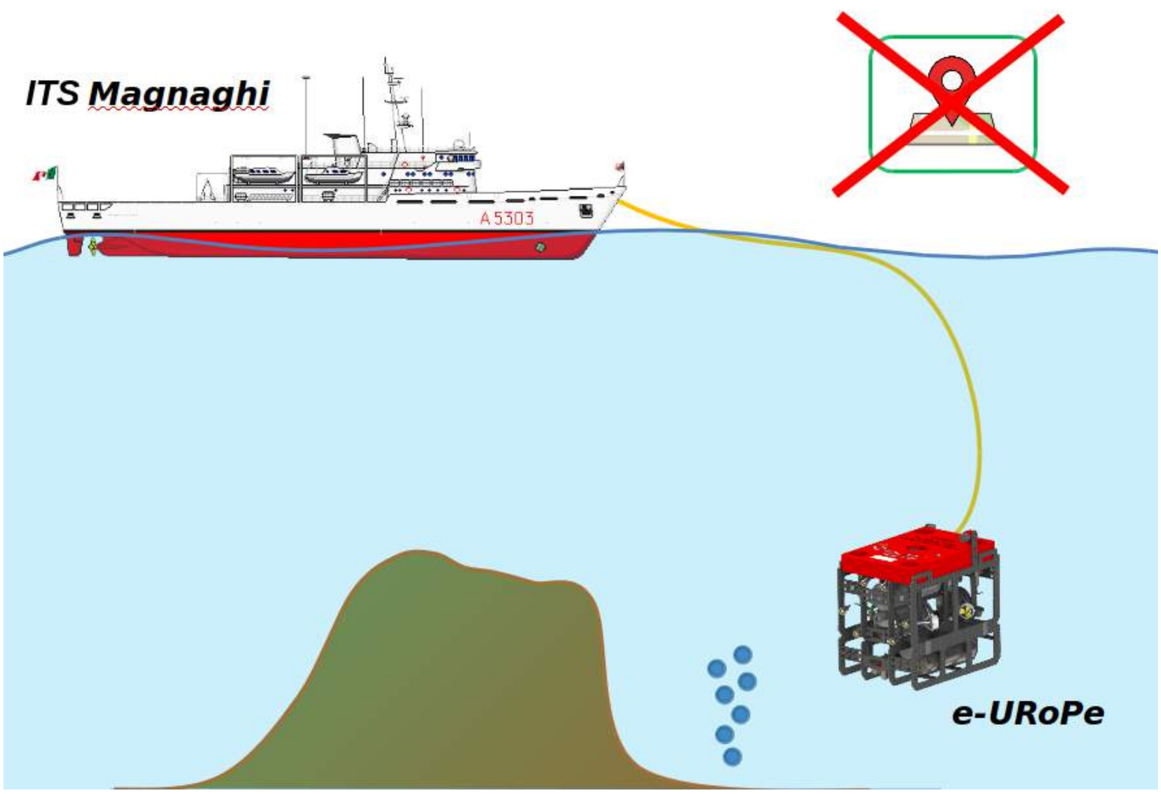

Figure 6.5 – Sketch of the second operating mode: the ROV was put into sea and operated directly from the ITS Magnaghi. In this case no underwater positioning system for the ROV is available.

For these reasons, the ROV was forced to work with a lot of cable at sea arranged approximately horizontally: in these conditions the cable exerts a considerable horizontal force on the ROV itself, limiting its maneuvering capabilities.
Moreover, due to the configuration of the ship, it was not possible to mount the USBL transponder on the ship and therefore the precise underwater location of the ROV with respect to the ship was not available during the immersive phases. In order to keep track of the position of the ROV and to minimize the risk associated with the possibility that the ROV cable could end up in the ship's

propeller, it was decided to work with a support rubber dinghy (Figure 6.6). The operators on board the dinghy maintained a mechanical connection with the ROV by means of a rope: this solution was also useful for supporting rapid movements between the different monitoring points executed with the dinghy towing the ROV.

Figure 6.6 – Pictures of e-URoPe during the launching phase from the ITS Magnaghi and of the support operations performed with the rubber dinghy.

After being lowered to the sea laterally, the ROV worked in the bow of the ship. The continuous work of launching and recovery of the ROV umbilical cable has highlighted the opportunity to motorize the winch to manage this kind of operations more easily.

At one point the cable hooked under the bow: it was noticed that, working with the vertical cable decoupled from the horizontal disturbance, the ROV maneuvered very well: it is necessary, for future campaigns, to adopt a logistics that allows the ROV to work with the cable vertically, an operating situation in line with the characteristics of this class of vehicles. This can be accomplished for example by using a ship with DP (Dynamic Positioning) or by coupling the ROV with an ASV (Autonomous Surface Vehicle) equipped with DP.

Having overcome some practical-logistical difficulties, the use of the ROV allowed the observation of different underwater site of interest for the gaseous emissions and demonstrated the possibility of carrying out long-term missions, considerably longer than those possible by means of human underwater operators. In addition, the exercise of carrying out operational activities with an ROV put into sea directly from a ship with the characteristics of the ITS Magnaghi (Italian Navy Ship) has allowed to acquire experience and indications for future operating procedures, even in case of emergency situations.

Several dives of varying duration each, from 20 minutes to more than 1 hour, were performed with the ROV. During the immersions, video images were recorded using three analog cameras mounted on board e-URoPe: two covered the part in front of the vehicle (with 2 different angles) and the third framed the rear of the vehicle. In addition, on board e-URoPe there was also an Ethernet camera mounted vertically under the vehicle to record the area of the seabed flown over by the robot. In this way it was possible to record the gaseous emissions and at the same time have an overview of the type of environment and seabed that surrounded the different emission points. This is useful in order to study the origin of these emissions and also possibly their effect on the morphology of the seabed over time.

In parallel to the activities with the ROV, a very high resolution multibeam echosounder (MBES) survey was carried out, also acquiring the water column data to search for possible gaseous emissions. Multi-parametric vertical profiles were performed to investigate possible changes in the physical properties of the water mass. Furthermore, water samples were acquired using a Niskin bottle and direct samplings of the bottom were performed using a Van Veen grab sampler for subsequent laboratory analysis.

The next chapter is dedicated to the description of the collected data, the analysis of the ROV data and the results obtained, showing how the use of robotic platform can help and add values to the classical methods of investigation, typically employed in the observation of gas emissions phenomena and in the classification of seabed characteristics.

Chapter 7

Seabed gas emissions in the Scoglio d'Affrica area: data collection and analysis

The event of March 2017, when a violent episode of gas emission from the seabed surrounding the Scoglio d’Affrica took place, drew the attention to the northern Tyrrhenian Sea, also for safety reasons. Although this kind of episodes may represent a danger for navigation, especially if they occur in areas with shallow waters, there is currently a lack of studies and knowledge of these phenomena and a growing need to identify and monitor their characteristics also to estimate their potential risks. For these reasons, several data collection campaigns took place in this area in the last few years.

This chapter will deal with the data collected during the 2019 campaign coordinated by the Italian Hydrographic Institute (IIM) with the National Institute of Geophysics and Volcanology (INGV), the INstitute of Marine engineering (INM - Genoa) of the CNR, the Universities of Ferrara (UniFe) and La Sapienza (Roma1), demonstrating the interest in this type of events that can also have consequences from the point of view of security and Civil Protection.

The focus will be on the observing activities and on the data acquired using the CNR-INM e-URoPe robotic platform, employed to integrate the data collected through traditional techniques using the ITS (Italian Navy Ship) Magnaghi (morpho-acoustic data collection) and using divers (gas and seabed sampling for geochemistry analysis) with video images.

7.1 Morpho-acoustic data

The area to be inspected by the ROV was chosen based on the morpho-acoustic data of the previous campaigns carried out by the Italian Hydrographic Institute in the same area of interest.

During the 2019 campaign, new morpho-acoustic data acquisitions were made using a multibeam echosounder (MBES) Kongsberg EM2040 working at 300kHz, mounted on board the support boat supplied to the ITS Magnaghi (Italian Navy Ship). Figure 7.1 shows a high resolution bathymetric map obtained from the raw data collected with the MBES, integrated and corrected using sound velocities profiles data and processed using CARIS Hips&Sips to obtain the Digital Elevation Model (DEM) of the area.

This specific area is part of an elongated main NNW-SSE ridge that rises 30 m from the surrounding seabed, already observed in the high-resolution bathymetric data collected subsequently to the 2017 gas outburst. The ridge is made up of two mounds (Figure 7.1, 1a red square; Figure 7.2) whose tops are located at about 8 m and 10 m water depths, respectively (Casalbore et al., 2020).

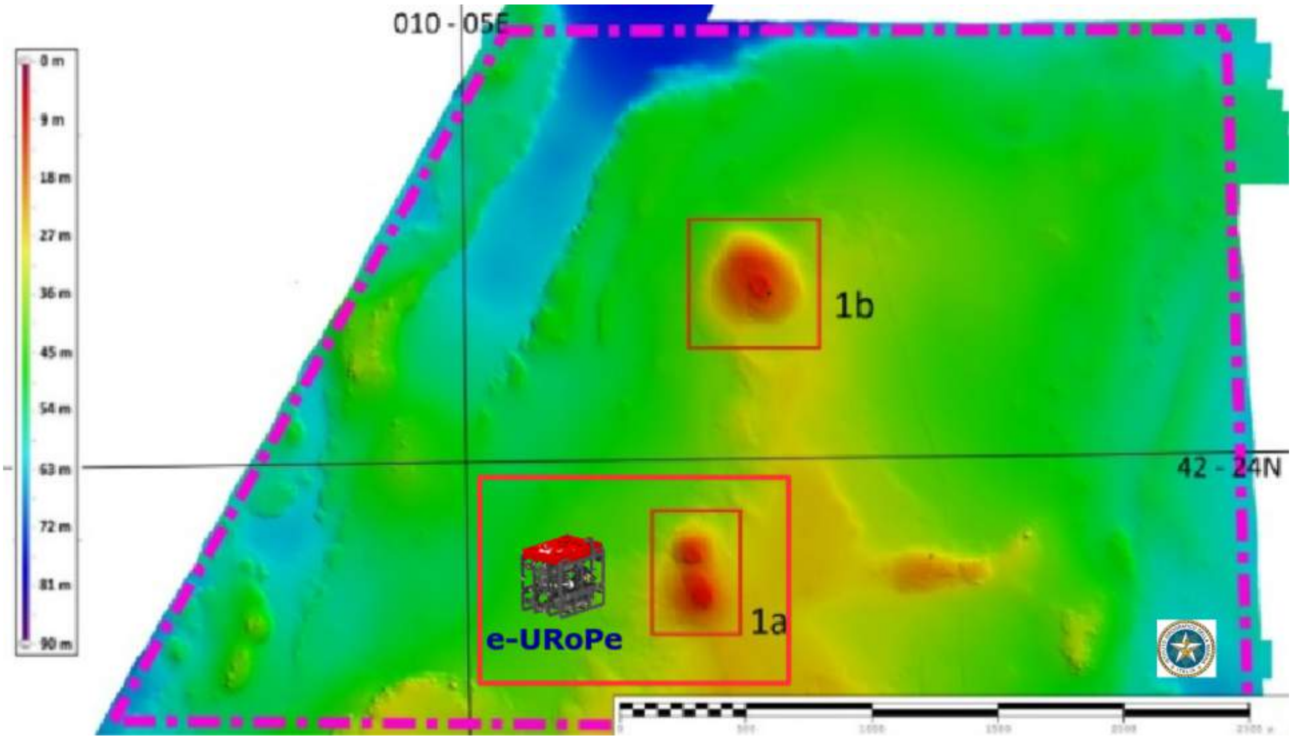

Figure 7.1 - Morpho-bathymetric map of the area investigated during the 2019 campaign (courtesy of Italian Hydrographic Institute). The e-URoPe ROV was used to make observations in the sub-area named "1a" (lower red square).

The different dives carried out with the e-URoPe ROV, described below, were concentrated in the sub-area named "1a" (Figure 7.1, lower red square) characterised by the two mounds that were still present three years after the violent gas emission event in 2017, despite the shallow depth of the area that could, in some way, modify the structure of the seabed through the wave motion.

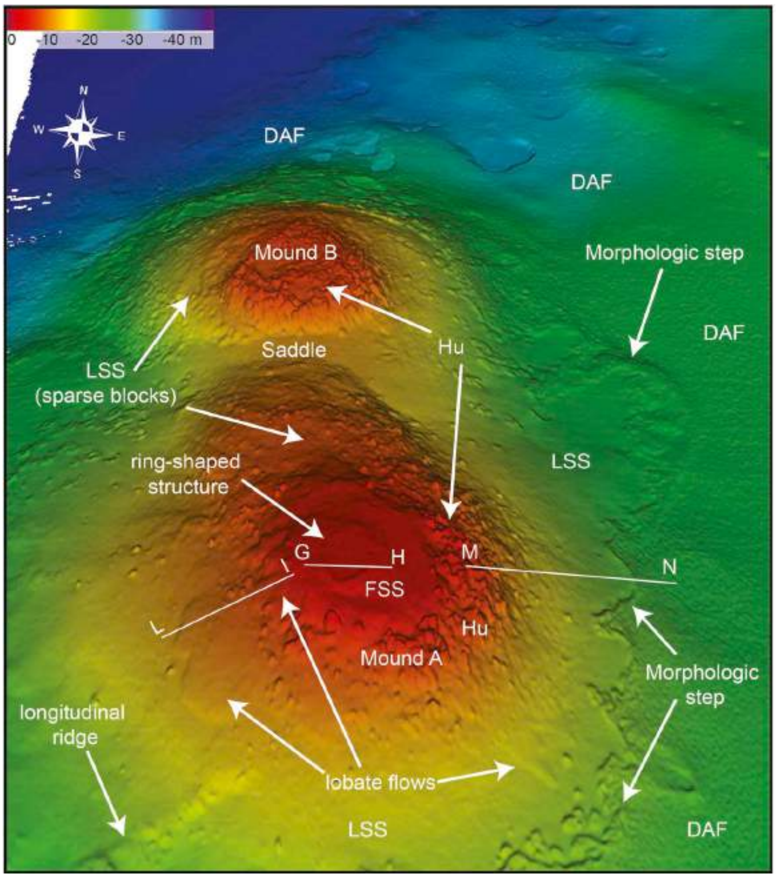

Figure 7.2 - 3D view of mounds A and B, with the indication of the main morphologies and morpho-acoustic facies: FSS: Flat and Smooth Summit, Hu: Hummocky morphology, LSS: Lower and Smooth Slope (divided in two sub-facies according to the density of the blocks), DAF: dimpled acoustic facies (Casalbore et al., 2020).

7.2 e-URoPe dives and video data acquisition

The e-URoPe robotic vehicle was developed to be adapted to specific requirements in terms of variables to be measured and environmental constraints associated with the measurements. To carry out underwater navigation and observation of the gaseous emissions and the surrounding environment, the vehicle was equipped with the following instruments:

- a system of attitude and orientation measurement (AHRS) to provide estimation of an object orientation in space (Microstrain 3DM-GX3-35);
- a positioning system (GPS) available during the surface operations, integrated in the Microstrain 3DM-GX3-35;
- a CTD probe (Electrical conductivity, Temperature and Depth) for the physical characterisation of the environment (OCEAN SEVEN 305Plus multi-parameter);
- a Doppler effect velocimeter (DVL - ExplorerDVL TELEDYNE) that measures motion underwater: how fast the vehicle is moving and in what direction;
- a fiber optic gyroscope (FOG) for heading measurements (QUADRANS iXBlue);
- two altimeters (Tritech Micron echosounder) and a single-beam sonar (Echologger ECS400, operating at 200 kHz) for bathymetric data;

- three analog cameras installed at the stern and bow;
- a vertically mounted Ethernet camera (Bullet Network Camera VIVOTEK IB8168) that allows to acquire high resolution images of the area under the vehicle.

As described in the previous chapter, due to operational constraints, the USBL transponder (Ultra Short BaseLine) for underwater acoustic positioning could not be employed.
In the Table 7.1 there is a summary of the instruments installed and operational during the ROV data acquisition.

Table 7.1 - Instruments installed on-board e-URoPe and operational during the ROV data acquisition

Date	Time	Where	Vehicle	Instruments									
				AHRS	GPS	(C)TD No C data	DVL	FOG	USBL	Altimeter	3 Analog Cameras (Pilot view, Video)	Singlebeam Echosounder	1 Ethernet Camera (down-looking, video/images)
08/06/19	7:19-8:15	Area 1a	e-URoPe	v	v	v	v	v	x	v	v	v	v
08/06/19	8:34-9:47	Area 1a	e-URoPe	v	v	v	x	v	x	v	v	v	v
08/06/19	10:14-10:46	Area 1a	e-URoPe	v	v	v	v	v	x	v	v	v	v
08/06/19	10:53-11:01	Area 1a	e-URoPe	v	v	v	x	v	x	v	v	x	x
08/06/19	11:23-11:43	Area 1a	e-URoPe	v	v	v	v	v	x	v	v	x	v

During the data acquisition phases, the robotic vehicle performed five dives in as many points of interest as possible for the study of gaseous emissions. Between one observation point and another, the vehicle was towed by a support rubber dinghy, to speed up transfer operations and maximize data acquisition time. The graph in the figure 7.3 shows the time on the x-axis (in the format hour: minutes: seconds) and on the y-axis shows the depth value of the vehicle with respect to the water surface as measured by the depth sensor of the CTD. Observing this graph it is possible to see the different immersion phases of the ROV, as highlighted by the horizontal red arrows.
The overall operations with the ROV lasted about five hours and a half, during which dives of different duration were made: from the shortest, lasting about twenty minutes, to the longest, lasting more than an hour. Note: Dive three and four are considered a single dive as they took place in the same point of interest. There was no transfer between the two dives but only the ROV which rose to the surface and then re-submerged.

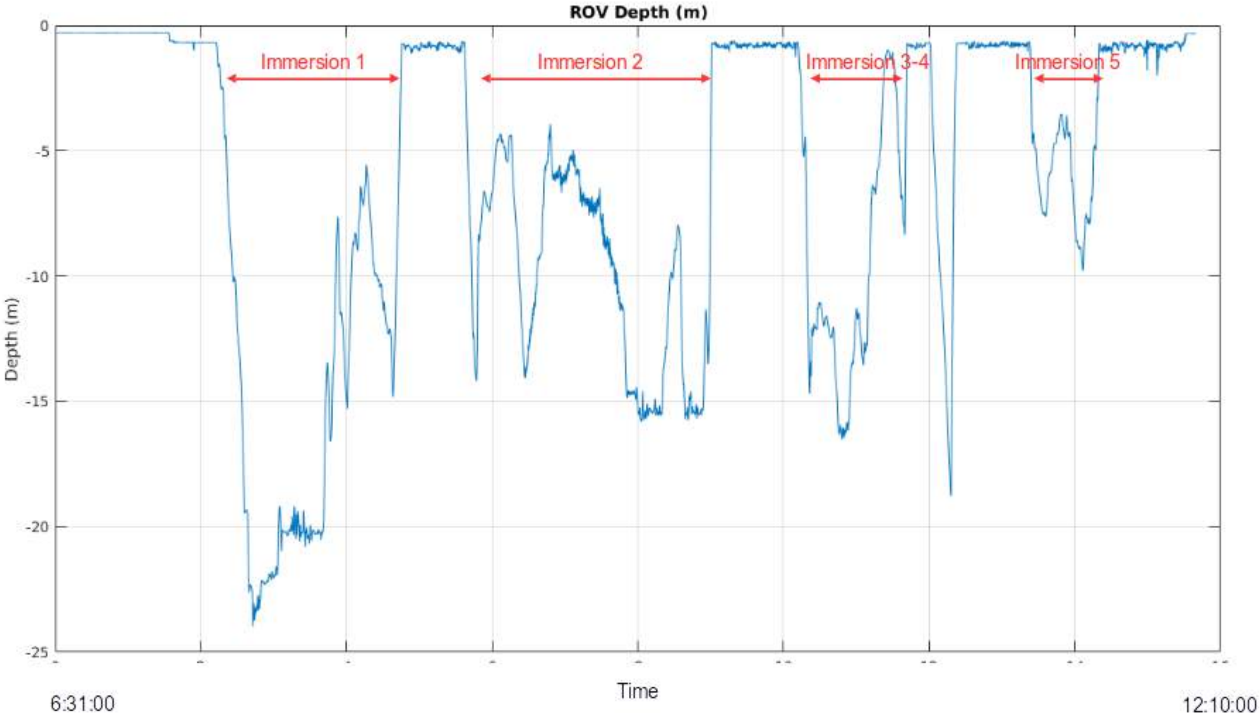

Figure 7.3 – Graph showing the five dives performed by e-URoPe (horizontal red arrows). The x-axis shows the time (in the format hour: minutes: seconds) and the y-axis shows the depth value of the vehicle with respect to the water surface as measured by the depth sensor of the CTD.

7.2.1 Time synchronisation of the data

Since the robotic platform worked in ROV mode, i.e. with an umbilical cable connecting the vehicle itself to the remote control station, it was possible to have the live streaming of the video images and then use the visual feedback of the cameras to direct the vehicle towards possible areas of interest for gaseous emissions. At the same time, both the video from the analog cameras using a DVR (digital video recorder) and the vehicle telemetry data from the sensors and instruments were recorded. In this way, however, two separate devices were used for data recording, resulting in an imperfect synchronization of the time scales: the videos had a time-stamp in “hour:minute:second” format based on the clock of the DVR while the telemetry data had a time-stamp originating internally from the clock of the operating system of e-URoPe.

The first work on the data, therefore, was to synchronize the times between the various data available. To do this, the videos were observed and the time at which the dive began and the time of the subsequent surfacing were marked. Once these times were known, the depth of the vehicle was graphed as a function of the vehicle’s internal time-stamp. In this way it was possible to pair the vehicle’s time corresponding to the beginning of the descent with the dive time in the format “hour:minute:second” of the DVR and so on for each immersion and emersion phase. The result of this synchronisation work is the graph shown in the figure 7.3 and also in the table 7.2. This table summarizes the five dives, detailing the times obtained with the synchronisation. It also reports some additional telemetry data (which in turn were synchronized) and which will be used in the other data analysis phases, described below.

Table 7.2 – Table that summarizes the times and GPS points of diving and surfacing of e-URoPe. Other data obtained from the vehicle's telemetry are also reported, useful in the subsequent analysis phases.

Time	Lat	Lon	Depth	Heading	Operation
07:19:00 AM	42.39514	10.09151	1.211	50.23	Immersion 1
08:15:00 AM	42.39567	10.09175	0.729	71.06	Emersion1
08:34:00 AM	42.39541	10.09263	1.637	3.38	Immersion 2
09:47:00 AM	42.39581	10.092	0.736	96.61	Emersion 2
10:14:00 AM	42.39668	10.09176	1.572	49.96	Immersion 3
10:46:00 AM	42.39715	10.09078	0.704	74.65	Emersion 3
10:53:00 AM	42.39767	10.08863	1.931	106.97	Immersion 4
11:01:00 AM	42.39775	10.08892	0.731	137.16	Emersion 4
11:23:00 AM	42.39682	10.09254	1.925	81.93	Immersion 5
11:43:00 AM	42.39707	10.09192	0.759	20.36	Emersion 5

7.2.2 Data analysis and emissions points identification

Once the video times were synchronized with the vehicle telemetry times, the data analysis involves the identification of the gaseous emissions from the seabed in order to create a map.

At this point, the question of underwater positioning of the vehicle arises. The GPS, in fact, during the diving phases does not function and continues to send out the last position left in memory before diving. From the GPS data recorded it is therefore possible to obtain the positions of the diving and surfacing points but not the path followed by the ROV while underwater.

Due to the lack of an underwater positioning system, the ROV track was inferred from the GPS data available while on the surface, integrated with the data from the DVL, that measures how fast the vehicle is moving and in what direction, and with the heading data from the FOG.

Applying algorithms of dead reckoning on these data, it was possible to reconstruct the hypothetical route followed by the vehicle during the diving phases.

The vehicle’s positions obtained were subsequently integrated with video and MBES data, allowing the different seafloor features observed in the videos to be associated with the distinct morphologies acoustically identified on the mounds: in this way the correctness of the results obtained is verified. The figure 7.4 shows the morpho-bathymetric map of the area, obtained from the MBES data, on which the trajectories traveled by e-URoPe are superimposed.

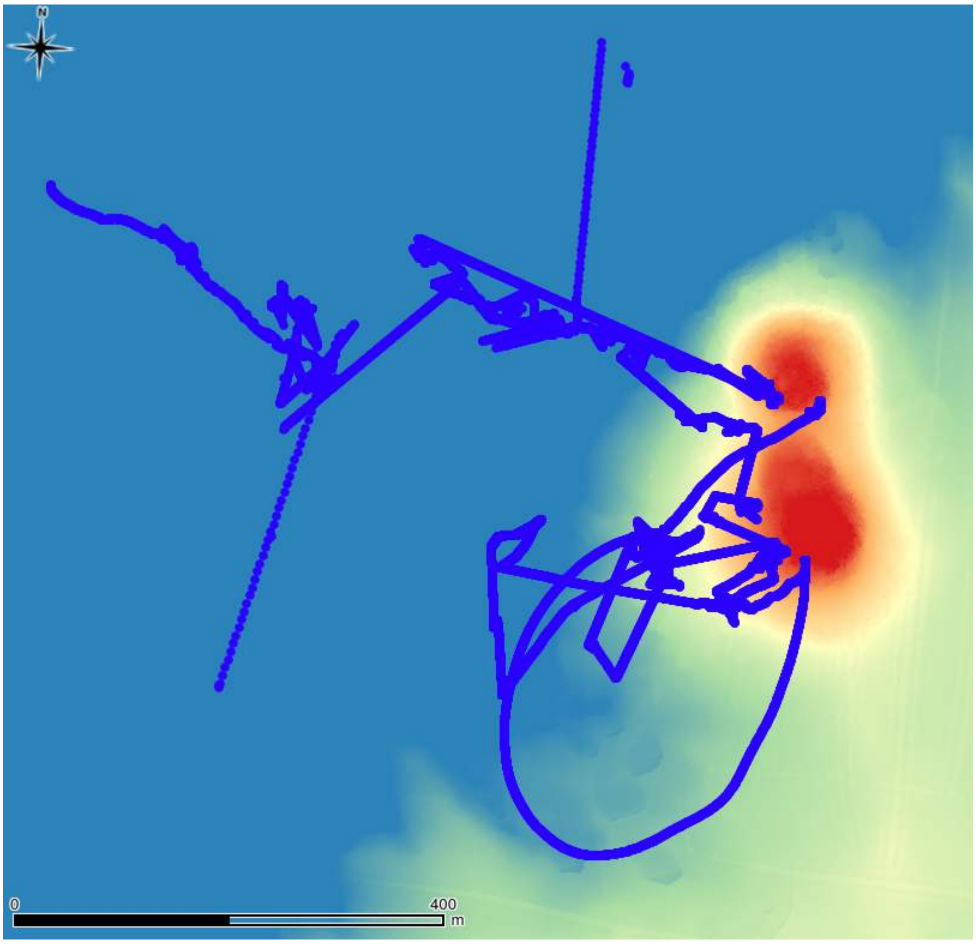

Figure 7.4 – Morpho-bathymetric map of the area of investigation, obtained from the MBES data (courtesy of Italian Hydrographic Institute), on which the trajectories traveled by e-URoPe are superimposed (blue line).

Integrating data from different sources (video images, telemetry of the robotic platform and acoustic MBES data) it is possible to identify different types of seabed and observe whether there are associated gaseous emissions or not. Some examples of observed data and phenomena are reported in the following paragraph.

During the first dive, highlighted in red in the graph at the top of figure 7.5, an area characterised by Posidonia oceanica meadows was flown over by the ROV. The area is also highlighted in the lower box in figure 7.5 and the estimated route traveled by e-URoPe is shown in yellow. In this area, where the seabed is covered with Posidonia oceanica, no gaseous emissions were observed during the test phase. The area characterised by the presence of Posidonia oceanica is located on the west side of the mound A, where the depth progressively increases with the distance from it.

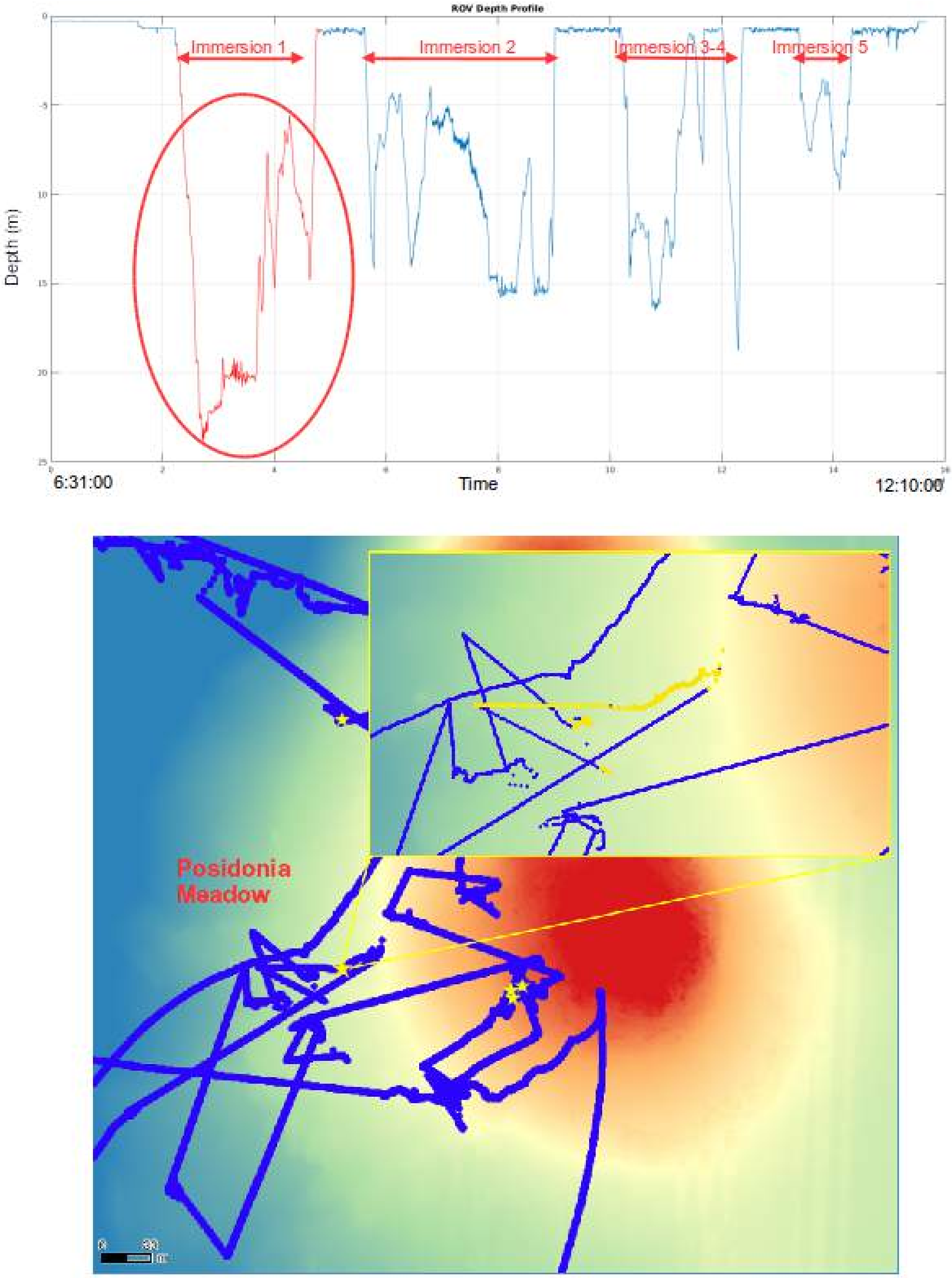

Figure 7.5 - Top: graph showing the five dives performed by e-URoPe. The first dive is highlighted in red. Bottom: the area characterised by Posidonia oceanica meadows and flown over by the ROV is located with a yellow star. The area is also highlighted in the box, where the estimated route traveled by e-URoPe is shown in yellow.

The following images in figure 7.6 show some areas characterised by the presence of Posidonia oceanica, acquired through the cameras mounted on board e-URoPe. The presence of Posidonia meadows in this area was already documented in various works, dating back to the 1960s (Del Bono et al., 1968).

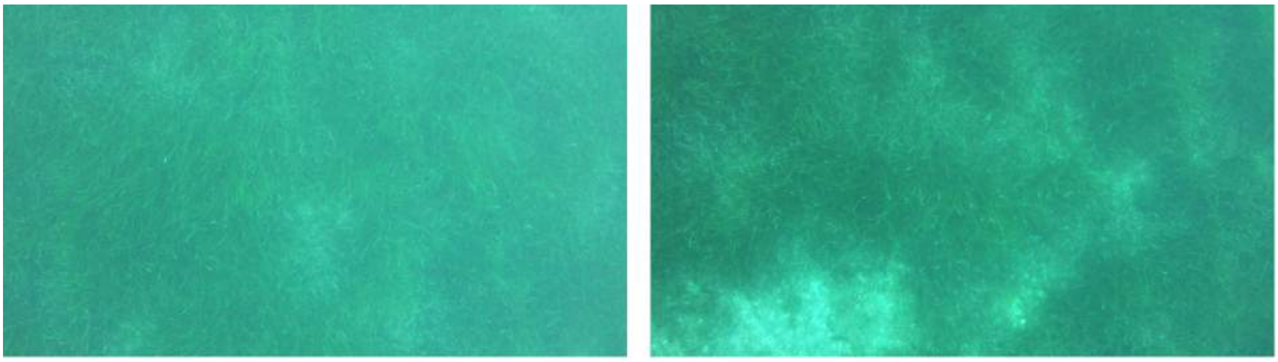

Figure 7.6 – Posidonia oceanica meadow observed on the west side of mound A.

Once the vehicle emerged, it was towed into the second area of interest, which is southwest (S-W) of mound A, as shown in the lower part of figure 7.7.

A long immersion was made in this area (lasting more than an hour, as can be seen from the graph in the upper part of figure 7.7), during which numerous active emission points were observed together with holes in the seabed identified as emission points not active during the investigation with the ROV (figure 7.8, a).

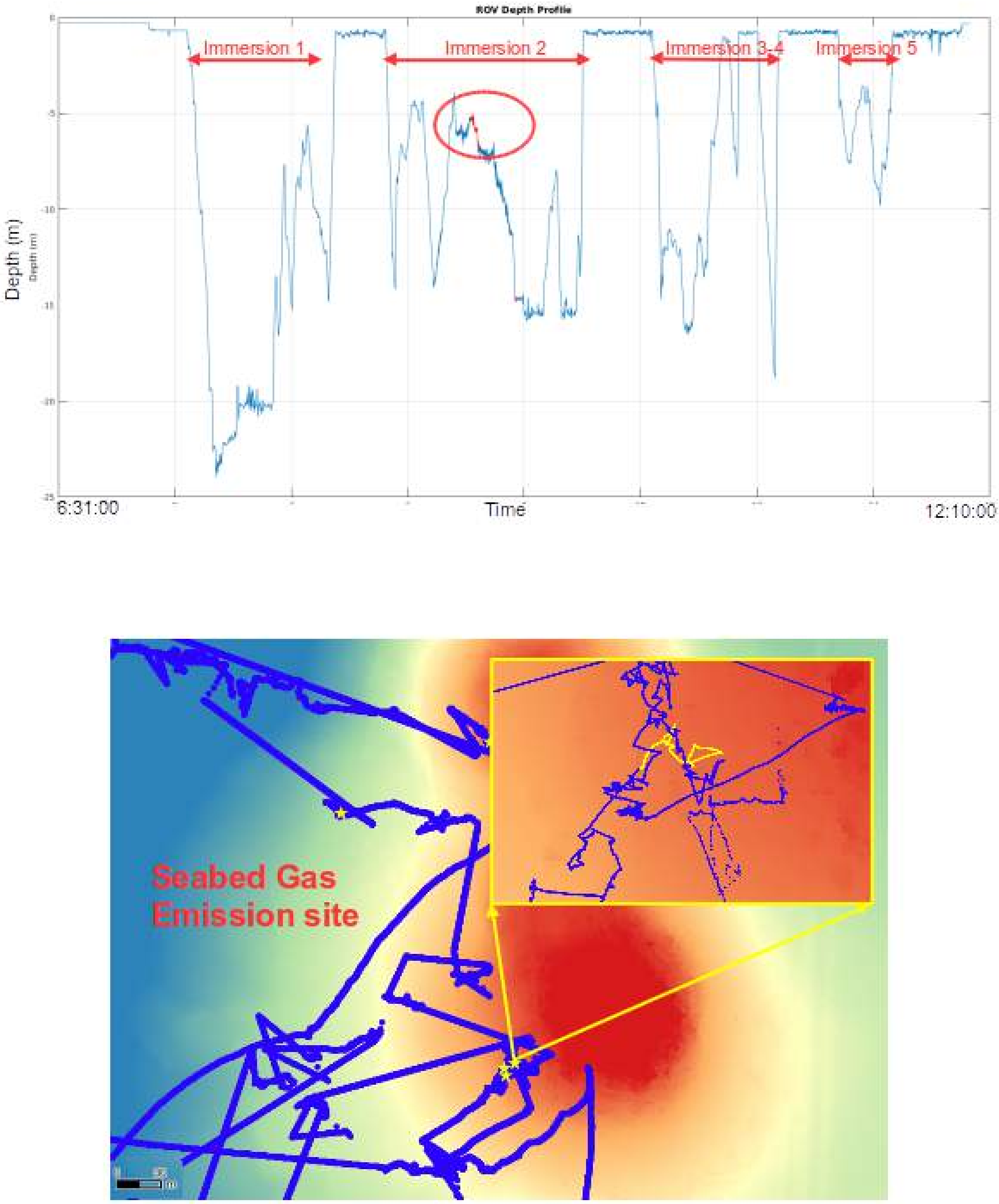

Figure 7.7 - Top: graph showing the five dives performed by e-URoPe. The subsection of the second dive analysed is highlighted in red. Bottom: the area characterised by degassing events and flown over by the ROV is located with yellow stars. The area is also highlighted in the box, where the estimated route traveled by e-URoPe is shown in yellow.

In this area, the seabed varies from areas whose bottom is covered with sand on which large blocks and masses (up to metric sizes) are scattered, to completely rocky areas. These rocks are often covered with algae, indicating that their presence dates back many years, even before the 2017 event. The pictures in figure 7.8 show several examples of seabed encountered during the second dive.

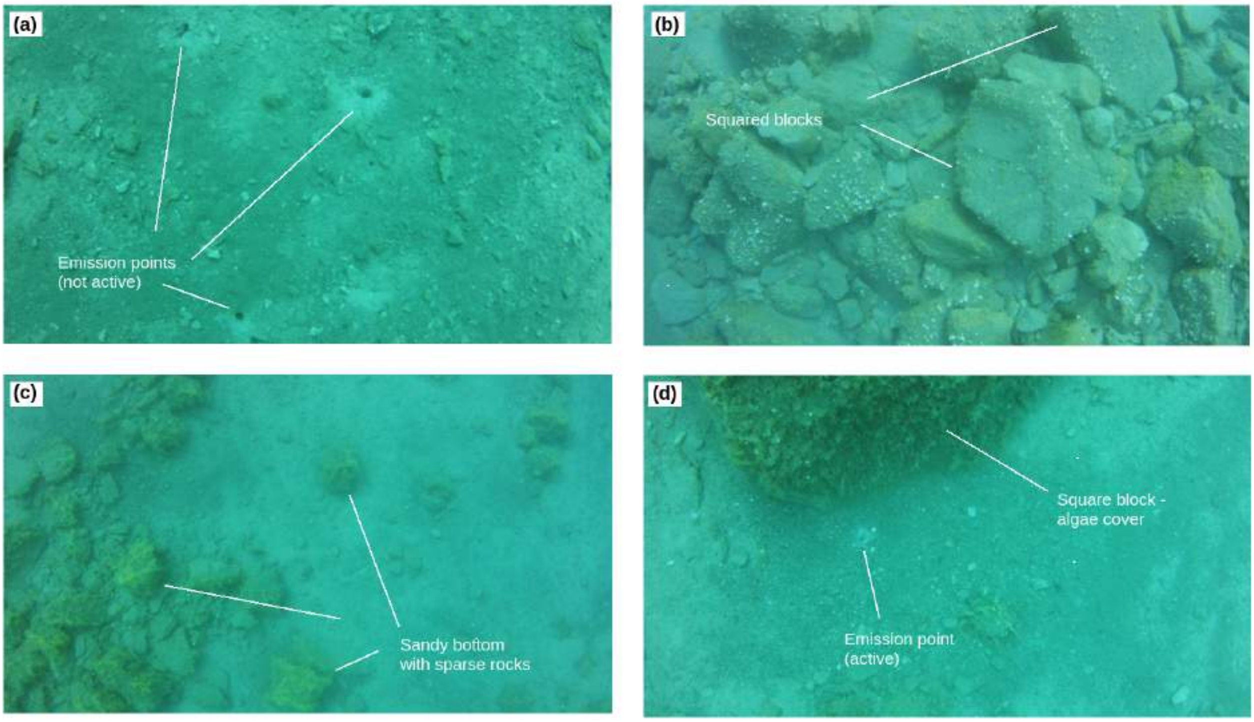

Figure 7.8 - Examples of seabed encountered during the second dive: a) sandy seabed with emissions points not active; b) rocky seabed; c) bottom covered with sand on which large blocks and masses (up to metric sizes) are scattered; d) large block covered with algae and near it an active emission point.

From the images collected, it was noted that the gaseous emissions very often occur at the contact points between rocks and sand. In particular, a persistent gaseous emission activity was observed in the area indicated in the figure 7.8-d: near the rock covered with algae, in the sandy bottom, there was a point from which gas leaks in the form of centimeter-sized bubbles were observed. The emission event was intermittent but constant throughout the observation time (a few tens of minutes) and the gas come out of small chimney of centimetric dimension.

Once re-emerged, e-URoPe was transferred to the area where it made the dives indicated as three and four in the upper graph of figure 7.9.

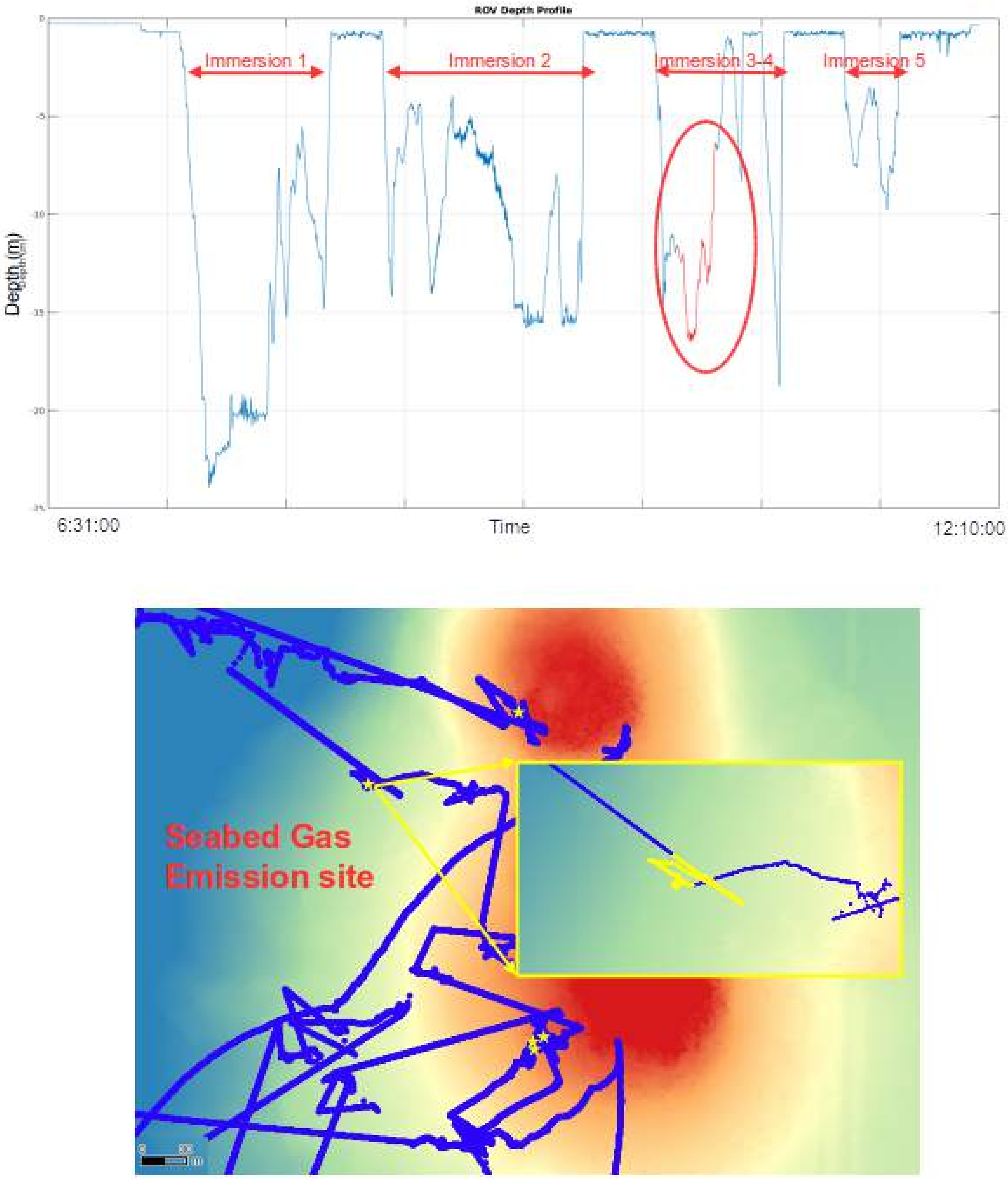

Figure 7.9 - Top: graph showing the five dives performed by e-URoPe. The subsection of the third and fourth dives analysed is highlighted in red. Bottom: the area characterised by degassing events and flown over by the ROV is located with a yellow star. The area is also highlighted in the box, where the estimated route traveled by e-URoPe is shown in yellow.

Analysing the video material acquired during these dives, it was found of particular interest for the purposes of mapping the gaseous emissions, the data taken in the time interval between about 10:20 a.m. and 10:30 a.m. (ten minutes). The map in the figure 7.9 highlights the interesting area with a yellow star and the box contains a zoom of e-URoPe route. This is a route reconstructed from the vehicle's telemetry data as during the dive phase, the GPS positions are not available.

Moreover, thanks to the data synchronisation work described previously, it was possible to associate the data obtained from the altimeter and depth gauge mounted on board the robotic vehicle with the video acquired.

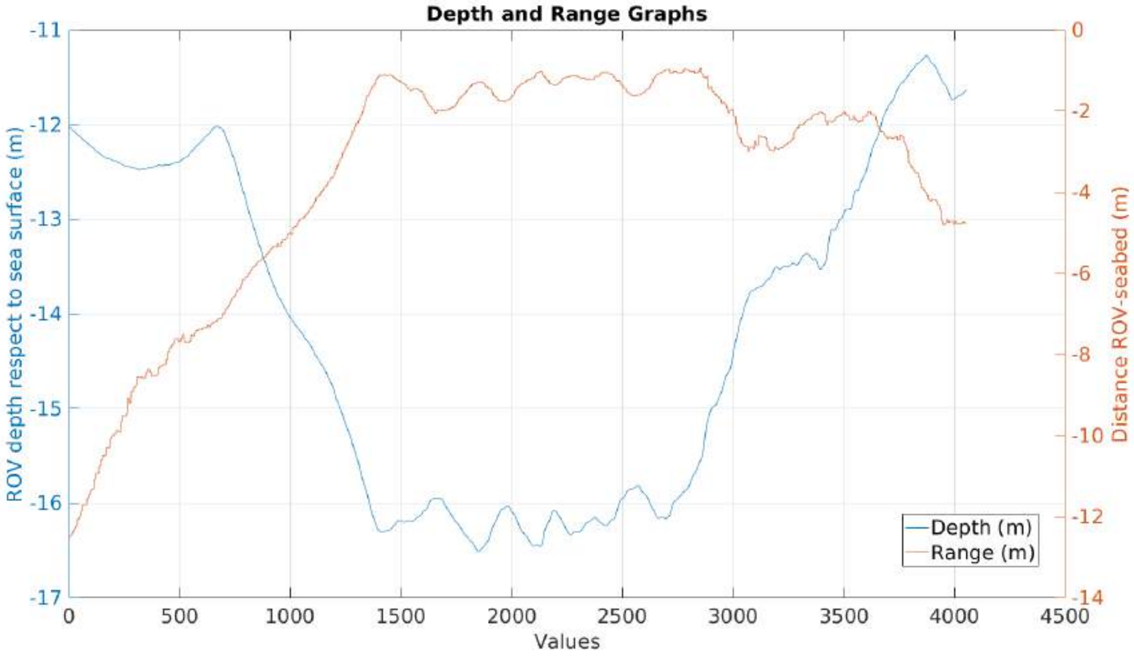

Figure 7.10 - Graph showing in blue the depth of e-URoPe with respect to the water surface, recorded by the depth gauge of the CTD, and in orange the distance of the vehicle from the seabed, measured by e-URoPe altimeter.

The graph in the figure 7.10 represents in blue the depth of the vehicle with respect to the water surface, recorded by the depth gauge of the CTD. The data in orange, on the other hand, represent the distance of the vehicle from the seabed measured by e-URoPe altimeter. From the graph it is possible to observe the initial immersion phase, characterised by an increase in depth with respect to the surface of the water and a corresponding decrease in the distance of the vehicle from the bottom (note the negative scale on the abscissas).

By adding these two sets of data available, it is possible to obtain the bathymetric data of the seabed (its morphology with respect to the surface of the water). The following graph (Figure 7.11), therefore, shows the depth values of the seabed, obtained from the sum of the pairs of previous values: in this way the profile of the seabed overflown by the robotic vehicle is obtained using a depth gauge and an altimeter.

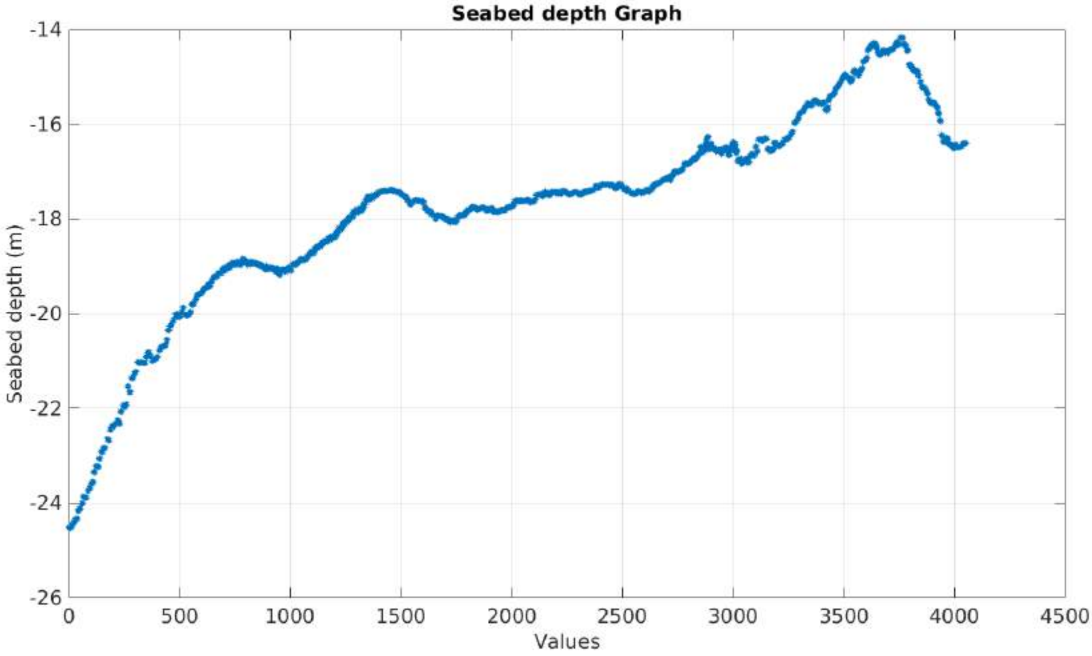

Figure 7.11 – Graph of the depth values of the seabed, obtained using the depth gauge and the altimeter mounted on-board e-URoPe.

The graph shows a decreasing trend in depth (negative y-axis scale). By putting together the data of the reconstructed route with the calculated depths, it is possible to obtain an indication of the bathymetry of the seabed in the area investigated with the ROV, as shown in figure 7.12.

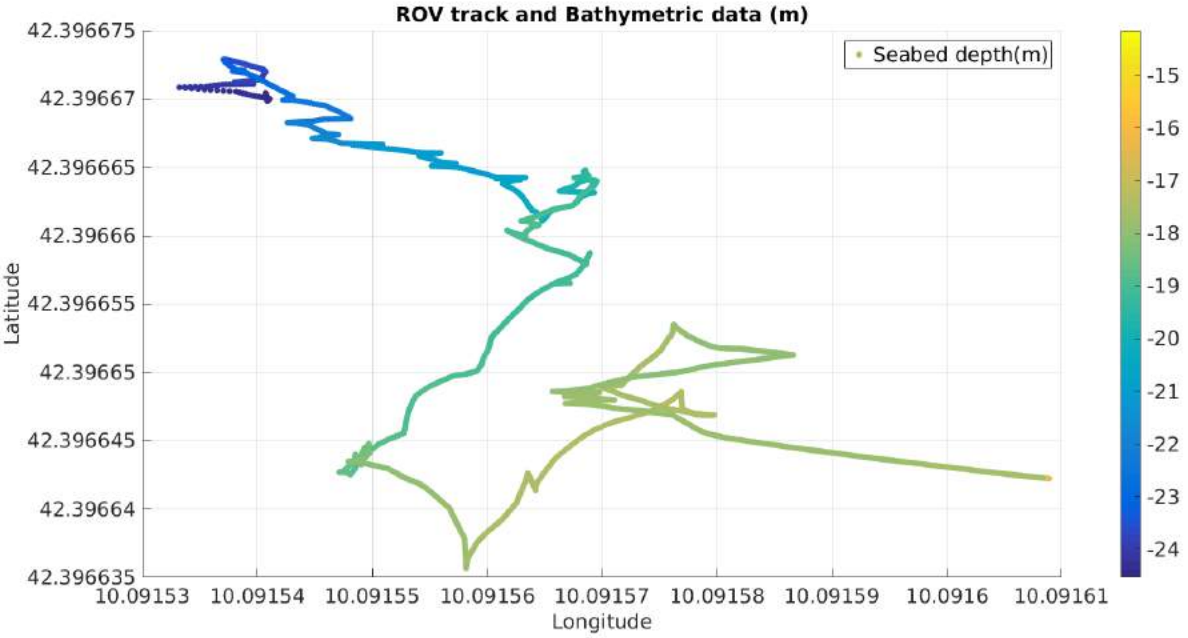

Figure 7.12 – Graph showing e-URoPe reconstructed route (Longitude values on the x-axis, Latitude values on the y-axis). The color scale is proportional to the seabed depth (m) obtained using the depth gauge and the altimeter of the ROV.

This graph agrees with the graph obtained from the acoustic data of the MBES, shown in the lower part of figure 7.9. In fact, it is noted that the ROV in its movement makes an approach path to the mound and that the seabed has a decreasing depth trend.

This exercise of estimating the bathymetry of the seabed starting from data collected with sensors commonly available as basic equipment of the ROV (altimeter and depth gauge) and the comparison of the results with the high resolution data obtained with more sophisticated (and expensive) instrumentation, such as the MBES, is done to demonstrate that in critical or emergency situations it is possible to intervene in a short time with a robotic vehicle, even if not equipped as necessary, but it is still possible to obtain data that are fundamental to characterise the environmental situation of the operations. With these kinds of procedures, the precisions and accuracies can be limited but the data is available in a short time. This is a fundamental aspect, for example, for REA (Rapid Environment Assessment) systems, which aim to have a first knowledge of the environment through data that are easy to interpret and characterised by the immediacy of information, in order to set-up an intervention strategy (Demarte et al., 2017). The videos registered are obviously part of these kind of data since they allow to observe the gaseous emissions and at the same time to characterise the surrounding environment.

During this dive it was noticed that the area in which there were the gaseous emissions phenomena was an area with a sandy bottom, of transition between the Posidonia oceanica meadow (which appeared in the images recorded by the rear camera of the ROV, figure 7.13, lower picture) and the area closer to the mound, characterised by mud breccia and the presence of rocks, as shown by the front cameras of the ROV, visible in the figure 7.13, in the two upper pictures. In these pictures are also visible examples of gas emissions.

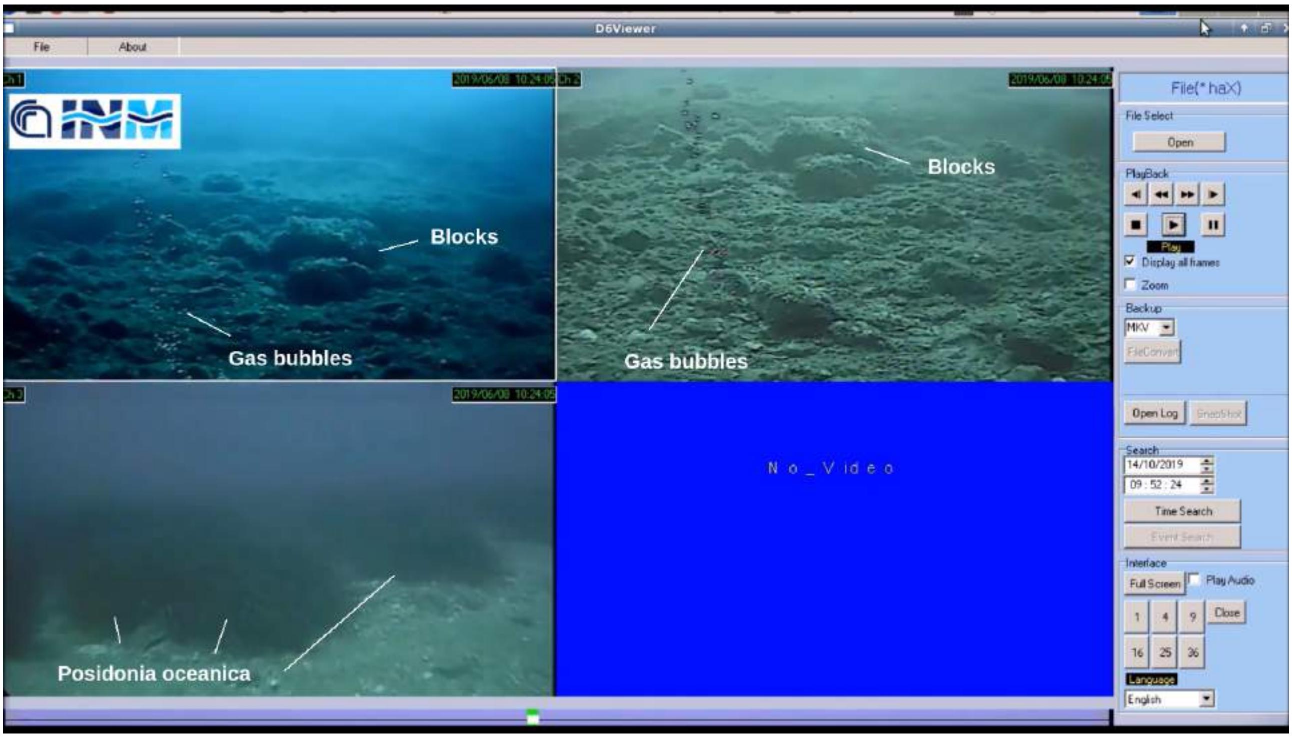

☑ Display all frames
☐ Zoom
Backup MKV
Search 14/10/2019 09 : 52 : 24
☐ Play Audio
Language English

Figure 7.13 – Images recorded with the analog camera mounted on-board e-URoPe: in the top part the two front cameras are shown while at the bottom there is the rear camera. Gaseous emissions are visible.

Once re-emerged, the ROV was towed towards the mound B, to the North of the previous one, where it made the last dive of the day (immersion 5, top of figure 7.14).
In this case, the autonomous vehicle has inspected the mound plateau area, as shown in the lower graph of figure 7.14. Also in this area, emissions activity was observed but of low intensity.

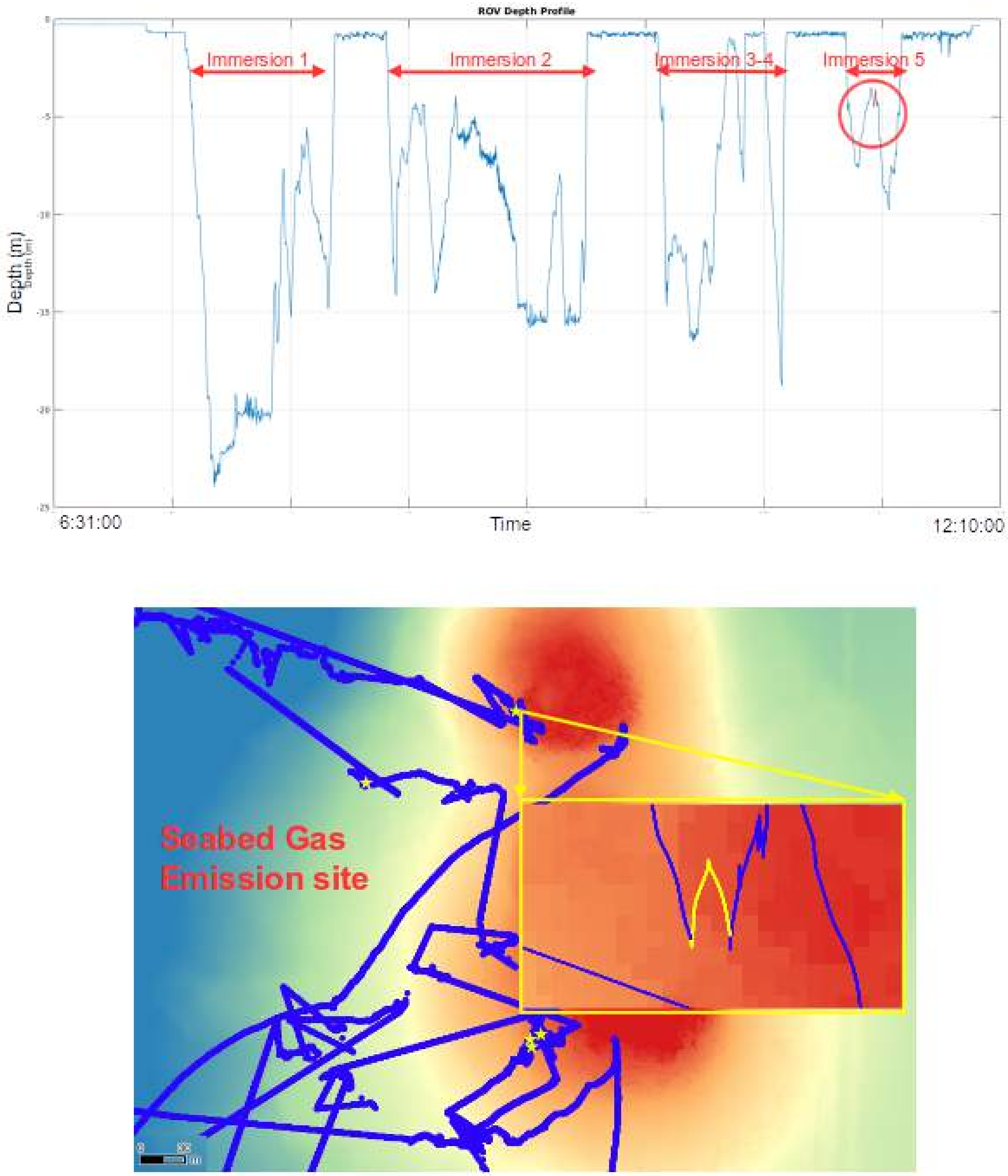

Figure 7.14 - Top: graph showing the five dives performed by e-URoPe. The short subsection of the fifth dive analysed is highlighted in red. Bottom: the area characterised by degassing events and flown over by the ROV is located with a yellow star. The area is also highlighted in the box, where the estimated route traveled by e-URoPe is shown in yellow.

The area is characterised by a central part, almost circular, with a sandy bottom. Ripples drawn on the sand by the wave motion are clearly visible. There, in fact, the depth is very limited and the morphology of the seabed is affected by the wave motion.

The sandy area is surrounded by the presence of both square and irregularly shaped blocks and masses, even of considerable size, covered with algae. These blocks create a sort of delimitation of the area of very shallow water. Going beyond them, the ROV flown over the slope of the mound which goes down towards areas with gradually higher depths. In the figure 7.15 on the left it can be seen the beginning of the mound slope and on the right an example of a sandy bottom with ripple.

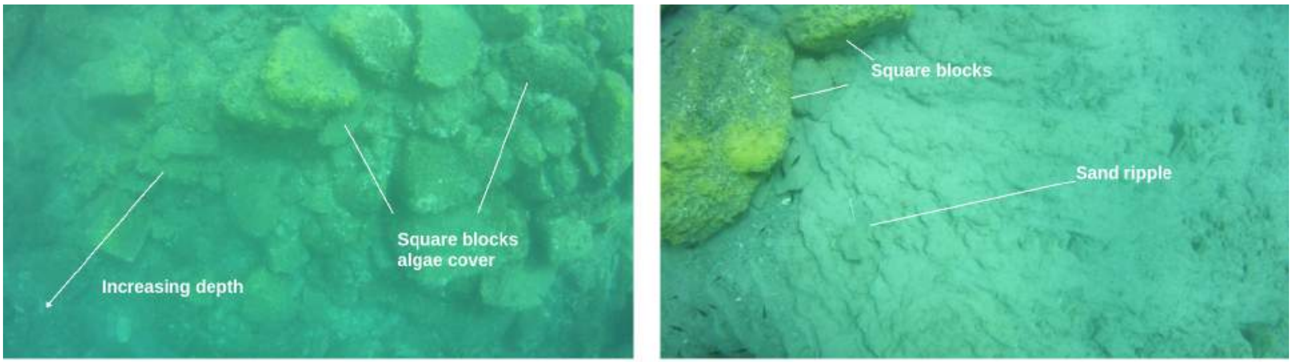

Figure 7.15 – Images acquired during the ROV dive on the mound B. On the left: the beginning of the mound slope is highlighted with an arrow; on the right: an example of a sandy bottom with ripple is shown.

The figure 7.16 shows a snapshot of the images acquired by the ROV during the overflight of the mound: the front cameras (upper two pictures) show the rocky area that delimits the mound plateau while the rear camera (lower picture) shows part of the sandy central area. The gaseous emissions in this area were observed in the contact area between the sandy bottom and the rocks.

☑ Display all frames
☐ Zoom
Backup: MKV
Search: 15/10/2019 09:13:03
☐ Play Audio
Language: English

Figure 7.16 - Snapshot of the images acquired by the ROV during the overflight of the mound. The front cameras (upper two pictures) show the rocky area that delimits the mound plateau; the rear camera (lower picture) shows part of the sandy central area.

7.3 Rapid environmental assessment: map of gas emissions points

Due to the complexity of degassing events from the seabed, an integrated study that acquires data from different points of view (geological, morphological and chemical-physical) and video images, is necessary in order to characterise the site in an interdisciplinary way.

The reconstructed underwater vehicle's positions, integrated with video and MBES data, allow the different seafloor features observed in the videos to be associated with the distinct morphologies acoustically identified on the seabed. In this way, the videos were georeferenced and a preliminary map of gas emission points was created.

The following figures (7.17 and 7.18) show a bathymetric map of the area, with the isobath lines indicating the depth of the seabed corresponding to the different colors: red is about -10 m, yellow about -20 m and so on toward deeper seabed in the light blue area (-40 m). The reconstructed routes of the ROV are drawn with a blue line and the identified degassing points are highlighted with yellow stars (and circles, figure 7.17).

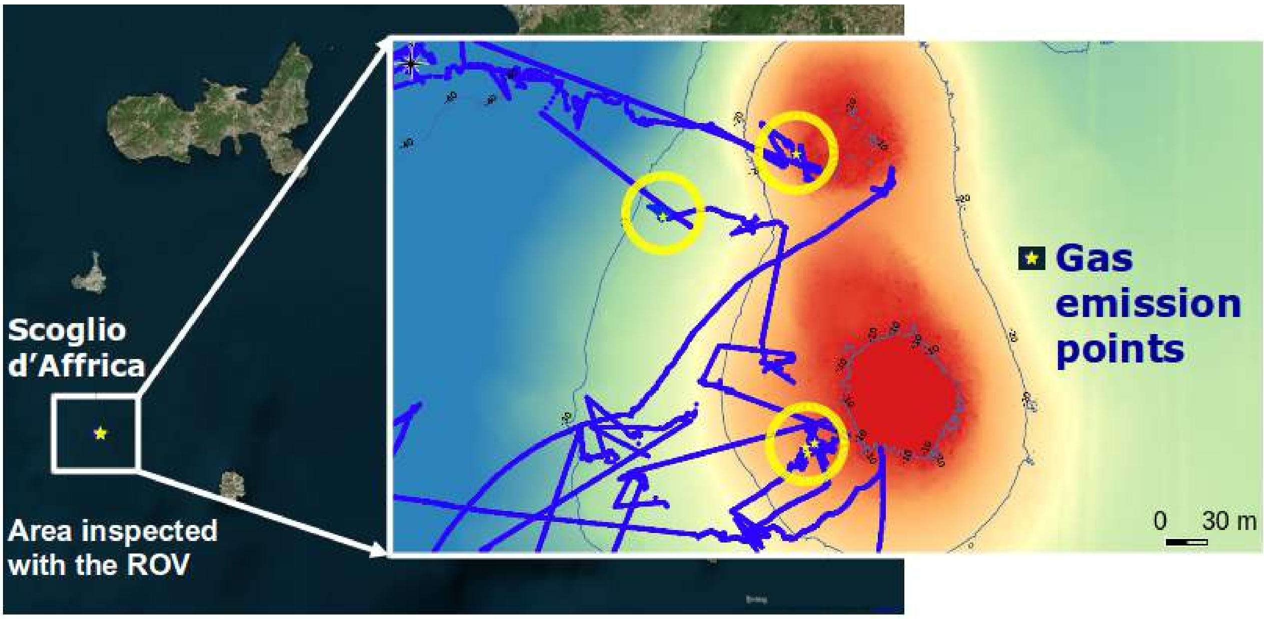

Figure 7.17 – Map of the area under investigation. The image in the box shows the bathymetric map of the area with the isobath lines indicating the depth of the seabed corresponding to the different colors: red is about -10 m, yellow about -20 m and the light blue about -40 m. The blue line shows the reconstructed routes of the ROV and the identified degassing points are highlighted with yellow stars and circles.

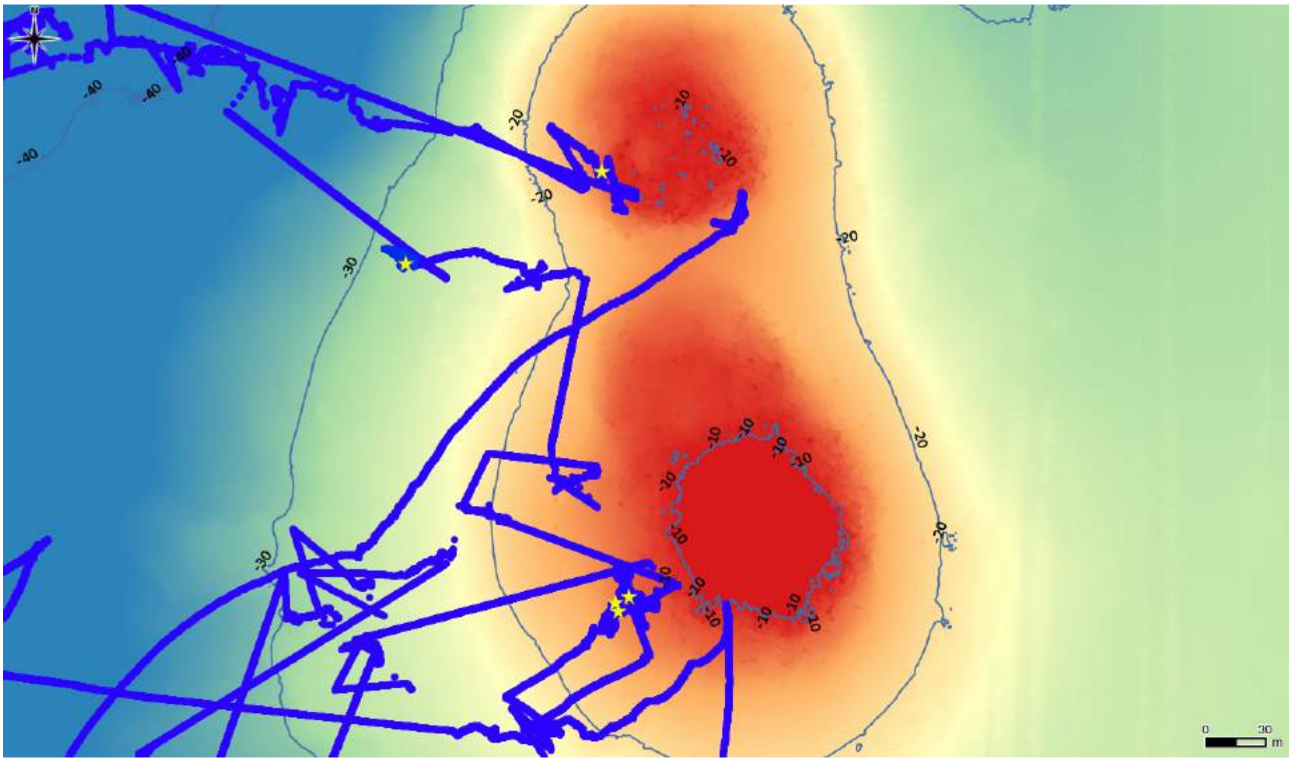

Figure 7.18 – Detailed bathymetric map of the area under investigation. For the description of color scale and symbols, refer to Figure 7.17.

The video collected by the ROV show wide-spread active seepages characterised by both continuous and intermittent bubble release from the seafloor, with several venting points distributed over different seafloor types. In general, the degassing activity is weak with small bubble columns that are emitted punctually and come out of small chimney of centimetric dimensions. The type of emission depends on both the porosity of the bottom and the amount of gas in the substrate.

Moreover, by putting together the data of the reconstructed ROV's routes with the seafloor depths calculated from data collected using sensors commonly available as basic equipment of the ROV (altimeter and depth gauge), it is also possible to obtain an indication of the bathymetry of the seabed in the area investigated with the ROV. With these kinds of procedures, the precisions and accuracies can be limited but the data is available in a short time. This is a fundamental aspect for systems which aim to have a first knowledge of the environment, in order to eventually plan an intervention strategy, especially in risky situations (Demarte et al., 2017).

The coordinated action between the different entities (IIM, INGV, INM–Genoa, UniFe and Roma1) took place with the goal of 3D mapping the area, identify the targets of interest and classify the nature of the seabed, developing a rapid environmental characterisation procedure in case of exceptional events, environmental monitoring and risk management. During the same campaign, CTD acquisitions along the water column and sampling of gas and sediment from the seabed were also carried out by human operators. As described in Saroni et al. (2020), the geochemical analysis of the gas samples allows to classify the gaseous emissions of the area of the Scoglio d'Affrica as typical of mud volcanoes. These seeps have a gas composition of biotic origin, with methane as the prevalent component (95 vol%) and minor gases which include carbon dioxide, nitrogen and trace amounts of helium. The combined stable C and H isotope composition of CH_4 ($\delta^{13}C$ and $\delta^{2}H$) and the enrichment in heavy carbon isotopes of CO_2, highlight a prevalent secondary microbial origin for these fluids. The classification as a mud volcano is also confirmed considering the morphology as well as the sedimentary and petrographic characteristics of the solid materials together with the geochemistry of the fluids expelled from the Scoglio d'Affrica site (Saroni et al., 2020).

Summarising, the observing and monitoring activities carried out in complex and critical environments like the one described above, underline that two main aspects are fundamental:

- the choice of the instruments and sensors to be mounted on the robotic platforms which must be able to guarantee certain performances (in time and space) and at the same time must be able to operate even in demanding conditions and with power requirements that are sustainable;
- the implementation of sampling procedures that are flexible and that can be adapted according to the specific working environment and the measure to be obtained.

The preliminary results described above are very important because show that, even in situations far from the "ideal operating conditions", it is still possible to obtain indicators that can be interpreted as hazard precursors for the implementation of alarm procedures.

Chapter 8

Discussion of transient phenomena observations in Svalbard and Northern Tyrrhenian Sea

The particularity of this work consists in adapting observing methodologies, based on robotic platforms, according to the marine environment being studied in order to obtain results that are reliable, reproducible and comparable with those obtained through the classic monitoring methodologies. The environments in which the tests were executed are particularly dynamic, sensitive and fragile areas where it is necessary to study and apply particular methodologies to observe phenomena strongly localised in space and requiring very high resolutions in time. The critical conditions may present some risks not only for the data acquisition but also for the instrumentation and the operators. Furthermore, these conditions also constitute a limit from a metrological point of view: very often it is not possible to perform repeated measurements due to adverse conditions and therefore measurements referring to the observations of different phenomena are associated even if they are not directly comparable from a metrological point of view. In this context, it is essential to apply multidisciplinary and coordinated measurement procedures to gather data that have metrological traceability thus ensuring compatibility (Ferretti et al., 2020).

8.1. Oceanographic processes from tidewater glacier in Kongsfjorden

In the previous chapters natural phenomena were examined which, at a first and quick glance, appear very distant and different. The first case study concerns the description of the Arctic environment in all its complexity and fragility, which includes specific processes allowing us to have a look at the current state of our environment and at its future evolution. In order to give better estimates of the future changes within a relatively short time, regions with a large natural climate gradient, and where processes sensitive to the expected changes are particularly important should be studied (Lindbäck et al., 2018; Van den Heuvel et al., 2020). Svalbard and the surrounding ocean areas fulfill all these criteria: they are located in a region with a very large climate gradient, being alternately influenced by cold central Arctic or mild marine climate conditions at time scales of weeks to years (Cottier et al., 2005; SIOS, 2019; Tverberg et al., 2019). The processes that take place in this area should be studied considering the climatic and meteorological, geological and geomorphological as well as oceanographic and sedimentological framework in which they are inserted. All these factors are fundamental to understand the processes taking place there. This environment, so important for its richness of phenomena, is however still characterised by a lack of data due to the numerous logistic difficulties in collecting them, increased by the severity of climatic and environmental conditions, typical of Polar areas. The need to take a step forward compared to the methods traditionally used in order to contribute to fill the gap of data that still persists, leads to the employment of the autonomous vehicle PROTEUS, specially developed by CNR-INM for applications in Arctic areas (Bruzzone et al., 2020; Odetti et al., 2017): this vehicle is characterised by versatility and adaptability, therefore it can be suitably modified according to the environmental constraints in which it operates. Furthermore, the critical environment is also an incentive for the development of "data driven" acquisition procedures: the final goal in terms of space-time resolution of the data leads to the development of precise procedures for their acquisition. This thesis describes the data acquisition operations carried out in the Kongsfjorden highlighting how the use of a robotic surface platform with the ability to perform profiles along the water column using a bunch of sensors (CTD, turbidimeter, ArLoC sensor) allowed to obtain data unique for their characteristics of accuracy, resolution and precision, making it possible to study the physical and bio-optical properties of the water masses of the fjord in general and of the areas close to the tidal glacier front in particular, and thus capture particular processes of stratification of the waters inside the fjord that occur in these areas difficult or impossible to reach and observe. The uniqueness of the results obtained compared to those known in the literature is also related to the ability to discriminate water masses of different nature, connected with the circulation phenomena inside the fjord and with the processes occurring at the limit of the ice glacier fronts, with unprecedented level of detail. The choice of the specific variables to monitor derives by the indications developed by international communities working on the definition of variables that are considered fundamental to characterize the climate system and its changes. In this work we focus on specific parameters that are listed in the Essential Climate Variables (ECV) defined by the Global Climate Observing System (GCOS) and in particular in some of the Essential Ocean Variables (EOV) defined by the Global Ocean Observing System (GOOS). Salinity and temperature of seawater measured with depth, turbidity and concentration of chlorophyll-a pigment in the water are variables also defined as “Core Data” in the SIOS integrated observing system for the Svalbard area. Moreover, the connection with the essential variable schemes can provide guidelines and criteria for the definition of requirements for temporal and spatial coverage for the different variables, that can also depend on the specific scientific question to be answered (SIOS, 2019).

The sampling of these specific water parameters is inserted in a more general context regarding the study of water masses and their dynamics. This is a particularly complex subject that must consider various factors on different time scales. For what concerns the Svalbard area, there are instant components (ice-collapsing and calving events), seasonal and annual components (influence of water coming from ocean currents, seasonal temperature variations, wind, etc.), and also components on much longer time scales (pluri-annual, decennial and even secular) that can be studied by analysing also the morphology of the seabed and the sediments at the water-bottom interface.

In this work, the data collected allow us to concentrate on a very short time scale within which instantaneous and strongly localized in space phenomena occur but with consequences on the ecosystem of the fjord that also extend over longer time scales. These phenomena are related to the introduction of melt water from the tidewater glaciers present in the Kongsfjorden and to the formation of plumes which, once they reach the surface of the water, spread mixing with the water of the fjord. Through the analysis of these specific variables, it is possible to identify the distribution of the water mass and the presence, in some points, of the plume of meltwater coming from the glacier, before the mixing with the water of the fjord.

In addition to the water component due to the melting of the glacier, in the late spring period during which the tests were carried out (beginning of June 2018), there is also a component of water that originates outside the study area but which, due to the global dynamics of the ocean circulation, is pushed into the fjord itself. The two main water masses originating outside the study areas are the Atlantic Water (AW) element of the West Spitsbergen Current (WSC) and Arctic Water (ArW) of the coastal current (Table 8.1). Both these currents flow northwards along the west Spitsbergen margin, steered by the slope edge topography (Figure 8.1) (Bensi et al., 2019; Howe et al., 2019).

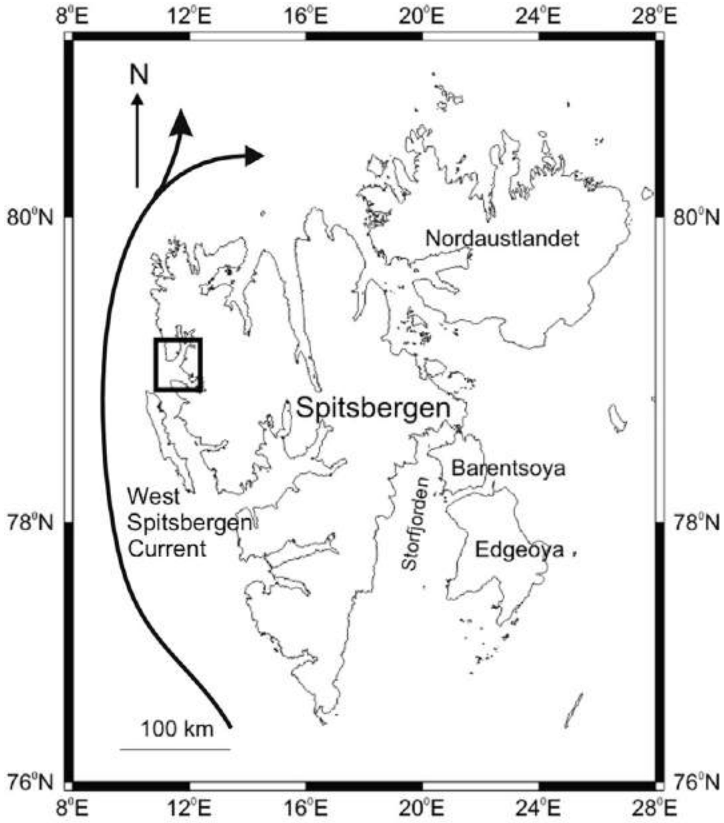

Figure 8.1 – Svalbard map showing the position of the Kongsfjorden (black square). The arrows indicate the approximate trajectory of the West Spitsbergen Current (WSC) which strongly influences the marine environment of the fjord through the advection of warm Atlantic Water (Howe et al., 2019).

Recent years have been characterised by an increase in the temperature and frequency of warm AW incursions into west Spitsbergen fjords, alongside an increase in the temperature of the WSC (Cottier et al., 2005). Due to the dynamic nature of cross-shelf transport, there is an annual cycle where water of Arctic origin dominates through winter and Atlantic water dominates through summer (Cottier et al., 2005; Svendsen et al., 2002). However, models do suggest that more heat is transported into the inner fjord during summer, resulting in a larger potential for glacier front melt (Sundfjord et al., 2017). A recent study of the Kronebreen-Kongsvegen glacier (Meslard et al., 2018) suggests that the high concentration of suspended sediment discharged in a surface water plume, is the result of a subglacial river. The presence of these focused, concentrated discharges of sediment-rich meltwater can strongly influence the ecosystem of the fjord, with subsequent consequences for the benthos and biogeochemistry of the system (Howe et al., 2019).

In addition to the aforementioned waters of external origin, it is possible to classify different types of water originating inside the fjord; one of these is the Surface Water (SW), which derives from the dissolution of cryospheric components (snow, ice and melting of glaciers). The thickness of this surface layer is generally greater in the inner parts of the fjords and then decreases towards the mouth of the fjord. The water in this layer has a very wide range of salinities and temperatures, as shown in table 8.1 (Howe et al., 2019).

The Transformed Atlantic Water (TAW), is a water of Atlantic origin created by the mixture of AW and ArW and can be found in the deeper parts of the fjords. When TAW enters the fjords, it undergoes further transformation due to entrainment and mixing with SW giving rise to Intermediate Water (IW) (Cottier et al., 2007). During autumn and winter, lower air temperatures and stronger winds will decrease the temperature giving rise to what has been termed Local Water (LW) in the Svalbard fjords. Once the LW has reached freezing point, which is typically in November or December, continuous surface cooling will lead to sea ice formation and associated brine release. This more saline winter water is called Winter-Cooled Water (WCW) (Nilsen et al., 2016; Svendsen et al., 2002). The following table comparatively summarizes the classification of water masses found in literature. In particular, the values are obtained from Cottier et al. (2005) and from Howe et al. (2019). The values shown in blue in the brackets are obtained from Tverberg et al. (2019), adapted from Svendsen et al. (2002).

Table 8.1 – Comparative table of temperature (°C) and Salinity (PSU) values used in literature for the classification of the water masses found in the Kongsfjorden and on the adjacent shelf. The values are derived from Cottier et al. (2005) and from Howe et al. (2019). The blue values in brackets are obtained from Tverberg et al. (2019) adapted from Svendsen et al. (2002).

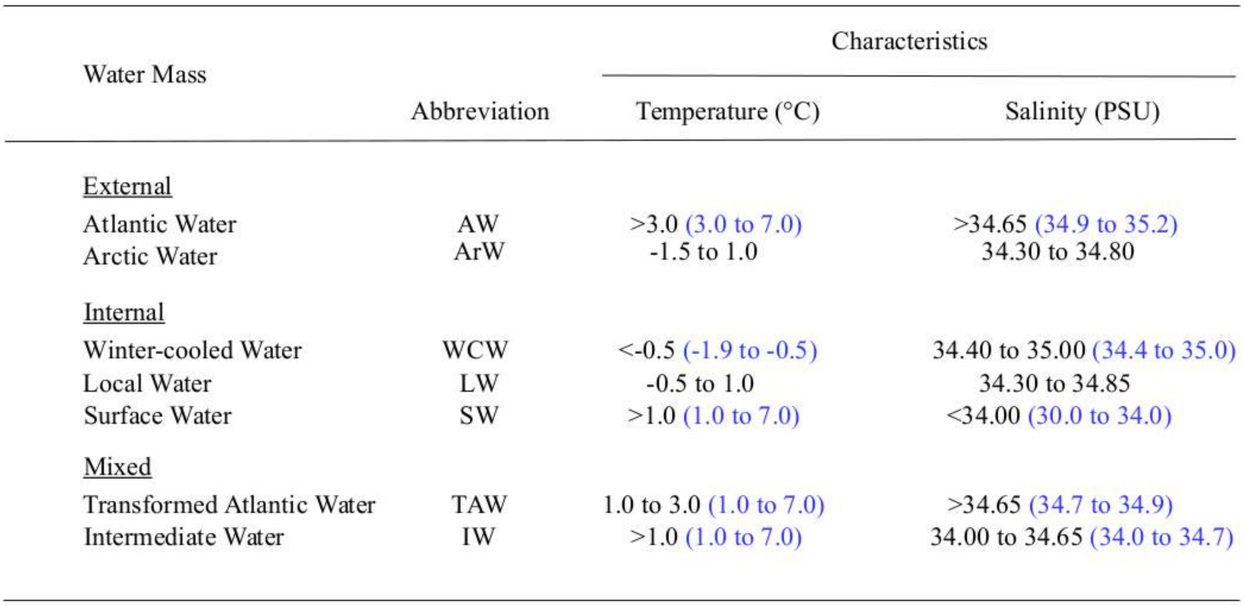

Water Mass	Abbreviation	Characteristics	
		Temperature (°C)	Salinity (PSU)
External			
Atlantic Water	AW	>3.0 (3.0 to 7.0)	>34.65 (34.9 to 35.2)
Arctic Water	ArW	-1.5 to 1.0	34.30 to 34.80
Internal			
Winter-cooled Water	WCW	<-0.5 (-1.9 to -0.5)	34.40 to 35.00 (34.4 to 35.0)
Local Water	LW	-0.5 to 1.0	34.30 to 34.85
Surface Water	SW	>1.0 (1.0 to 7.0)	<34.00 (30.0 to 34.0)
Mixed			
Transformed Atlantic Water	TAW	1.0 to 3.0 (1.0 to 7.0)	>34.65 (34.7 to 34.9)
Intermediate Water	IW	>1.0 (1.0 to 7.0)	34.00 to 34.65 (34.0 to 34.7)

Numerous tests have been carried out to characterize the masses of water present in the Kongsfjorden and study their characteristics. For example, in D'Angelo et al. (2018), a 6-year time series (2010–2016) of physical parameters and particle fluxes collected by an oceanographic mooring in Kongsfjorden are shown, providing an extraordinary opportunity to investigate seasonal and multi-year changes in the inner fjord. The results suggest that, as the Arctic temperature rises in a warming scenario, the flux of glacier-derived material will increase accordingly. Furthermore, water column stratification modulated by the inflow of warm Atlantic waters, especially in winter, will progressively hamper the exchange of nutrients from the bottom waters (Caroppo et al., 2017; D'Angelo et al., 2018). In Aliani et al. (2016) is described a report on the hydrology and ocean heat content (OHC) in Kongsfjorden, especially focusing on its innermost part. OHC estimates were based on calculations of the volume of water in the major basins of Kongsfjorden as inferred by a dedicate and accurate bathymetric survey and by CTD casts (Aliani et al., 2016). From these two examples, chosen among the many available in the literature, it is observed that typically the studies for the characterization of the water masses inside the Kongsfjorden are carried out using instruments installed on mooring and cast. In this thesis, a different approach was presented, based on the use of robotic platforms, paying particular attention to the acquisition procedures and to the data itself, also highlighting the close link with metrology and so the possibility to observe phenomena at a very detailed scale.

The analysis of the data collected during the 2018 campaign, carried out in the framework of the H2020 project "EXCELLABUST - Excelling LABUST in marine robotics", by performing transects at an increasing distance from the front of tidewater glaciers using robotic platforms, give us the possibility to observe the presence of different masses of water in the Kongsfjorden, in a new and better way than traditionally used systems, that are not able to reach a level of detail of the order of a few meters, necessary for the fine discrimination of the physical characteristics of water masses near glaciers. In particular, the use of the robotic vehicle for data acquisition, equipped with the Microstrain 3DM-GX3-35 for the positioning system, made it possible to locate and georeference the physical parameters of the water with horizontal position accuracy <2.5 m. During the water column sampling, the underwater position of the bunch of sensors is estimated at a point which, for shallow depths (and little current), can be considered within the uncertainty of the GPS measurement but which obviously degrades with increasing depth and current.

In the context of the oceanographic processes from tidewater glaciers in Kongsfjorden, here we focus on the Conwaybreen glacier (Fig. 8.2, right side) to discuss the importance of the results obtained.

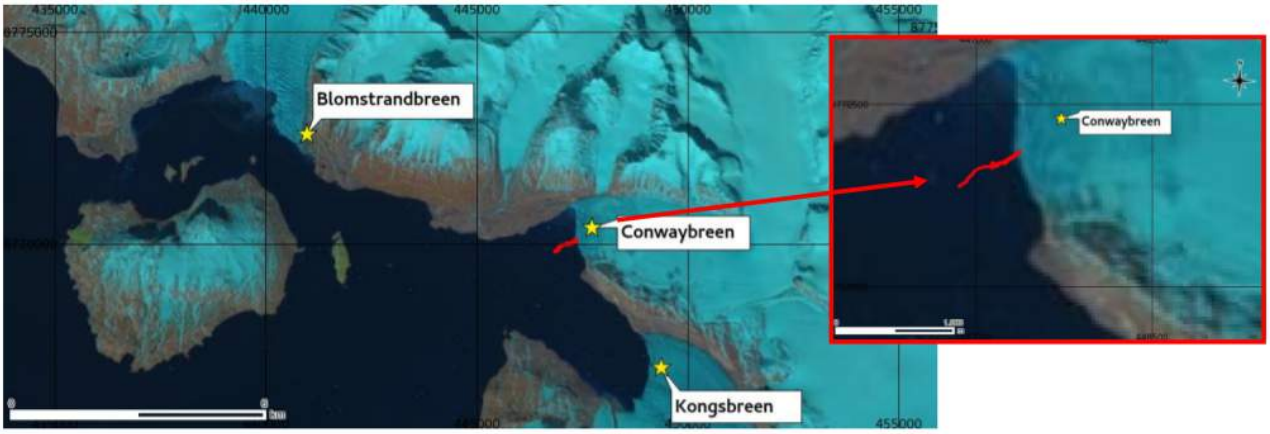

Figure 8.2 – Sentinel-2 satellite image showing the position of three tidewater glacier in the Kongsfjorden. In the red box on the right, the position of the Conwaybreen glacier front is shown together with the transect made with PROTEUS (red track).

In order to fully understand the importance of the results obtained, the classification of the different types of water masses shown in the table 8.1 was superimposed on Temperature-Salinity (T-S) diagram representing the water masses surrounding Conwaybreen glacier. The color scale is proportional to the distance from the glacier front. According to the water masses definitions shown in table 8.1, three water masses were identified in the fjord basin: Surface Water, Intermediate Water and Local Water. The stratification of water masses is due to freshwater runoff from glaciers, which creates SW characterized by salinity values below 34 PSU and temperatures above 1.0°C. IW is created by the merging of SW and LW (occurring during winter).

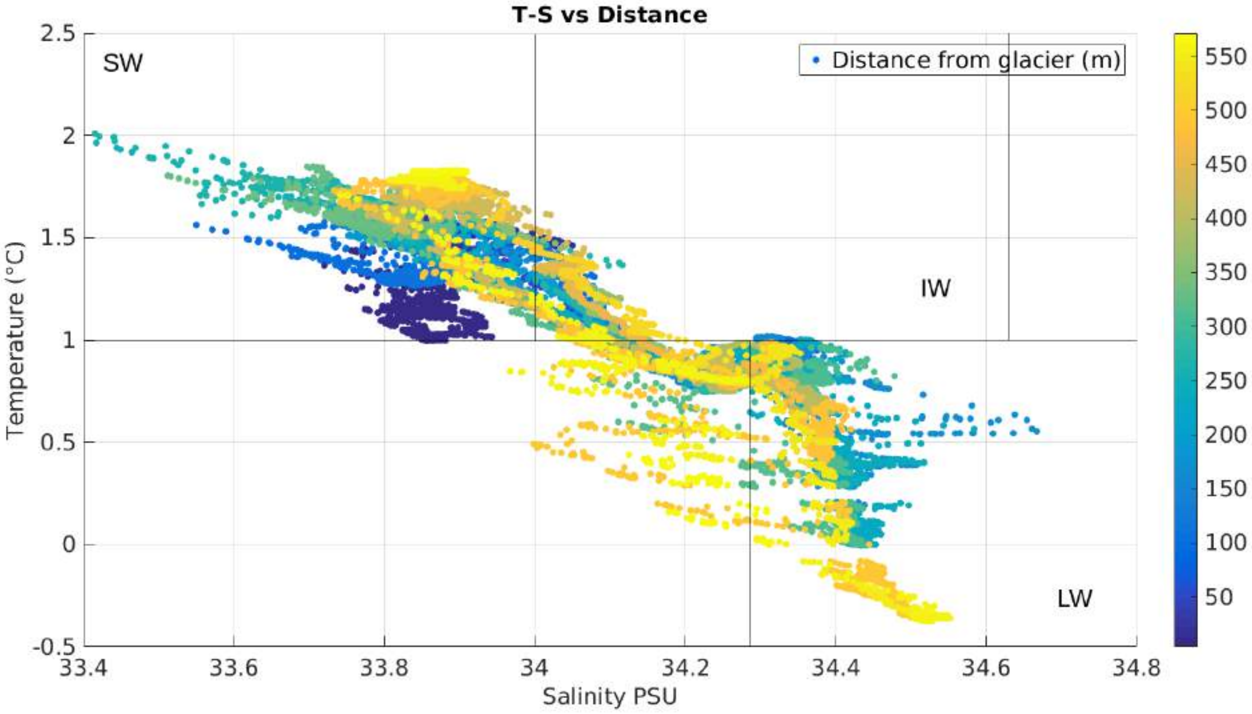

Figure 8.3 – T-S diagram for the Conwaybreen glacier front area: temperature (°C, y-axis) is plotted versus salinity (PSU, x-axis). The color scale is proportional to distance from the glacier front (m): yellow = far; blue = near. The classification of water masses as shown in the table 8.1 has been superimposed on these graphs: SW – Surface Water; IW – Intermediate Water; LW – Local Water.

The data of Figure 8.3 do not show the presence of a plume near the glacier front. This fact could be due to the progressive recession of the Conwaybreen glacier which makes it land-terminating, thus leading to an inflow of fresh water only at the surface level without the formation of a plume (Howe et al., 2019). However, there could also be other explanations: during the first ice melt season, the discharge flow is not strong enough to reach the surface or a high presence of sediment could affect the density of the plume, preventing it from reaching the surface and stratifying at an intermediate depth (Pasculli et al., 2020).

The layering of the water masses can also be studied as a function of depth with respect to the water surface. The presence of water masses characterized by different temperature and salinity values at different depths can generate vertical movements of the masses which affect the dynamics and circulation within the fjord. The following figure (Figure 8.4) shows the Temperature-Salinity graphs with the color scale proportional to the depth of the sensor with respect to the water surface.

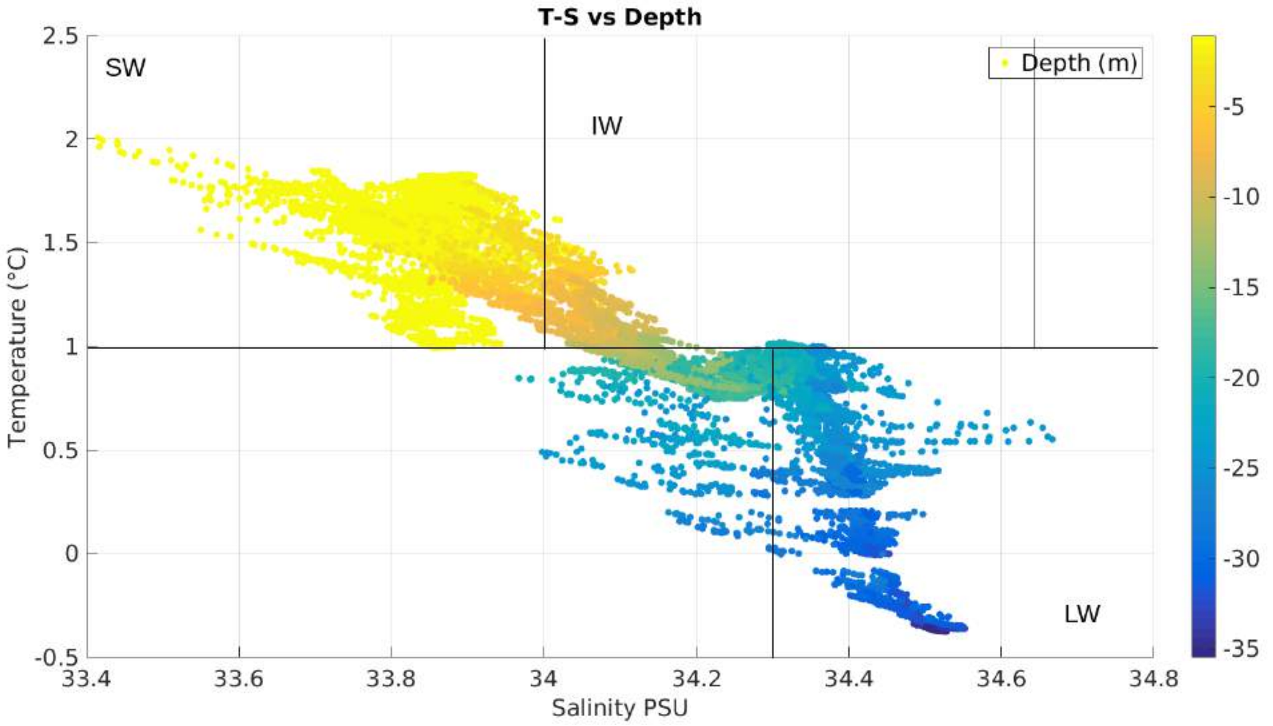

Figure 8.4 – T-S diagram for the Conwaybreen glacier front area: temperature (°C, y-axis) is plotted versus salinity (PSU, x-axis). The color scale is proportional to depth values (m): yellow = surface; blue = high depth. The classification of water masses as shown in the table 8.1 has been superimposed on these graphs: SW – Surface Water; IW – Intermediate Water; LW – Local Water.

We can see that Local Water (LW), characterised by Salinity higher than 34.3 PSU and Temperature below 1 °C, is typically found in the deeper layer of the water masses, at depth > -20 m.

On the contrary, the superficial layer, where the depth varies between the sea-surface and about -10 m, is characterized by the presence of Surface Water and Intermediate Water. The results discussed here are comparable with those described in Pasculli et al. (2020), obtained from the analysis of the data recorded using the ArLoC sensor prototype, developed by the research group of the University of Tuscia (Marcelli et al., 2010; Piermattei et al., 2018a) and mounted on-board PROTEUS during the 2018 EXCELLABUST campaign in Svalbard.

To fully understand the distribution of these masses of water, it should be emphasized that there are numerous factors that influence the dynamics inside the fjord. In particular, near the glacier front there is a strong inter-relationship between bathymetry and hydrography: bathymetric setting can influence local hydrographic conditions and hence lead to glacial front melt. A recent work carried out by Howe et al. (2019) shows in detail how bathymetry is an important factor in the hydrography near the glacier fronts, enhancing processes such as submarine melting, convection and mixing. Moreover it also shows the variety of glacial landforms in the seabed proximal to the grounded glacial front, whose characteristics can influence the phenomena related to the stratification of water masses (Batchelor, 2018; Dowdeswell et al., 2016).

The principal submarine landforms found in the proximity of tidewater glaciers in the Kongsfjorden (Kongsbreen, Kronebreen and Conwaybreen) are: large transverse ridges, which have been interpreted as moraines, indicating a period of time (‘still-stand’) of reduced glacial activity, producing focused proximal sedimentation in front of the glaciers; smaller, transverse and arcuate ridges, interpreted as De Geer moraines, showing the glacier front dynamism, result of seasonal movements at the active calving margin (Ottesen et al., 2006); glacial lineations, produced by subglacial erosion and deformation of the bed, well preserved in the larger, more active glaciers of Kongsbreen and Kronebreen. One of these glacier also displays a subglacial meltwater signature (with active meltwater plumes, visible at the surface), also during the 2018 EXCELLABUST campaign described in this thesis, suggesting that glacial dynamism is driven both externally (e.g. by water mass temperature (Luckman et al., 2015; Schild et al., 2018) as well as internally, (e.g. such as by the behavior of the glacier through processes such as surging); minor submarine features such as glacial erratics and iceberg plough marks. It is notable that most of these features are confined to the small glaciers, like the Conwaybreen. Iceberg plough marks, being the product of grounded bergs deforming the seabed they are in contact with, are more inclined to be preserved in shallower water (< 50 m), as is certainly the case with Svalbard tidewater glaciers which calve smaller icebergs. Both Kongsbreen and Kronebreen although highly active, are modifying the proximal seabed by draping from sediment plume deposition (Meslard et al., 2018) as well as the seabed being overridden and subsequently modified by surging.

Numerous published works deal with the study of the relationships between the morphology of the seabed and the oceanographic processes that occur near the fronts of the glaciers (Forwick et al., 2015; Howe et al., 2019; Lindbäck et al., 2018; Ottesen et al., 2006). In the work of Howe et al. (2019), models of the glacier fronts and seabed based on AUV observations are presented combining the oceanography with the bathymetric setting. These models suggest that bathymetry provides a strong control on glacier behavior, driving the water mass structure in the glacier front environment. It is interesting to compare the models regarding the different water masses identified in the Kongsfjorden, described by Howe et al. (2019), with the results obtained analysing the data acquired during the 2018 EXCELLABUST campaign and described in this work. Our data were collected at the end of May-beginning of June 2018 (late spring) while those of the article Howe et al. (2019) were collected in the first half of August 2017, therefore in summer. The seasonality conditions can justify some differences found in the results obtained but they are not the only causes behind them. These are also due to the fact that the autonomous surface system PROTEUS is able to monitor in detail the variations in the physical and bio-geo-chemical parameters with great accuracy and at high resolution, greater than those that can be obtained with an AUV system, characterized by lower performances linked to the lower precision of underwater acoustic positioning.

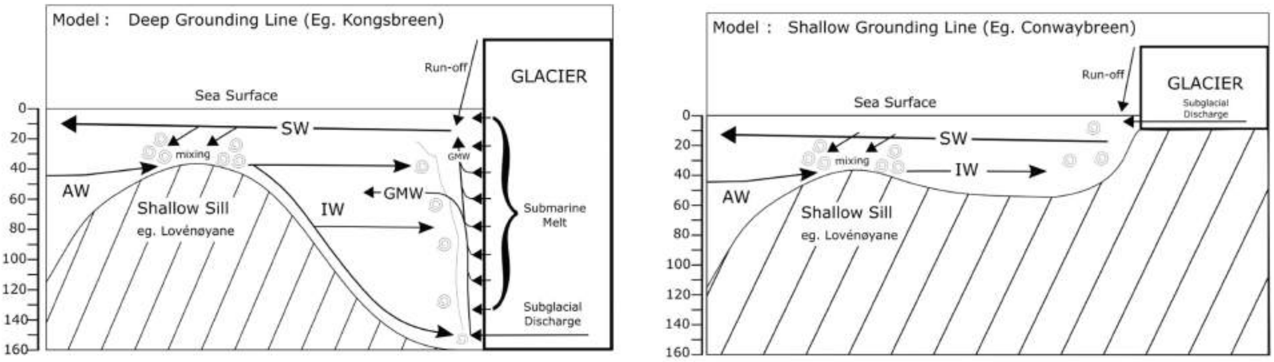

Figure 8.5 – Model cartoons illustrating the influence of glacial grounding line depth and ice-proximal bathymetry has on driving fjordic circulation, based on the AUV observations from the western Svalbard tidewater glaciers. Water depth is shown on the left hand side of each model, and is based on data from Forwick et al. (2015) and Howe et al. (2019).

The graphs in figure 8.5 illustrate models of the processes taking place near glaciers also examined in this thesis (Kongsbreen, left; Conwaybreen, right). In all the models the controlling factor is the near-glacier (~0-10 km) bathymetry of the fjord, which drives the local hydrography and hence circulation. In particular, the scenario encountered at Conwaybreen is illustrated by the right model of figure 8.5. Here in a "shallow grounding line" model, AW becomes modified by SW as it enters the fjord. Only a small portion of the glacier sits within the fjord waters and there is no deep buoyancy injection (as in the Kongsbreen case). The shallow basin holds only predominantly SW, with IW at depth. The majority of the IW appears to be exported from the glacier as it moves to exit the fjord. AUV observations of Conwaybreen suggest further modification of IW with fresh run-off from subglacial discharge into the surface waters. Whilst the inferred hydrography and bathymetry of these models is supported by the near-glacier AUV data, in this scenario, the position of the shallow sill is suggested to be the Løvenøyane islands or other inshore restrictions in the fjord. Comparing the results of Howe et al. (2019) with our results, it is possible to find the presence of SW in the upper layer (see figure 8.4) but the IW, even if present in some quantities, is largely substituted by the presence of LW in the deeper part of the water column (blue dots of figure 8.4).

As bathymetric setting can influence local hydrographic conditions and sills within the fjord can promote mixing and local circulation in front of shallow grounded glaciers, the data acquired by means of the CTD lowered along the water column at increasing distances from the glacier front were analyzed taking also into account, for their interpretation, the data acquired from the altimeter mounted on board the robotic vehicle which allows to reproduce the trend of the seabed.

The following graph (Fig. 8.6) shows the descent profiles of the CTD (blue dots) and the range values of the seabed (orange dots) relative to the Conwaybreen glacier front.

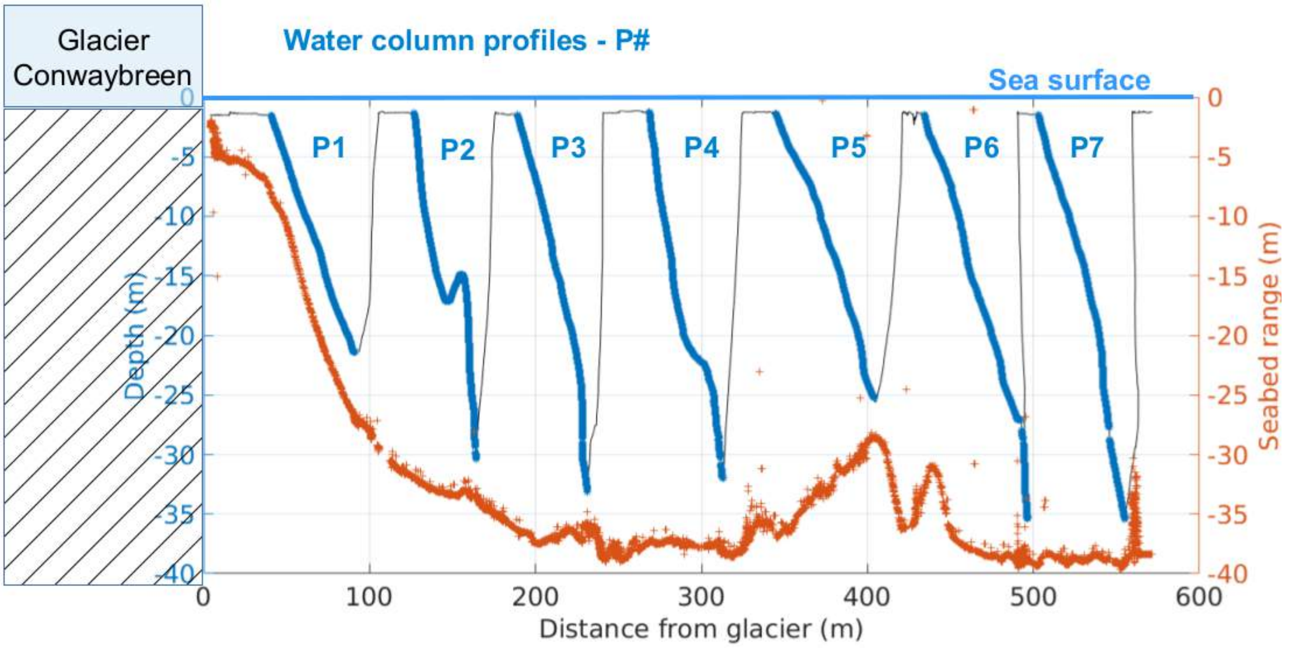

Figure 8.6 – Graph showing descent CTD profiles (blue dots) and range values of the seabed (orange dots) relative to the Conwaybreen glacier front.

Considering the values of Salinity (PSU) and Temperature (°C) acquired along these vertical profiles we obtain the following T-S graph, in which the different profiles are shown with different colors.

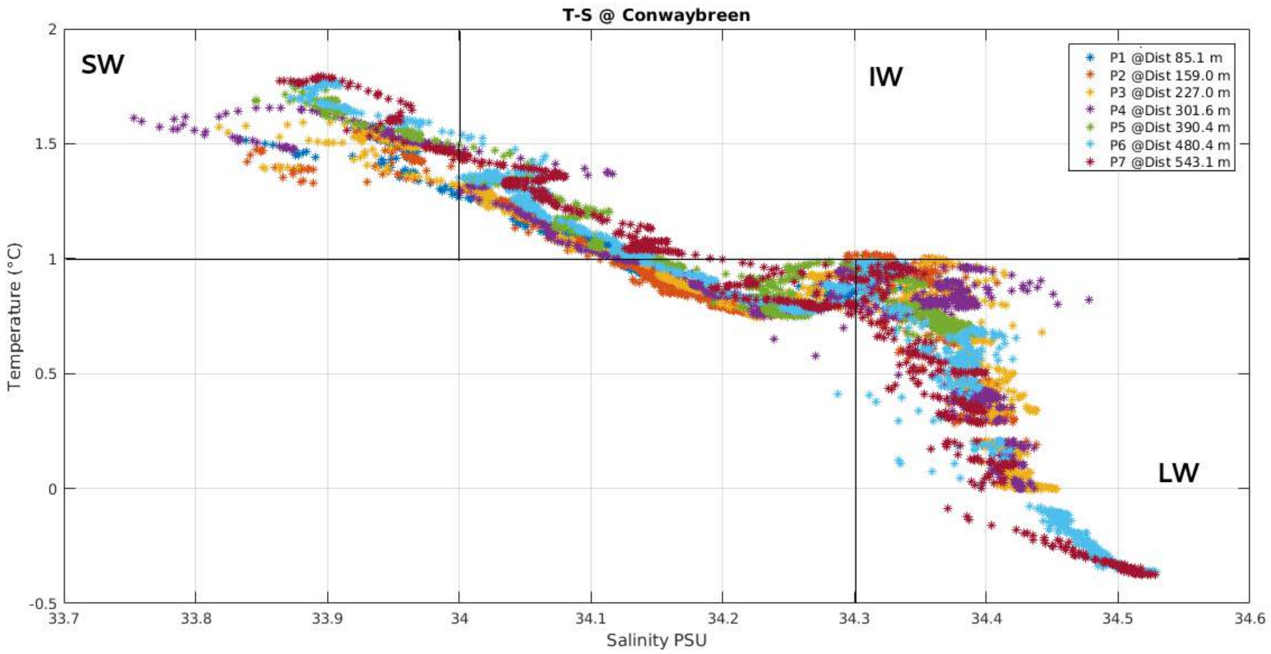

Figure 8.7 – Graph showing in different colors the Temperature (y-axis, °C) and Salinity (x-axis, PSU) data of the different vertical CTD profiles. Different water masses are identified based on the values of the Table 8.1

Comparing this graph with the one where T-S data are plotted as a function of the depth with respect to the surface (figure 8.4) and considering the water mass classification of table 8.1, three different water masses can be identified, in a range that goes from the sea surface to a depth of about 35 m. The novelty of this work consists in the ability to identify the presence of a new water mass together with the SW (visible in the upper left part of the previous graph) which is not present in any of the classifications mentioned above. This new water mass is clearly visible by analyzing the semi-logarithmic scale graphs of Temperature and Chlorophyll-a of the P6 and P7 profiles compared, for example, to P4 and already shown in the data analysis chapter (See Figure 4.26 and 4.27). These graphs show important inflection points in the variables Temperature and Chlorophyll-a, compared to the expected trend. We call this new mass "Sill Surface Water" (SSW) as its presence is related to the boundary effect created by seabed morphology on the distribution of the water masses at about 300 meters away from the glacier front. The P4 profile (purple dots of figure 8.7) correspond to the limit, discriminating the SW from the SSW. The presence of this water, characterized by lower temperature and salinity values, can be associated with melting processes taking place at the edge of the glacier. Furthermore, the observation of the SSW mass, not mentioned in other works, can also be related to the measurement procedures and the instrumentation used in the 2018 EXCELLABUST campaign. Investigations near glacier fronts are typically performed using AUVs. These tools are characterized by a high degree of autonomy and the ability to map the environment in a three-dimensional way. On the other hand, they have a lower capacity to discriminate punctual measurements and are also affected by higher uncertainties on the positioning as they use underwater acoustic systems, less precise than systems operating in the air. In the campaign described in this thesis, on the other hand, a robotic system that operates in the water surface was used but with capabilities to acquire parameters also along the water column, thus guaranteeing high positioning accuracy. This allowed us to observe new transient phenomena, characterized by non-repeatability, with high precision, like for example the aforementioned observation of the water masses stratification not only along the vertical profile but also at increasing distance from the glacier front, in correspondence of a particular seabed morphology that creates a boundary effect on the distribution of the water masses.

The complexity of the surface water layer (SW+SSW) must also be interpreted by taking into account the state of the fjord’s waters as a whole. The measurements of the 2018 EXCELLABUST campaign, in fact, were made between the end of May and the beginning of June. In this period the fjord is characterized by more than a month of open waters, as confirmed by the Sentinel 2 images which show how the surface layer of ice opened in April, making the effect due to the intrusion of warmer Atlantic water almost negligible when the measurements were made (Figure 8.8). In this condition, the melting processes, highlighted by the presence of high turbidity values in the surface layer, continue to take place at the edge of the glaciers.

The information on the general state of the fjord, obtained with Sentinel 2 satellite images, can be integrated with the precise data of the meteorological conditions in the tests area recorded by the AirQino system, as described in chapters 3 and 4. The meteorological conditions close to the glacier front (temperature, humidity, wind) influence the generation of transient phenomena observed in water as they can induce the melting of the ice. During the 2018 campaign there was a temperature between 6 and 18 ° C with humidity conditions between 32 and 58% and calm or non-existent wind. These meteorological conditions have therefore contributed to triggering processes on the glaciers that lead to the observation of transient phenomena in the layers of the water mass.

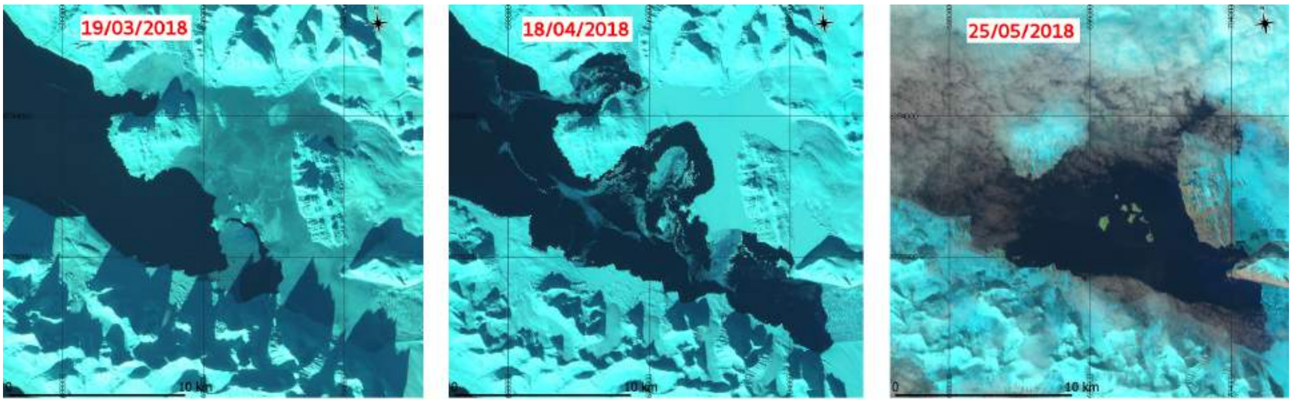

Figure 8.8 – The three images are obtained from Sentinel-2 data and show, from left to right, the progressive melting of the fjord's surface ice layer due to the intrusion of warmer Atlantic water. In March (left picture) the ice cover started to melt; subsequently it is seen that in April (central picture) the melting had already largely occurred and that at the end of May (right picture), period in which the tests were carried out, the fjord was free from ice cover for over a month.

The added value of this work was therefore the ability to record these transient variations in the trend of the variables of interest, at a level of resolution that allows an extremely detailed discrimination of the processes that occur at the edge of the glacier front, not directly related to the seasonality effects but due to the internal processes that take place inside the fjord, like freshwater runoff, surface heat fluxes, vertical mixing and wind forcing, to name a few of them.

Another mechanism linked to the melting of the ice at the edge of the glacier for a fjord in open water condition (without the ice sheet cover) and already documented in literature, is the possible presence of internal waves, inducing mixing and heat redistribution processes (Alford et al., 2016; Buijsman et al., 2019; Fer, 2014). Internal waves are a key process linking the large-scale mechanical forcing of the oceans to small-scale turbulence and mixing. Surface waves propagate at the interface between air and water, which is a strong density gradient. Internal waves propagate along weaker gradients (pycnoclines) within density-stratified fluids, behaving similarly to surface waves but spanning the entire vertical stratification of the water column. Studies of internal waves are based on oceanographic measurements (temperature, salinity, velocity), as well as optical and radar satellite imaging and numerical simulations (Pomar et al., 2012; Sarkar and Scotti, 2017).

The generation of internal waves is determined by external forcing by wind and tides that are important source of energy. In the Arctic, the generation of internal waves is primarily a result of surface forcing by wind and the motion of sea ice (D'Asaro, 1985), both of which transfer momentum to the ocean surface mixed layer (Cole et al., 2018; Dosser et al., 2014). However, internal waves in the Arctic region are characterised by low wave energy levels, attributed to the presence of sea ice, which causes dissipation of internal waves in the under-ice surface boundary layer, limiting energy propagation (Fer, 2014; Morison et al., 1985; Slinn et al., 1998). The rapid Arctic sea ice decline and changing sea ice properties have impacts on internal wave generation, propagation, and energy: as the climate shifts and polar temperatures rise, ice cover in the Arctic is reduced and we may see an increase in wind-generated internal waves, which may result in enhanced mixing and redistribution of heat, which will further reduce the ice-cover (Dosser and Rainville, 2016; Morozov et al., 2011).

Internal waves influence nutrient, plankton and larval distributions while inducing thermal variations by vertical displacements of the thermocline, which can also create thermal stresses in benthic communities. Moreover, they can induce mobilization of bottom sediments, affect sedimentation patterns and bottom gradients, thereby shaping the continental slope and its geological history (Cacchione et al., 2002; Pomar et al., 2012). Internal waves are relevant not only for ocean mixing, dispersal of matter and thereby influence on local biology and geomorphology, but also for their impact on ocean structures, ocean acoustics, and submerged vehicles navigation (Osborne et al. 1978; Sarkar and Scotti, 2017). Conventional acoustic means of submarine detection and navigation are complicated by the deflection of acoustic rays by the rather random variations in sound speed induced by internal waves (Apel, 2002; Buijsman et al., 2019; Inall et al., 2001; Scotti and Pineda, 2004). The influence that internal waves can have on the propagation of acoustic signals underwater is a particularly interesting point for the activity described in this thesis: the use of underwater robotic vehicles could be affected by this fact which could create problems during data acquisition, especially in the case of sampling underwater. The disturbance factor created by the presence of internal waves must therefore be taken into consideration in planning the data acquisition procedures during the field campaign. This is an important possible source of hazard as a loss of acoustic communication due to the influence of internal waves can have harmful effects, possibly leading to the loss of the vehicle and all the instruments on board.

We have seen how the effects of the presence of internal waves can be multiple and, in some cases, dangerous. However, it is difficult to detect their presence within the fjord waters due to their low energy level. Being able to distinguish the contribution coming from the internal waves from that due to other phenomena with similar effects requires the planning of acquisition campaigns near the glacial fronts, specifically structured for their identification: acquisition of data that allow a study of the trend of the physical and bio-geo-chemical parameters of the water column, repeated for time intervals appropriately correlated with the times of tides and in parallel acquisition of weather and sea conditions data within the fjord. The data at our disposal acquired during the 2018 EXCELLABUST campaign cannot be used to support the presence of internal waves because they were acquired with different methods and purposes. However, this issue can provide interesting insights for future acquisition campaigns.

Generally speaking, with this work it was possible to record phenomena showing that the dynamic of the water masses in the fjord system is influenced by numerous factors, generating both vertical movements (differences in temperature and salinity together with differences in density also influenced by parameters such as turbidity and chlorophyll-a) and horizontal movements (external forcing due to the wind and internal due to the morphology of the seabed). From the observation of the results related to this data acquisition campaign, there seems to be a prevalence of the vertical movement, driven by the intrinsic characteristics of the water masses, compared to external forcing causing horizontal movements. Being able to observe and record the interactions between the physical and bio-geo-chemical parameters of water in the context of the critical Svalbard environment at such a level of both spatial and temporal detail is essential to understand these water masses movements, to study their origin and follow their effects. Using PROTEUS, it was therefore possible to carry out a complete characterisation of the environment near the glacier front, acquiring in situ data with space/time resolutions not obtainable with traditional observation methods and highlighting fundamental phenomena related to the water mass stratification not previously recorded at such a level of details.

8.2 Shallow water gas emissions in the Scoglio d'Affrica

To analyze the second case study of this thesis it is necessary to leave the Svalbard and move thousands of kilometers away, towards the northern Tyrrhenian Sea where phenomena of seabed gas emissions, which are the subject of our investigations, take place. Despite the apparent diversity, the phenomena described in the two case studies (water mass stratification with possible presence of plume of meltwater from a glacier in Svalbard and seabed methane emissions in the Tyrrhenian sea) share some characteristics: both are events strongly localised in space and time, non-repeatable and not completely predictable. These distinctive features require the development of dedicated observation procedures, which on the one hand consider the constraints imposed by the environment in which operations take place, and on the other hand, are able to satisfy the requests in terms of spatial and temporal resolution and accuracy, necessary to record these transient events.
In parallel with the development of specific observation procedures, it is necessary to use instruments and tools that are able to overcome the limitations associated with traditional methods of observing this critical marine environment. In this perspective, the use of autonomous robotic platforms characterised by ease of assembly and adaptability, equipped with instrumentation capable of operating even in demanding working conditions, is of fundamental importance.
The complexity of the phenomena to be studied and the lack of data still present, rise the need to develop integrated observation systems with the introduction of marine robotics, in order to characterise the area from different points of view: various geophysical, biophysical and morphological signatures associated with active seeps can be detected through both optical and acoustic techniques (Mitchell et al., 2018). Moreover the capabilities of observing cold seep morphologies from a close distance using ROV allow to reveal the near bottom characteristics at metric resolution. This knowledge is one of the important aspects to characterise cold seep activity, their formation and explanations of their space-time evolution (Klaucke, 2018).
Cold gas emissions from the seabed characterise the area between the Scoglio d'Affrica, the island of Pianosa and the island of Elba. Numerous studies and data acquisition campaigns were carried out since the sixties and in June 2019 the Italian Hydrographic Institute coordinated a scientific campaign in the area of the Scoglio d'Affrica in collaboration with other research centers, in order to continue the annual monitoring program already started in 2017.
In this thesis, the combined use of a newly designed robotic vehicle and of acquisition procedures specifically conceived to cope with the criticality of the operating environment are described. During the 2019 campaign, the ROV e-URoPe was used for the collection of video images in a sub-area of interest of the larger area inspected with the high resolution MBES from ship (ITS Magnaghi, Italian Navy Ship) and from support boats. About the use of the ROV, the problems related to the underwater positioning initially encountered were solved in a second instance by integrating the information from the ROV telemetry with the acoustic data from the multibeam survey. This made possible to obtain results with a resolution in space (less than 1 meter) and time (from minutes up to hours) that allow both instantaneous interpretation of the data, for alert purposes in the event of a hazard, and long-term interpretation, to study the evolution of the degassing events taking place in the area surrounding the Scoglio d'Affrica.
Once georeferenced and integrated with the acoustic data from MBES, the video images were used to create a map of the emission points in the area of the Scoglio d'Affrica. The following figure

shows the bathymetric map of the area inspected during the campaign where the green crosses and letters identify interesting points obtained as a result of the analysis of the video images.

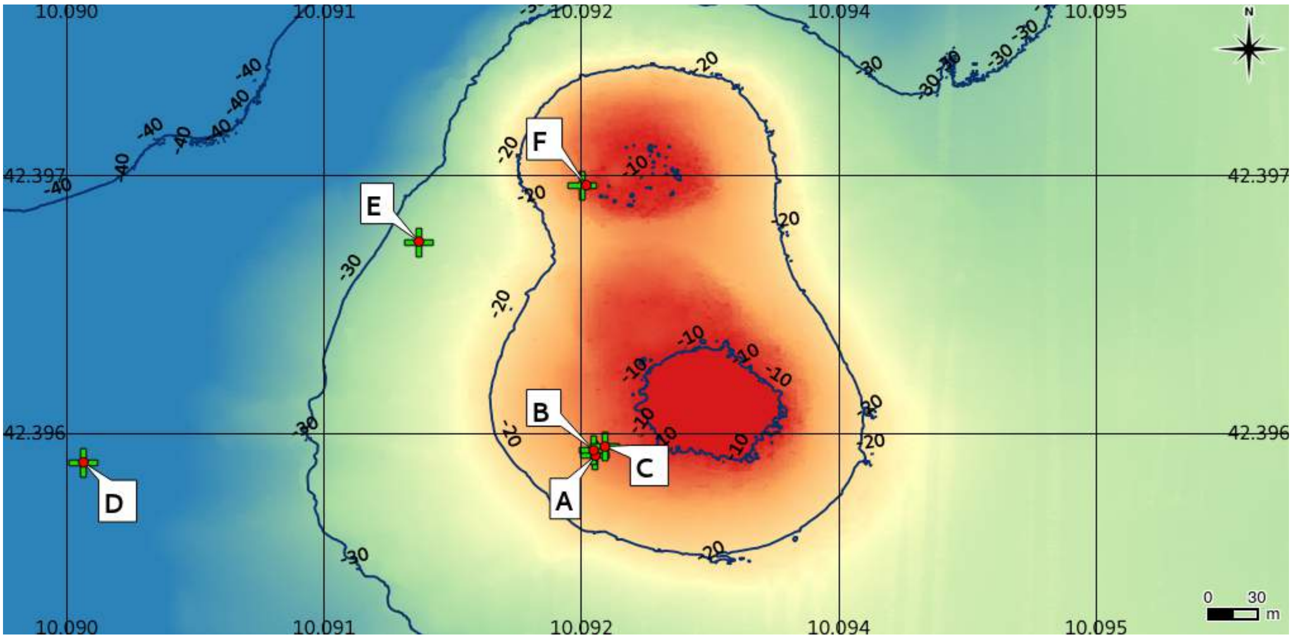

Figure 8.9 - Bathymetric map of the area inspected during the 2019 campaign. The green crosses and the letters highlight a selection of interesting point obtained as a result of the analysis of the video images.

However, mapping the emission points is only the starting point of the analysis. The step forward was to use the new data acquired with the ROV to enrich the morphological and geochemical information known in literature and obtained from previous campaigns carried out in the same area. Thus, the video data are essential to add value and create relationships between the morphology of the seabed, the composition of the sediments and the geochemistry of the gases.

Cold seeps are, in general, associated with several different seafloor structures such as mud volcanoes, pockmarks, diapirs, carbonate-related constructions (mounds, chimneys, crusts, plates), brine pools, oil and gas vents (Klaucke, 2018). Based on the morphology as well as the sedimentary, petrographic and geochemical characteristics of the solid materials analysed together with the fluids expelled from the Scoglio d'Affrica site, the seeps of the area are classified as a mud volcano (Saroni et al., 2020). Submarine mud volcanoes are positive geological structures formed by the extrusion of gas (mainly methane) and water-saturated fine-grained sediments; they are often associated with mud breccias and specific morphological features like a central crater and mudflows.

One of the main results obtained by analyzing the videos acquired with the ROV is the possibility not only to characterize the environment in support of the traditional geochemical and morphological analyses but also to observe degassing processes extremely localised in space and study their evolution over time, opening a window on the dynamics of the emission processes also in spatial terms..

To this end, a table (Table 8.2) that summarizes the main features of the points of interest, obtained integrating the ROV data with the morphological data from Casalbore et al. (2020) and the geochemistry of the area known in literature (INGV – Rapporto Tecnico, 2017; Saroni et al., 2020) is created in order to give hints of the mechanisms that originate some of the observed phenomena.

*Table 8.2 - Table showing details about the selected point of figure 8.9: position coordinates (WGS84 – EPSG 4326), depth of the seabed (m), seabed type, presence or not of gas emission and the image of the area extracted from the video. * = morphology data as indicated in Casalbore et al. (2020); ** = geochemistry data as indicated in INGV-Rapporto tecnico (2017) and Saroni et al. (2020).*

Point identifier	Latitude	Longitude	Depth (m)	Seabed type	Gas emissions	Video image	Morphology (*)	Geochemistry (**)
A	42.39551	10.09251	-14.64	Sand + sparse rocky sediments	Not present	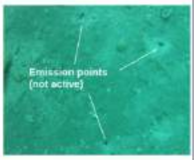	Lobate flow	Methane (>95 vol%) (thermogenic gases)
B	42.39554	10.0925	-14.52	Sand + large blocks with algae cover	Present	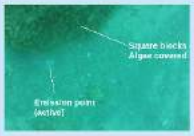	Lobate flow	Methane (>95 vol%) (thermogenic gases)
C	42.39556	10.09256	-13.33	Sand+ sparse rocks	Present	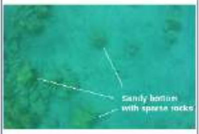	Lobate flow	Methane (>95 vol%) (thermogenic gases)
D	42.39547	10.08977	-36.54	Posidonia oceanica	Not present	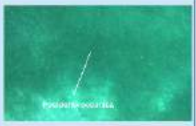	Old sediment covered with Posidonia oceanica	n/a
E	42.39665	10.09157	-28.09	Sand+mud beccia and rocks	Present	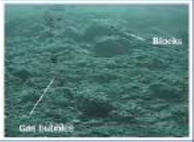	Sediment flow	Methane (>95 vol%) (thermogenic gases)
F	42.39695	10.09244	-12.31	Sand with ripples+ blocks with algae cover	Present		Lower and Smooth Slope (LSS) - sparse rock	Methane (>95 vol%) $\delta^{13}C$ CH_4 from -30‰ to -50‰ (thermogenic gases)

Points A, B, C are on the western front of the southern mound (Figure 8.9), responsible for the violent emission of March 2017. These points are located at a depth between -13/-14 m on a hillside that slopes gently towards the deepest part. In this area the seabed is mainly sandy, with scattered rocky blocks. From the point of view of morphology, the area is characterized by multiple lobate mudflows on the side of the mound, some of which have a fresh-looking morphology and most not colonized by Posidonia oceanica meadows, suggesting a repetition of eruptive events in recent times, supported by an overall smooth morpho-acoustic facies (FSS) (Casalbore et al., 2020). In this area, emission activity consisted in trains of bubbles of centimeter size coming out intermittently from small holes of centimeter size. Furthermore, in the area of point A, holes in the seabed no longer emissive (or not-emissive in the observation time) were identified. This information is useful in order to study the temporal evolution of emissions points.

From a geochemical point of view, this area was investigated in 2017 with two different campaigns on behalf of the Civil Protection and described in INGV - Rapporto Tecnico (2017). The investigations carried out highlighted a gas composition with a prevalence of methane (> 95 vol%) with some secondary components of CO_2 and He. These results are compatible with gas analyzes carried out in the Scoglio d'Affrica area dating back to the end of the 1960s which found emissions composed mainly by methane, with an average composition of CH_4 88%, N_2 7%, O_2 4%, CO_2 0.2% (Barletta et al., 1969; Del Bono and Giammarino, 1968) and also with the analyzes carried out on gas sampled by the HYDRA Institute in 2011 and reported in Meister et al. (2018) from a site located about 1 km to the north from the Scoglio d'Affrica sampling area.

Moving further to the west side, there is the point D at a depth of about -36 m. Here the area is characterized by the presence of Posidonia oceanica, developed on a seabed characterized by old sediments and gradually colonized. No emission activities were observed in this area. The morphological map of the zone classifies this area as old sediment flow covered with Posidonia oceanica. Moving toward the North, we identified the Point E, located in the western part of the northern mound (Figure 8.9) and at a depth of approximately -28 m. The area is characterized by sand alternating with mud breccia and rocks, morphologically identified as sediment flow. In this area, emission activities consisted in small bubbles, intermittent and originating from sediment, were observed. Going up the slope of the western side of this mound, the morphological structures are Lower and Smooth Slope (LSS), divided in sub-facies according to the density of the blocks (Casalbore et al., 2020). In this area there is the F point, located at the boundary of the top part of the mound, in a shallow water area (about -12 m). Here the video images show a sandy seabed with ripple, contoured by blocks of rock mostly covered with algae. This fact indicates that the blocks were colonized since some time and that the emissions in this area occur from contact points between the sandy bottom and the rocks, not in an explosive manner and therefore without disturbances for the morphology of the area.

All these observations were used to elaborate the following figure (figure 8.10). This thematic map was created by integrating information from different sources: the bathymetric map obtained from the processing of acoustic data from MBES acquired by the Hydrographic Institute of the Italian Navy (IIM), the map showing the classification of the morphologies of the seabed, described in Casalbore et al. (2020), and the morphological information at high level of detail obtained from the video images acquired with the ROV. The interpretation of the map is supported by the results obtained from the geochemical analysis carried out in the area (Saroni et al., 2020). The presence of specific morphological structures can help in understanding the origin of the emissions, typically in the sediment and not from fractures in the rock, and also to retrieve information about the porosity of the seabed, as for the same type of seabed and substrate, the emissions are different according to it.

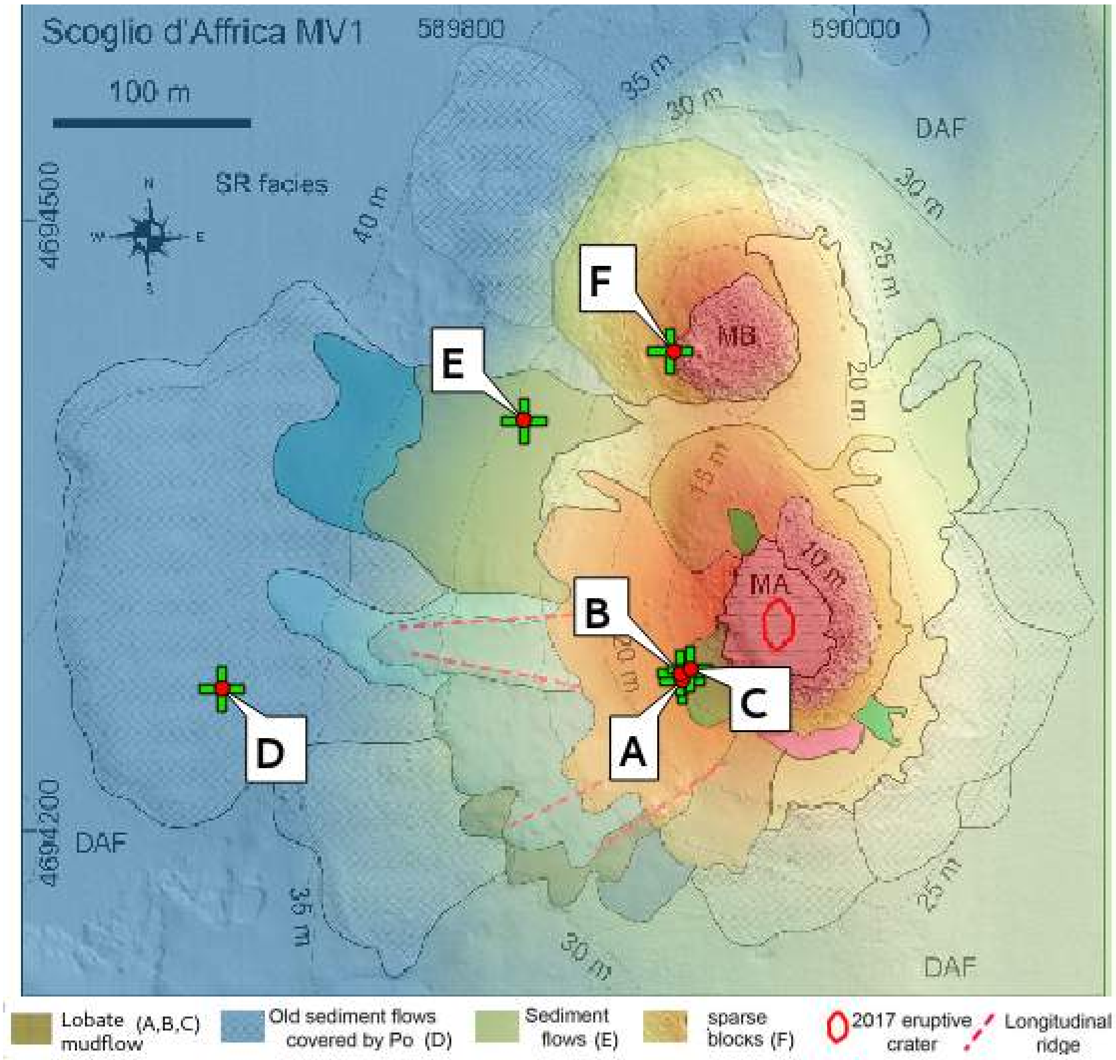

Figure 8.10 - Thematic map created integrating the high resolution morphological information from the ROV video, the bathymetric map obtained from the processing of data from MBES acquired by the Hydrographic Institute of the Italian Navy (IIM) and the map showing the classification of the morphologies of the seabed, described in Casalbore et al. (2020). Each point (A,B,C,D,E and F) is characterised by specific characteristics, detailed in table 8.2.

From this thematic map it is also possible to make some assumptions about the age of the morphological structures observed in this area: the points A, B, C and F, located near the summit of the volcanoes (shallowest area) consist of recently formed morphologies; point E, in an area at an intermediate depth, is made up of older sediments that flowed along the slope. Point D, on the other hand, is made up of much older sediments, now completely covered with Posidonia oceanica.

Moreover, from a geochemical point of view, there is a detailed analysis of the area surrounding point F, described in Saroni et al. (2020). As previously stated, this point is located near the northern mound, in an area characterized by a sandy bottom with large scattered rocky blocks. Observations made in 2018 showed that the gas was emitted as large bubbles (up to 15 cm in diameter) from conical mud mounds. In the mud volcano area, porewater and seawater samples did not show significant differences from the water samples taken outside the area. The pH was around 8.00 and salinity was about 38 PSU (Saroni et al., 2020). Also, the gas chemistry of the collected samples was typical of mud volcanoes (Etiope et al., 2009a; Etiope et al., 2009b), with methane as the prevalent gas component (>95 vol%) and minor gases which include carbon dioxide, nitrogen and heavier alkanes and helium, whereas CO was present in trace amounts. To assess the origin of the hydrocarbon gases, the stable isotopes as well as the molecular composition were analysed. $\delta^{13}C$ CH_4 values from -30‰ to -50‰ were interpreted as thermogenic gases. Moreover, the samples collected at Scoglio d'Affrica were extremely depleted in ^3He, with $^3He/ ^4He$ ratios values showing typical values for a gas crustal emitted from a geological setting in which the radiogenic helium component is strongly dominant (Saroni et al., 2020).

Carrying out our observations in the same area but one year later, we still saw emissive activities but of a different nature: the bubbles were intermittent and of reduced size. Moreover, from the analysis of the video data it was possible to obtain a semi-quantitative analysis of the emissions, by estimating the amount of gas emitted. This fact creates an added value to the ROV data compared to the observations made using human operators: using the ROV in hovering mode, in fact, it is possible to lengthen the time spent at each point of interest in order to acquire data for an estimate of the emission volumes.

From the comparative analysis between the results known in the literature and the observations made with the ROV, it is possible to advance some hypotheses on the temporal evolution of the emissive sites, that can evolve either towards a depletion of the emission activity with time (fewer and smaller bubbles emitted) or towards an accumulation of gas in the substrate that increasingly struggles to find a way out, and which could then again manifest itself suddenly with a violent explosive activity. In this case, the system could have much greater emissive capacities than those observed experimentally with the ROV and this fact could be an important source of hazard. For all these reasons, continuous and integrated monitoring of these emission sites is of fundamental importance.

Chapter 9

Concluding Remarks

The work described in this thesis has an interdisciplinary value as it analyzes the difficult task of carrying out measurements and observations of transient phenomena in critical environmental conditions from different points of view. The metrological approach is a central point of this work as it is fundamental to characterise the measurements and necessary to give an interpretation of the results obtained in a rigorous way in terms of comparability, consistency and traceability and to identify specific phenomena that can be seen as "anomalies" in the trend of the data.

From a metrological point of view, specific characteristics are also required in terms of repeatability, accuracy and resolution of the measurements made. This is a particularly critical point and very often it is not possible to reach certain minimum levels necessary to obtain valuable results from the collected data, especially if traditional methods applied in critical contexts are used. A possible solution to this problem derives from the introduction of robotic autonomous vehicles: these can be exploited to obtain data with characteristics of precision and resolution that allow to obtain valuable information on the observed processes. Despite autonomous platforms already provide key observations for environmental assessment, further advances in autonomous systems are required to meet the growing ocean observation needs in different scientific fields like biology, biogeochemistry, seabed mapping, deep ocean, and Polar exploration together with the growing needs for real-time data. The use of robotic systems as fundamental data-gathering tools by scientists, allow new perspectives and a greater understanding of the planet and its processes, also taking advantage from the possibility to mount sets of tools on board for a complete characterization of the environment, even critical, with spatial and temporal resolutions not otherwise obtainable, as extensively described in this work.

The development of acquisition procedures adapted to the use of robotics and guided by critical environmental constraints constitute a fundamental element for the observation of transient processes. The two examples presented as case studies in this thesis, permit to show the importance of the methods used for the acquisition of the data, with a focus on measurements and their interpretation from the point of view of environmental science. By applying the methodologies developed and described in this work, valuable results are obtained: stratification processes of the water masses, highlighting internal effects due to the morphology of the seabed that created boundary effects, were observed with an unprecedented level of detail. These processes refer to the case study in Svalbard but, suitably adapted and integrated with geochemical and acoustic data, they can be applied to the identification of gaseous emissions in the Tyrrhenian Sea.

Operating according to methods and procedures adapted to the environment made it possible to overcome the failures of the technological and instrumental part that sometimes occurred due to the hostile conditions of the environment in which the acquisition campaigns were conducted. What at first glance might appear to be weaknesses of the system, actually turned out to be important food for thought for future evolutions. The integration of data coming from different sources allows also to obtain important results from the point of view of measurement and its interpretation. This is a fundamental aspect of this work, which opens important scenarios in future applications.

Moreover, the methodological and data analysis approach used can be extended and applied also in other case studies and in other environmental situations where the quality of the data and its interpretation, also from a metrological point of view, are fundamental. An example of this possible adaptation of the observing methodologies used can be the identification of the presence of Posidonia oceanica on the seabed. The presence of this plant on the seafloor can be identified as an "anomaly" in the captured video images or in the acoustic spectra compared to the data acquired in areas where the Posidonia is not present. The identification approach, in principle, has characteristics similar to that used to identify the presence of a plume of melt water from a glacier or the presence of gas bubbles in the water column. This example shows, once again, how the work described and proposed in this thesis provides an approach to the observation of the environment focused on the measurement and its interpretation, to obtain the characterization of extremely localized events in space and time with extremely high levels of detail.

A further and important step forward toward an integrated observation of the marine environment is the need to improve interoperability of sensors, systems, and data. The use of standards and best practices for observations make it easier to operate efficiently, share results and exploit existing data, promoting interoperability and reproducibility of the results obtained. In this perspective, the use of autonomous platforms, allow to acquire a greater volume of standardized and high-quality data, improving the comparability and reducing the uncertainty. To effectively achieve this goal, it is necessary to combine the skills acquired in the traditional fields of metrology with the new interdisciplinary and multidisciplinary environmental observation strategies, fostering collaborations between communities to develop better measurement standards, perform comparisons, establish metrological guidelines and operating procedures for observation networks.

Bibliography

2030Strategy - The Global Ocean Observing System 2030 Strategy, 2019, https://www.goosocean.org

A.C.I.A - Arctic Climate Impact Assessment,. "Impacts of a warming Arctic: Arctic climate impact assessment." Impacts of a Warming Arctic-Arctic Climate Impact Assessment. Cambridge: Cambridge University Press, 2004.

Alcocer, Alex, Paulo Oliveira, and Antonio Pascoal. "Underwater acoustic positioning systems based on buoys with GPS." *Proceedings of the Eighth European Conference on Underwater Acoustics*. Vol. 8. 2006.

Alford, Matthew H., et al. "Near-inertial internal gravity waves in the ocean." *Annual review of marine science* 8 (2016): 95-123.

Aliani, Stefano, et al. "Characterization of seawater properties and ocean heat content in Kongsfjorden, Svalbard Archipelago." *Rendiconti Lincei* 27.1 (2016): 155-162.

Apel, John R. "Oceanic internal waves and solitons." *An atlas of oceanic internal solitary waves* (2002): 1-40.

ARICE: Arctic Research Icebreaker Consortium: A strategy for meeting the needs for marine-based research in the Arctic, Deliverable 6.2., Recommendations for automatic environmental data collection of ice going vessels, 2019.

Ashley, Gail M. "Glaciolacustrine environments." *Modern and past glacial environments*. Butterworth-Heinemann, 2002. 335-359.

Azzaro Maurizio, et al., “Microbial metabolism in front of Kongsfjorden glaciers (2018)”, POLAR 2018, Davos (Switzerland), 15-26/06/2018.

Barletta, S., G. L. Del Bono, and L. Salvati. "Nota preliminare sui lavori geomorfologici e geominerari subacquei effettuati dal Servizio Geologico d’Italia dal 1964 al 1969." *Boll. Serv. Geol. It* (1969): 83-89.

Batchelor, Christine L., Julian A. Dowdeswell, and Dag Ottesen. "Submarine glacial landforms." *Submarine Geomorphology*. Springer, Cham, 2018. 207-234.

Bellingham, James G., and Kanna Rajan. "Robotics in remote and hostile environments." Science

318.5853 (2007): 1098-1102.

Bensi, Manuel, et al. "Shelf and slope dynamics offshore the west Svalbard continental margin." 2018.

Bensi, Manuel, et al. "Deep flow variability offshore south-west Svalbard (Fram Strait)." Water 11.4 (2019): 683.

Bergh, S. G., Maher, H. D. & Braathen, A. 2000: Tertiary divergent thrust directions from partitioned transpression, Brøggerhalvøya, Spitsbergen. Nor. Geol. Tidsskr. 80, 63–82.

Błaszczyk, Małgorzata, Jacek A. Jania, and Jon Ove Hagen. "Tidewater glaciers of Svalbard: Recent changes and estimates of calving fluxes." Polish Polar Research 30.2 (2009): 85-142.

Bojinski, Stephan, et al. "The concept of essential climate variables in support of climate research, applications, and policy." Bulletin of the American Meteorological Society 95.9 (2014): 1431-1443.

Bourriquen, Marine, et al. "Coastal evolution and sedimentary mobility of Brøgger Peninsula, northwest Spitsbergen." Polar Biology 39.10 (2016): 1689-1698.

Bruzzone, Gabriele, Angelo Odetti, and Massimo Caccia. "Remote Data Collection Near Marine Glacier Fronts Unmanned Vehicles for Autonomous Sensing, Sampling in the North Pole." *Sea Technology* 59.3 (2018): 22-26.

Bruzzone, Gabriele, et al. "Monitoring of Sea-Ice-Atmosphere Interfacein the Proximity of Arctic Tidewater Glaciers: The Contribution of Marine Robotics." *Remote Sensing* 12.11 (2020): 1707.

Buch, Erik et al., Integrated Arctic Observation System, INTAROS, Deliverable 1.1, Initial Requirement Report, 2017, https://intaros.nersc.no/content/initial-requirement-report

Buijsman, Maarten C., et al. "Internal Gravity Waves☆☆." *Encyclopedia of Ocean Sciences*. Elsevier, 2019. 622-632.

Burton, David J., et al. "Marginal fluctuations of a Svalbard surge-type tidewater glacier, Blomstrandbreen, since the Little Ice Age: a record of three surges." *Arctic, Antarctic, and Alpine Research* 48.2 (2016): 411-426.

Cacchione, D. A., Lincoln F. Pratson, and A. S. Ogston. "The shaping of continental slopes by internal tides." *Science* 296.5568 (2002): 724-727.

Caccia, Massimo, et al. "Marine robotics for sampling air-sea-ice interface in the Arctic region." *Geophysical Research Abstracts*. Vol. 21. 2019.

Caratori Tontini F., Stefanelli P., Giori I., Faggioni O., Carmisciano C. (2004). The revised aeromagnetic anomaly map of Italy. Ann. Geophys., 47

Carlino, Stefano, et al. "Geothermal investigations of active volcanoes: the example of Ischia Island and Campi Flegrei caldera (southern Italy)." *Engineering Geology for Society and Territory-Volume 1*. Springer, Cham, 2015. 369-372.

Carlson, Daniel F., et al. "Retrieval of ice samples using the Ice Drone." *Frontiers in Earth Science* 7 (2019): 287.

Caroppo, Carmela, et al. "Late summer phytoplankton blooms in the changing polar environment of the Kongsfjorden (Svalbard, Arctic)." *Cryptogamie, Algologie* 38.1 (2017): 53-72.

Carotenuto, F., et al. "Design and performance of a low-cost atmospheric composition monitor for deployment in extreme environments." *IOP Conference Series: Earth and Environmental Science*. Vol. 489. No. 1. IOP Publishing, 2020.

Carr, S. J., and J. F. Hiemstra. "Sedimentary evidence against a local ice-cap on the Shetland Isles at the Last Glacial Maximum." *Proceedings of the Geologists' Association* 124.3 (2013): 484-502.

Carr, J. Rachel, et al. "Basal topographic controls on rapid retreat of Humboldt Glacier, northern Greenland." *Journal of Glaciology* 61.225 (2015): 137-150.

Casalbore, Daniele, et al. "Morpho-acoustic characterization of a shallow-water mud volcano offshore Scoglio d'Affrica (Northern Tyrrhenian Sea) responsible for a violent gas outburst in 2017." *Marine Geology* 428 (2020): 106277.

Cassano, Emanuele, et al. "The Island of Elba-northern Tyrrhenian sea aeromagnetic and gravity data." *Ofioliti* 26.2a (2007): 153-160.

Cavaliere, Alice, et al. "Development of low-cost air quality stations for next generation monitoring networks: Calibration and validation of pm2. 5 and pm10 sensors." *Sensors* 18.9 (2018): 2843.

Chiappini, Massimo, et al. "Shaded relief magnetic anomaly map of Italy and surrounding marine areas." *Annals of Geophysics* 43.5 (2000).

Chiocci F. L., Casalbore D., Martorelli E., Beaubien S., Bigi S., Pierdomenico M. (2017). Emissioni di fluidi al largo dello scoglio d'Affrica (Arcipelago Toscano). Rapporto per il Dipartimento di Protezione Civile.

Cole, Sylvia T., et al. "Internal waves in the Arctic: influence of ice concentration, ice roughness, and surface layer stratification." *Journal of Geophysical Research: Oceans* 123.8 (2018): 5571-5586.

Connelly Douglas, Final Report Summary - SENSEOCEAN (SenseOCEAN: Marine sensors for the 21st Century), 2017, https://cordis.europa.eu/project/id/614141/reporting

Cornamusini, G., et al. "Eocene-Miocene evolution of the north Tyrrhenian Sea." *Bollettino della Società geologica italiana* 1 (2002): 769-787.

Cottier, Finlo, et al. "Water mass modification in an Arctic fjord through cross-shelf exchange: The seasonal hydrography of Kongsfjorden, Svalbard." *Journal of Geophysical Research: Oceans* 110.C12 (2005).

Cottier, Finlo R., et al. "Wintertime warming of an Arctic shelf in response to large-scale atmospheric circulation." *Geophysical Research Letters* 34.10 (2007).

D'Angelo, Alessandra, et al. "Multi-year particle fluxes in Kongsfjorden, Svalbard." *Biogeosciences* 15.17 (2018): 5343-5363.

D'Asaro, Eric A. "The energy flux from the wind to near-inertial motions in the surface mixed layer." *Journal of Physical Oceanography* 15.8 (1985): 1043-1059.

Dañobeitia, Juan Jose, et al. "Toward a comprehensive and integrated strategy of the European marine research 936 infrastructures for ocean observations." *Frontiers in Marine Science* 7 (2020): 180.

Del Bono, G. L., and Stani Giammarino. "Rinvenimento di manifestazioni metanifere nelle Praterie a Posidonie sui fondi marini prospicienti lo «Scoglio d'Africa» nell'Arcipelago Toscano." *Atti Ist. Geol. Univ. Genova* 6.1 (1968): 11.

Demarte, Maurizio, et al. "Innovative REA tools for integrated bathymetric survey." *EGUGA* (2017): 13651.

Deschamps-Berger, Cesar, et al. "Closing the mass budget of a tidewater glacier: the example of Kronebreen, Svalbard." *Journal of Glaciology* 65.249 (2019): 136-148.

Dosser, Hayley V., Luc Rainville, and John M. Toole. "Near-inertial internal wave field in the Canada Basin from ice-tethered profilers." *Journal of physical oceanography* 44.2 (2014): 413-426.

Dosser, Hayley V., and Luc Rainville. "Dynamics of the changing near-inertial internal wave field in the Arctic Ocean." *Journal of Physical Oceanography* 46.2 (2016): 395-415.

Dowdeswell, Julian A., et al., eds. "Atlas of submarine glacial landforms: modern, Quaternary and ancient." Geological Society of London, 2016.

ECO Magazine, MARCH/APRIL 2019 environment coastal & offshore, ecomagazine.com

Eriksson, L., and C. Savelli. "Magnetic anomalies and magmatic events in and around the island of Elba (Northern Tyrrhenian Sea)." *Marine geology* 87.1 (1989): 85-93.

Etiope, Giuseppe, et al. "Reappraisal of the fossil methane budget and related emission from geologic sources." *Geophysical Research Letters* 35.9 (2008).

Etiope, Giuseppe, Akper Feyzullayev, and Calin L. Baciu. "Terrestrial methane seeps and mud volcanoes: a global perspective of gas origin." *Marine and Petroleum Geology* 26.3 (2009a): 333-344.

Etiope, G., et al. "Evidence of subsurface anaerobic biodegradation of hydrocarbons and potential secondary methanogenesis in terrestrial mud volcanoes." *Marine and Petroleum Geology* 26.9 (2009b): 1692-1703.

Etiope, Giuseppe, and Barbara Sherwood Lollar. "Abiotic methane on Earth." *Reviews of Geophysics* 51.2 (2013): 276-299.

Etiope, Giuseppe, and Martin Schoell. "Abiotic gas: atypical, but not rare." *Elements* 10.4 (2014): 291-296.

Etiope, Giuseppe. "Natural gas seepage." *The Earth's Hydrocarbon Degassing, Springer* 640 (2015).

Etiope, Giuseppe. "Abiotic methane in continental serpentinization sites: an overview." *Procedia Earth and Planetary Science* (2017).

Etiope and Schwietzke, "Gridded maps of geological methane emissions and their isotopic signature." *Earth System Science Data* (2019).

Etiope, Giuseppe, et al. "Global geological methane emissions: An update of top-down and bottom-up estimates." *Elementa: Science of the Anthropocene* 7 (2019).

EURAMET, the European Association of National Metrology Institutes, Strategic Research Agenda for Metrology in Europe, Version 1.0 (03/2016)

Favier, Lionel, et al. "Retreat of Pine Island Glacier controlled by marine ice-sheet instability." *Nature Climate Change* 4.2 (2014): 117-121.

Fer, Ilker. "Near-inertial mixing in the central Arctic Ocean." *Journal of physical oceanography* 44.8 (2014): 2031-2049.

Ferretti R., et al. "Critical marine environment observation: measurement problems, technological solutions and procedural methods", IMEKO TC-19 *Metrology for the Sea*, 5-7 October 2020

FOO - A Framework for Ocean Observing. By the Task Team for an Integrated Framework for Sustained Ocean Observing, UNESCO 2012, IOC/INF-1284, doi: 10.5270/OceanObs09-FOO

Forwick, Matthias, et al. "Last glacial ice-sheet dynamics and deglaciation on Svalbard inferred from fjord records." *EGUGA* (2015): 2918.

Fox, N. P. "Developments in optical radiometry." PROCEEDINGS-INTERNATIONAL SCHOOL OF PHYSICS ENRICO FERMI. Vol. 166. IOS Press; Ohmsha; 2007.

GCOS-154 Implementation Plan for the Global Observing System for Climate in Support of the UNFCCC (2010 Update) SYSTEMATIC OBSERVATION REQUIREMENTS FOR SATELLITE-BASED DATA PRODUCTS FOR CLIMATE 2011 Update

Gerland, Sebastian, et al. "Long-term monitoring of landfast sea ice extent and thickness in Kongsfjorden, and related applications (FastIce)." *SESS report 2019*. Svalbard Integrated Arctic Earth Observing System, 2020. 160-167.

GOOS website -
https://www.goosocean.org/index.php?option=com_content&view=article&id=14&Itemid=114

GOOS-214 - THE GLOBAL OBSERVING SYSTEM FOR CLIMATE: IMPLEMENTATION NEEDS, GCOS-200, World Meteorological Organization, 2016

Greve, Sonja, et al. "Shear-velocity structure of the Tyrrhenian Sea: Tectonics, volcanism and mantle (de) hydration of a back-arc basin." *Earth and Planetary Science Letters* 400 (2014): 45-53.

Guidance Note 1: ECVs - sources of information on GCOS requirements and international standards relevant to climate observing.

Guidelines ROADS for contributing to SAON's Roadmap for Arctic Observing and Data Systems (ROADS), Draft version 30 th August 2019.

Haas, Christian, et al. "Helicopter-borne measurements of sea ice thickness, using a small and lightweight, digital EM system." *Journal of Applied Geophysics* 67.3 (2009): 234-241.

Haensch, T., S. Leschiutta, and A. Wallard, eds. Metrology and Fundamental Constants. Vol. 166. *IOS Press*, (2007).

Halbach, Laura, et al. "Tidewater glaciers and bedrock characteristics control the phytoplankton growth environment in a fjord in the arctic." *Frontiers in Marine Science* 6 (2019): 254.

Hanelt, Dieter, et al. "Light regime in an Arctic fjord: a study related to stratospheric ozone depletion as a basis for determination of UV effects on algal growth." *Marine Biology* 138.3 (2001): 649-658.

Hanssen-Bauer, I., et al. "Climate in Svalbard 2100." *A knowledge base for climate adaptation* (2019).

Hodder, K. R., R. Gilbert, and J. R. Desloges. "Glaciolacustrine varved sediment as an alpine hydroclimatic proxy." *Journal of Paleolimnology* 38.3 (2007): 365-394.

Holland, David M., and Adrian Jenkins. "Modeling thermodynamic ice–ocean interactions at the base of an ice shelf." *Journal of Physical Oceanography* 29.8 (1999): 1787-1800.

Holmes, Felicity Alice. "An investigation into the relative importance of different climatic and oceanographic factors for the frontal ablation rate of Kronebreen, Svalbard." (2018).

Hop, Haakon, et al. "The marine ecosystem of Kongsfjorden, Svalbard." *Polar Research* 21.1 (2002): 167-208.

Hop, Haakon, et al. "The Ecosystem of Kongsfjorden, Svalbard." *The Ecosystem of Kongsfjorden, Svalbard*. Springer, Cham, (2019). 1-20.

Howat, Ian M., Ian Joughin, and Ted A. Scambos. "Rapid changes in ice discharge from Greenland outlet glaciers." *Science* 315.5818 (2007): 1559-1561.

Howe, John A., et al. "Autonomous underwater vehicle (AUV) observations of recent tidewater glacier retreat, western Svalbard." *Marine Geology* 417 (2019): 106009.

Hübner, Christiane, et al. "Improving Arctic Observation Systems through coordination–examples from the first State of Environmental Science in Svalbard (SESS) report." *Geophysical Research Abstracts*. Vol. 21. 2019.

Husum, Katrine, et al. "The marine sedimentary environments of Kongsfjorden, Svalbard: an archive of polar environmental change." (2019).

Iezzi, Gianluca, et al. "First documented deep submarine explosive eruptions at the Marsili Seamount (Tyrrhenian Sea, Italy): A case of historical volcanism in the Mediterranean Sea." *Gondwana Research* 25.2 (2014): 764-774.

IHO-C13, Chapter2- International Hydrographic Organization, C-13 - The Manual on Hydrography, Chapter 2 Positioning.

IHO S44 - IHO STANDARDS FOR HYDROGRAPHIC SURVEYS (S-44), 6 th Edition draft 1.7.0 July 2019

Inall, M. E., G. I. Shapiro, and T. J. Sherwin. "Mass transport by non-linear internal waves on the Malin Shelf." *Continental Shelf Research* 21.13-14 (2001): 1449-1472.

INGV - Rapporto tecnico, 2017. Attività di prospezione geofisica e oceanografica su Nave Aretusa (IIM- Marina Militare) nel tratto di Mare tra le isole di Montecristo e Pianosa (Scoglio d'Africa).

IOM-Report, BIPM, WMO: Report on the WMO-BIPM workshop on Measurement challenges for global observation systems for climate change monitoring. Rapport BIPM-2010/08 ; WMO/TD-No. 1557, IOM-Report No. 105 ; (2010)

IPCC, Climate Change. "Mitigation of climate change." Contribution of working group III to the fifth assessment report of the intergovernmental panel on climate change (2014).

Jakobsson, Martin, Larry Mayer, and David Monahan. "Arctic ocean bathymetry: A necessary geospatial framework." *Arctic* (2015): 41-47.

Joseph, A. "Chapter 6-seafloor hot chimneys and cold seeps: mysterious life around them." *Investigating Seafloors and Oceans, ed. A. Joseph (Amsterdam: Elsevier)* (2017): 307-375.

Joughin, Ian, Waleed Abdalati, and Mark Fahnestock. "Large fluctuations in speed on Greenland's Jakobshavn Isbrae glacier." *Nature* 432.7017 (2004): 608-610.

Joughin, Ian, et al. "Greenland flow variability from ice-sheet-wide velocity mapping." *Journal of Glaciology* 56.197 (2010): 415-430.

Kimball, Peter, et al. "The WHOI Jetyak: An autonomous surface vehicle for oceanographic research in shallow or dangerous waters." *2014 IEEE/OES Autonomous Underwater Vehicles (AUV)*. IEEE, 2014.

Klaucke, Ingo. "Sidescan sonar." *Submarine Geomorphology*. Springer, Cham, (2018). 13-24.

Kohler, J., et al. "Acceleration in thinning rate on western Svalbard glaciers." *Geophysical Research Letters* 34.18 (2007).

Larsen, Jan Rene, and Sandy Starkweather. "A Roadmap for Arctic Observing and Data Systems." *EGU General Assembly Conference Abstracts*, (2020).

Lee, Craig Michael, et al. "A framework for the development, design and implementation of a sustained arctic ocean observing system." *Frontiers in Marine Science* 6 (2019): 451.

Lindbäck, Katrin, et al. "Subglacial topography, ice thickness, and bathymetry of Kongsfjorden, northwestern Svalbard." *Earth System Science Data* 10.4 (2018).

Luckman, Adrian, et al. "Calving rates at tidewater glaciers vary strongly with ocean temperature." *Nature communications* 6.1 (2015): 1-7.

Lydersen, Christian, et al. "The importance of tidewater glaciers for marine mammals and seabirds in Svalbard, Norway." *Journal of Marine Systems* 129 (2014): 452-471.

Manga, Michael, et al., "Earthquake triggering of mud volcanoes." *Marine and Petroleum Geology* 26.9 (2009): 1785-1798.

Marcelli, Marco, et al. "New technological developments for oceanographic observations." *Oceanography* 4178 (2010).

Maturilli, Marion, Andreas Herber, and Gert König-Langlo. "Climatology and Time Series of Surface Meteorology in Ny¬ Ålesund, Svalbard." *Earth System Science Data* 5 (2013): 155-163.

Mazzini, Adriano, and Giuseppe Etiope. "Mud volcanism: an updated review." *Earth-Science Reviews* 168 (2017): 81-112.

Mazzola, Mauro, et al. "Probing of the Vertical Structure of the lower Atmosphere over Svalbard (ProVeSAS).", *SESS Report,* (2020)

Meier, M. F., and Austin Post. "Fast tidewater glaciers." *Journal of Geophysical Research: Solid Earth* 92.B9 (1987): 9051-9058.

Meire, Lorenz, et al. "Marine-terminating glaciers sustain high productivity in Greenland fjords." *Global Change Biology* 23.12 (2017): 5344-5357.

Meister, Patrick, et al. "Anaerobic methane oxidation inducing carbonate precipitation at abiogenic methane seeps in the Tuscan archipelago (Italy)." *PloS one* 13.12 (2018): e0207305.

Meslard, Florian, et al. "Suspended particle dynamics and fluxes in an Arctic fjord (Kongsfjorden, Svalbard)." *Estuarine, Coastal and Shelf Science* 204 (2018): 212-224.

Milton, M. J. T. "Metrology for chemical measurements in the environment." *PROCEEDINGS-INTERNATIONAL SCHOOL OF PHYSICS ENRICO FERMI*. Vol.166. IOS Press; Ohmsha; 1999, 2007.

Mitchell, Garrett A., et al. "Improved detection and mapping of deepwater hydrocarbon seeps: optimizing multibeam echosounder seafloor backscatter acquisition and processing techniques." *Marine Geophysical Research* 39.1-2 (2018): 323-347.

Moon, T., et al. "21st-century evolution of Greenland outlet glacier velocities." *Science* 336.6081 (2012): 576-578.

Morison et al., "Internal wave dissipation under sea ice." *Journal of Geophysical Research: Oceans* 90.C6 (1985): 11959-11966.

Morozov, E. G., et al. "Short-Period Internal Waves under an Ice Cover in Van Mijen Fjord, Svalbard." *Advances in Meteorology* 2011 (2011).

Morton, B., G. I. Taylor, and J. S. Turner. "Gravitational turbulent convection from maintained and instantaneous sources." *Proc R Soc Lond A* 234 (1956): 1-23.

Motteran G. and Ventura G. “Aspetti geologici, morfologici e ambientali dello Scoglio d’Africa (arcipelago toscano): nota preliminare”. *Atti Soc. tosc. Sci. nat., Mem., Serie A*, 110, (2005): 51-60.

Myhre, Gunnar, et al. "Aerosols and their relation to global climate and climate sensitivity." *Nature Education Knowledge* 4.5 (2013): 7.

Neal, Mark, et al. "A hardware proof of concept for a remote-controlled glacier-surveying boat." *Journal of Field Robotics* 29.6 (2012): 880-890.

Nilsen, Frank, et al. "A simple shelf circulation model: intrusion of Atlantic Water on the West Spitsbergen Shelf." *Journal of Physical Oceanography* 46.4 (2016): 1209-1230.

Nilssen, Ingunn, et al. "Integrated environmental mapping and monitoring, a methodological approach to optimise knowledge gathering and sampling strategy." *Marine pollution bulletin* 96.1-2 (2015): 374-383.

Nornes, Stein M. "Guidance and control of marine robotics for ocean mapping and monitoring." (2018).

Nuth, Christopher, et al. "Decadal changes from a multi-temporal glacier inventory of Svalbard." *The Cryosphere* 7.5 (2013): 1603-1621.

Odetti A., PhD Thesis - Study of innovative autonomous marine vehicles for monitoring in remote areas and shallow waters The Shallow Water Autonomous Multipurpose Platform (SWAMP), http://hdl.handle.net/11567/1003967

Odetti, Angelo, et al. "P2-ROV a portable/polar ROV." *OCEANS 2017-Aberdeen*. IEEE, 2017.

Odetti, Angelo, et al. "Design, development and testing at field of a modular Mini Automatic Water Sampler (MAWS) based on magnetic activation." *OCEANS 2019-Marseille*. IEEE, 2019.

Osborne et al. , "The influence of internal waves on deep-water drilling." *Journal of Petroleum Technology* 30.10 (1978): 1-497.

Ottesen, Dag, and J. A. Dowdeswell. "Assemblages of submarine landforms produced by tidewater glaciers in Svalbard." *Journal of Geophysical Research: Earth Surface* 111.F1 (2006).

Ottesen, Dag, et al. "Dynamics of the Late Weichselian ice sheet on Svalbard inferred from high-resolution sea-floor morphology." *Boreas* 36.3 (2007): 286-306.

Pascucci, Vincenzo, Saverio Merlini, and Ireneo Peter Martini. "Seismic stratigraphy of the Miocene-Pleistocene sedimentary basins of the Northern Tyrrhenian Sea and western Tuscany (Italy)." *Basin Research* 11.4 (1999): 337-356.

Pasculli, Lorenzo, et al. "New Cost-Effective Technologies Applied to the Study of the Glacier Melting Influence on Physical and Biological Processes in Kongsfjorden Area (Svalbard)." *Journal of Marine Science and Engineering* 8.8 (2020): 593.

Perovich, Donald K., et al. "Increasing solar heating of the Arctic Ocean and adjacent seas, 1979–2005: Attribution and role in the ice-albedo feedback." *Geophysical Research Letters* 34.19 (2007).

Piermattei, Viviana, et al. "Cost-effective technologies to study the arctic ocean environment." *Sensors* 18.7 (2018a): 2257.

Piermattei, Viviana, et al., “Preliminary Results of an Experimental Survey in Kongsfjorden Area (June 2017)”, (2018b), POLAR 2018, Davos, CH, 15-26/6/2018.

Pomar, L., et al. "Internal waves, an under-explored source of turbulence events in the sedimentary record." *Earth-Science Reviews* 111.1-2 (2012): 56-81.

Rice, Shawn L., et al. "Arctic seismic acquisition and processing." The Leading Edge 32.5 (2013): 546-554.

Røds, Johan-Fredrik. *Navigation in the Arctic. How can simulator training be used for assessment and reduction of risk?*. MS thesis. UiT The Arctic University of Norway, 2018.

Rovere, Marzia, et al. "Venting and seepage systems associated with mud volcanoes and mud diapirs in the southern Tyrrhenian Sea." *Marine Geology* 347 (2014): 153-171.

Sarkar, S., and Scotti. A. "From topographic internal gravity waves to turbulence." *Annual Review of Fluid Mechanics* 49 (2017): 195-220.

Saroni, Anna, et al. "Shallow submarine mud volcano in the northern Tyrrhenian sea, Italy." *Applied Geochemistry* 122 (2020): 104722.

Schellenberger, Thomas, et al. "Surface speed and frontal ablation of Kronebreen and Kongsbreen, NW Svalbard, from SAR offset tracking." *The Cryosphere* 9.6 (2015): 2339-2355.

Schild, K. M., et al. "Glacier calving rates due to subglacial discharge, fjord circulation, and free convection." *Journal of Geophysical Research: Earth Surface* 123.9 (2018): 2189-2204.

Sciarra, Alessandra, et al. "Shallow submarine seep of abiotic methane from serpentinized peridotite off the Island of Elba, Italy." *Applied Geochemistry* 100 (2019): 1-7.

Scotti, Alberto, and Jesús Pineda. "Observation of very large and steep internal waves of elevation near the Massachusetts coast." *Geophysical Research Letters* 31.22 (2004).

Simmons, Adrian, et al. "Observation and integrated Earth-system science: A roadmap for 2016–2025." *Advances in Space Research* 57.10 (2016): 2037-2103.

SIOS, Guidelines for metadata and data sharing, 21 June 2019

Slinn, Donald N., and J. J. Riley. "Turbulent dynamics of a critically reflecting internal gravity wave." *Theoretical and computational fluid dynamics* 11.3-4 (1998): 281-303.

Smith, Gregory Christopher, et al. "Polar ocean observations: a critical gap in the observing system and its effect on environmental predictions from hours to a season." *Frontiers in Marine Science* 6 (2019): 429.

Smith, Norman D. "Sedimentation processes and patterns in a glacier-fed lake with low sediment input." *Canadian Journal of Earth Sciences* 15.5 (1978): 741-756.

Speich, Sabrina, et al. "Oceanobs19: An Ocean of Opportunity." *Frontiers in Marine Science* 6 (2019): 570.

Spreen, Gunnar, and Stefan Kern. "Methods of satellite remote sensing of sea ice." *Thomas, DN, 3rd edn., Wiley Backwell* (2017).

Stevens, Laura A., et al. "Linking glacially modified waters to catchment-scale subglacial discharge using autonomous underwater vehicle observations." *Cryosphere* 10.1 (2016): 417-432.

Straneo, Fiammetta, et al. "Rapid circulation of warm subtropical waters in a major glacial fjord in East Greenland." *Nature Geoscience* 3.3 (2010): 182-186.

Sundfjord, A., et al. "Effects of glacier runoff and wind on surface layer dynamics and Atlantic Water exchange in Kongsfjorden, Svalbard; a model study." *Estuarine, Coastal and Shelf Science* 187 (2017): 260-272.

Svendsen, Harald, et al. "The physical environment of Kongsfjorden–Krossfjorden, an Arctic fjord system in Svalbard." *Polar research* 21.1 (2002): 133-166.

Syvitski, James PM. "On the deposition of sediment within glacier-influenced fjords: oceanographic controls." *Marine Geology* 85.2-4 (1989): 301-329.

Tanhua, Toste, et al. "What we have learned from the framework for ocean observing: Evolution of the global ocean observing system." *Frontiers in Marine Science* 6 (2019): 471.

Torsvik, Tomas, et al. "Impact of tidewater glacier retreat on the fjord system: modeling present and future circulation in Kongsfjorden, Svalbard." *Estuarine, Coastal and Shelf Science* 220 (2019): 152-165.

TR-SGL-20-02: An Analysis of Global Positioning System (GPS) Standard Positioning Service Performance for 2019, May 14, 2020, Technical Report: TR-SGL-20-02

Tverberg, Vigdis, et al. "The Kongsfjorden Transect: seasonal and inter-annual variability in hydrography." *The Ecosystem of Kongsfjorden, Svalbard*. Springer, Cham, (2019). 49-104.

Van den Heuvel F, et al., "SESS report 2019, Svalbard Integrated Arctic Earth Observing System", Longyearbyen, (2020)

Van Der Veen, C. J. "Tidewater calving." *Journal of Glaciology* 42.141 (1996): 375-385.

Vanicek, Petr, and Edward J. Krakiwsky. *Geodesy: the concepts*. Elsevier, (2015).

Vieli, Andreas, Martin Funk, and Heinz Blatter. "Tidewater glaciers: frontal flow acceleration and basal sliding." *Annals of Glaciology* 31 (2000): 217-221.

Vihma, Timo, et al. "Towards an advanced observation system for the marine Arctic in the framework of the Pan-Eurasian Experiment (PEEX)." *Atmospheric Chemistry and Physics* (2019).

Wadhams, Peter, Jeremy P. Wilkinson, and S. D. McPhail. "A new view of the underside of Arctic sea ice." *Geophysical Research Letters* 33.4 (2006).

Wezel, Forese Carlo. "The structure of the Calabro-Sicilian Arc: result of a post-orogenic intra-plate deformation." *Geological Society, London, Special Publications* 10.1 (1982): 345-354.

Woolliams, Emma, et al. "The European metrology network for climate and ocean observation." *19th International Congress of Metrology (CIM2019)*. EDP Sciences, 2019.

Zaldei, A., et al. "An integrated low-cost road traffic and air pollution monitoring platform for next citizen observatories." *Transp. Res. Procedia* 24 (2017): 531-538.

Zappalà, Giuseppe, et al. "Development of an automatic sampler for extreme polar environments: first in situ application in Svalbard islands." *Rendiconti Lincei* 27.1 (2016): 251-259.

Acknowledgments

This thesis describes the PhD work carried out in the framework of the XXXIII Cycle of the PhD in Earth and Marine Science of the University of Ferrara (UniFe), in collaboration with the Italian Hydrographic Institute (IIM) and the Italian National Research Council (CNR-INM).

Many people were fundamental in providing suggestions and ongoing support throughout the PhD.

A first special thanks goes to my tutor, Prof.ssa Roberta Ivaldi for her availability, for the ideas shared with me and for pushing me to look at the data from a different perspective to achieve the result.

A second special thanks goes to my tutor Prof. Massimo Coltorti for having made available his many years of experience and for the continuous help during the various phases of the doctorate.

Last but not least, a special thanks goes to my tutor Ing. Massimo Caccia for having pushed me to start this PhD and for his support during the development of the work.

This thesis could not exist without the data taken during the field campaigns and therefore a special thanks goes to the team that took care of the preliminary laboratory tests and data collection in Svalbard and in particular sincere thanks goes to Ing. Gabriele Bruzzone, Giorgio Bruzzone, Ing. Angelo Odetti, Edoardo Spirandelli and Mauro Giacopelli (CNR-INM).

The same thing is true for the Scoglio d’Affrica campaign, where the fundamental thanks go to the Italian Navy and in particular to the Captain and Crew of the ITS Magnaghi Navy Ship and all the members of the Hydrographic Institute (IIM). A special thanks goes to C.F. Maurizio Demarte, fundamental for the planning and implementation of the campaign. A second special thanks goes also to Dr. Roberto Nardini (IIM) for his support during the analysis of the data concerning the Scoglio d’Affrica campaign.

A sincere thanks goes to my colleague and friend Ing. Marco Bibuli who was fundamental, not only for the practical and scientific support during the work, but also for the moral one during the periods when the obstacles seemed insurmountable. I would like to thank again Angelo Odetti, colleague with whom I shared the office, for having patiently tolerate my frequent “bad moods” and for having always shared a positive point of view on things. A more general big thanks goes to all my colleague of CNR-INM, not only for having supported me in the research activities but also for the numerous and necessary coffee breaks.

A sincere thanks goes also to all the people of the University of Ferrara (teachers and students) with whom I came into contact and exchanged ideas during these three years.

Finally, my deep and sincere gratitude to my (extended) family for their continuous help and support in all the moments of my personal and professional life.